Einstein-Podolsky-Rosen experiment with two Bose-Einstein condensates

Inauguraldissertation

zur
Erlangung der Würde eines Doktors der Philosophie
vorgelegt der
Philosophisch-Naturwissenschaftlichen Fakultät
der Universität Basel

von

Paolo Colciaghi

2023

Genehmigt von der Philosophisch-Naturwissenschaftlichen Fakultät auf Antrag von

Erstbetreuer: Prof. Dr. Philipp Treutlein

Zusätzl. Erstbetreuer: Dr. Tilman Zibold

Zweitbetreuer: Prof. Dr. Christoph Bruder

Externer Experte: Prof. Dr. Marco Fattori

Basel, den 20. Juni 2023

Prof. Dr. Marcel Mayor

Dekan

Abstract

In 1935, Einstein, Podolsky, and Rosen (EPR) conceived a Gedankenexperiment in which two particles are entangled through interactions, spatially separated, and measured. Under the classical assumption of local realism, they showed that the measurement correlations predicted by quantum mechanics for this scenario lead to a violation of the Heisenberg uncertainty principle. This contradiction, later denominated *EPR paradox*, revealed that the completeness of quantum mechanics is not compatible with the local realist description of nature that characterises classical physics.

Although the EPR paradox has been observed between systems consisting of few particles, this has not yet been achieved between larger systems: The entanglement of macroscopic objects has already been demonstrated, but the measured correlations were not strong enough to demonstrate the EPR paradox. However, the presence of entanglement of the EPR type in many-particle systems has been shown by measuring correlations within single systems.

In this thesis I describe an EPR experiment with two spatially separated massive many-particle systems: In close analogy to the original Gedankenexperiment, we entangle about 1400 atoms in a two-component ^{87}Rb Bose-Einstein condensate (BEC) via tunable collisional interactions and coherently split them into two separate condensates. Our splitting technique preserves the overlap and coherence between the components in each of the split BECs, allowing us to individually manipulate them. The entanglement inherited from the initial system results in measurement correlations between the two BECs that are strong enough to show the EPR paradox.

Our work shows that the conflict between quantum mechanics and local realism does not disappear when the size of the involved systems is increased to $\sim 10^3$ atoms. In addition to this, EPR entanglement – in conjunction with the spatial separation and individual addressability of the two systems demonstrated in our experiment – is a valuable resource for quantum metrology and quantum information processing with many-particle systems.

Contents

1 Introduction **1**

2 Bose-Einstein condensation **4**
2.1 The phenomenon of Bose-Einstein condensation 4
2.2 The Gross-Pitaevskii equation 5
2.3 Two-component Bose-Einstein condensates 7
2.3.1 The ground state of ^{87}Rb 7
2.3.2 Collective spin formalism 10
2.3.3 Wigner function 12
2.3.4 Coherent spin states 13
2.3.5 Spin squeezing 14
2.3.6 Atom losses in two-component Bose-Einstein condensates 15
2.3.7 Coherence in two-component Bose-Einstein condensates 16

3 Experimental apparatus **18**
3.1 Magnetic fields and vacuum system 18
3.1.1 Magnetic trapping potentials 20
3.1.2 Current sources 21
3.2 Laser system 22
3.3 Radio-frequency and microwave generation 25
3.3.1 Evaporative cooling 26
3.3.2 Coherent manipulation 26
3.3.3 State-dependent potential 30
3.4 Imaging system 32
3.4.1 Primary imaging system 33
3.4.2 Secondary imaging systems 36
3.4.3 Imaging calibration 37
3.4.4 Imaging noise and typical imaging parameters 42
3.5 Experiment control and data acquisition 43
3.6 Typical experimental sequence 45

4 Einstein-Podolsky-Rosen experiment with two Bose-Einstein condensates **47**
4.1 The Einstein-Podolsky-Rosen paradox 48
4.2 The Einstein-Podolsky-Rosen paradox with many-particle systems 50
4.3 Generation of entanglement in a Bose-Einstein condensate . . 52
4.4 Coherently splitting a two-component Bose-Einstein condensate 53
4.4.1 Cloud separation 57
4.4.2 Individual manipulation of the split condensates 60
4.4.3 Addressability and strength of the transitions 63
4.5 Einstein-Podolsky-Rosen experiment with two Bose-Einstein condensates 64
4.5.1 Data analysis 71
4.5.2 Signal generation and local oscillator noise 72
4.6 Measuring the two systems in different bases 73

5 Summary and outlook **77**
5.1 Summary 77
5.2 Outlook 78

A IQ modulation programming **80**

B Elliptical regions of interest **82**

C Typical calibration measurements **84**
C.1 Cooling sequence 84
C.2 Magnetic field calibration 84
C.3 Rabi frequency calibration 85
C.4 Two-photon resonance 86
C.5 Ramsey phase calibration 87
C.6 Demixing-remixing dynamics 87
C.6.1 Demixing-remixing dynamics with spin echo 89
C.7 Squeezing tomography 90
C.8 Pulses during the time of flight 92
C.8.1 Resonance frequency 92
C.8.2 Pulse duration 92

D Phase of the split systems **94**

Chapter 1

Introduction

Classical physics satisfies the principles of local causality, which prohibits any causal connection between space-like separated events, and realism, which requires that all physical properties of a system exist independent of detection and can be determined without disturbing the system. Quantum mechanics, on the other hand, only makes probabilistic predictions about measurement outcomes and places a lower bound on the combined uncertainty of complementary observables – the Heisenberg uncertainty principle. Furthermore, quantum entanglement allows local measurements to instantaneously change the state of distant systems.

In 1935, Einstein, Podolsky, and Rosen (EPR) raised the question whether the quantum mechanical description of physical reality can be considered complete, or whether there are some "hidden" degrees of freedom that predetermine the measurement outcomes [1]. To address this, EPR proposed a Gedankenexperiment where two particles, A and B, are prepared in an entangled state, separated, and measured. They demonstrated that, in this scenario, assuming both the completeness of quantum mechanics and the validity of local realism (i.e. the union of local causality and realism) leads to a contradiction, which became known as the EPR paradox [2, 3].

Even though an experimental realisation of the Gedankenexperiment was unforeseeable at the time of its publication, EPR's work has had a groundbreaking impact on both the study of fundamental physics and quantum technology, as it was the first to reveal some of the most non-classical features of quantum mechanics – for example, the terms *entanglement* and *steering* were introduced by Schrödinger in his reaction to EPR's paper [2,3]. In 1964, Bell developed the Gedankenexperiment further by considering a different set of measurements. This allowed him to make an even stronger statement than the EPR paradox, demonstrating that the predictions of quantum mechanics cannot be reproduced by any local realist theory [4].

Local realism is so deeply rooted in classical physics and ubiquitous in our experience of macroscopic phenomena, that EPR imposed it as a requirement for a physical theory to be considered acceptable, thus concluding that quantum theory was incomplete. However, such a claim needed to be investigated experimentally: For what was known at the time, the states considered by EPR could have been physically inaccessible, or their description made by quantum mechanics could have been incorrect. Furthermore, we now know that the assumption of local realism does not hold in the microscopic world. Indeed, not only the experimental realisations of the EPR paradox in its original form have demonstrated the conflict between quantum mechanics and local realism [5–10], but increasingly sophisticated experimental Bell tests have yielded results inconsistent with the latter [11–18].

The experiments mentioned above, which were all performed with few particles, showed the non-local-realist behaviour of microscopic systems. However, local realism still governs our experience of macroscopic phenomena, which raises the question whether this non-classical aspect of quantum systems just becomes negligible in large, noisy, "everyday" objects, or whether the latter cannot be described correctly by quantum theory [19]. This question can be addressed by performing EPR experiments with increasingly macroscopic, massive systems [9, 20, 21], which poses the challenge of engineering strong entanglement and achieving a high level of control and coherence in such systems. In recent years, remarkable progress has been made in this direction, with the demonstration of entanglement between spatially separated macroscopic objects [22–27] and the observation of EPR-like correlations within individual many-particle systems [28–31].

In this thesis I describe the experimental realisation of an EPR experiment (in the spin version proposed by Bohm [32, 33]) with two massive many-particle systems. In our experiment, we first prepare a two-component Bose-Einstein condensate composed of about 1400 ^{87}Rb atoms in a squeezed spin state (which is many-particle entangled [34]) by means of tunable collisional interactions [35]. Then, we coherently split the system into two spatially separated clouds, which we can individually manipulate and measure. The measurement correlations due to the entanglement inherited from the original BEC are strong enough to demonstrate the EPR paradox, which is observed here for the first time with two mesoscopic systems.

The results presented in this thesis were published in

[36] P. Colciaghi, Y. Li, P. Treutlein, and T. Zibold, *Einstein-Podolsky-Rosen experiment with two Bose-Einstein condensates*, Phys. Rev. X, 13, 021031, 2023.

Further experimental work from the early stages of my doctorate was

published in

[37] Y. Li, K. Pawłowski, B. Décamps, P. Colciaghi, M. Fadel, P. Treutlein, and T. Zibold, *Fundamental limit of phase coherence in two-component Bose-Einstein condensates*, Phys. Rev. Lett., 125, 123402, 2020.

Outline

In Chap. 2, I go through the fundamentals of Bose-Einstein condensation, review the properties of our system, and introduce the formalism that we use to describe it. In Chap. 3, I describe the experimental apparatus. In Chap. 4, which contains the main results of this thesis, I discuss the EPR paradox, introduce the experimental criteria that we use to investigate it, describe the experimental sequence, and present the experimental results demonstrating the EPR paradox with two spatially separated BECs. In the appendix, I describe among others a range of calibration measurements that are essential to correctly set up the experiment.

Chapter 2

Bose-Einstein condensation

In the experiments described in this thesis we work with BECs for their properties such as excellent coherence, reliable state initialisation and manipulation, and macroscopic quantum behaviour. In this chapter I briefly review the fundamentals of Bose-Einstein condensation (following the approach used in Ref. [38]), discuss the properties of our own BEC, and introduce the formalism we use to describe it. For more extensive reviews about this topic, I refer the reader to Ref. [39–42].

2.1 The phenomenon of Bose-Einstein condensation

In 1924 Einstein predicted, based on Bose's considerations about photons [43], that a large fraction of the particles in a bosonic system should occupy the same single-particle state when the system is cooled below a certain temperature [44, 45]. This phenomenon, now known as Bose-Einstein condensation, was first observed experimentally in 1995 in dilute vapours of alkali metals [46–48].

Bose-Einstein condensation is a purely quantum statistical effect [41]: Let us consider the problem of distributing N indistinguishable particles with bosonic permutation symmetry among p states. When the number of accessible states p is reduced (typically by decreasing the temperature of the system) to the point where $p \lesssim N$, then the statistical weight of configurations where many particles occupy the same state becomes dominant. This is in contrast with the classical case of distinguishable particles, where the configurations with many different occupied states remain likelier.

As an alternative, qualitative argument [39], one can claim that symmetry-related phenomena become relevant when the wave functions

of the particles start overlapping, that is when their thermal de Broglie wavelength $\lambda_{\mathrm{dB}} = \sqrt{2\pi\hbar^2/mk_BT}$ becomes comparable to the inter-particle separation $n^{-1/3}$ [39], where m is the mass of the particles, T is their temperature, and n is their number density.

As it can be seen from the arguments above, Bose-Einstein condensation occurs below a certain critical temperature T_c, which depends on the spectrum of the motional states of particles in the system. For non-interacting bosons in a three-dimensional harmonic potential, the critical temperature is given by [40]

$$T_c^0 = \frac{\hbar\omega_{\mathrm{ho}}}{k_B}\left(\frac{N}{\zeta(3)}\right)^{1/3} \simeq 0.94\,\frac{\hbar\omega_{\mathrm{ho}}}{k_B}N^{1/3}, \tag{2.1}$$

where ζ is the Riemann ζ function and ω_{ho} is the geometric average of the oscillator frequencies. Taking into account finite size effects and interactions, one obtains the following corrections to the critical temperature [49],

$$T_c \simeq \left(1 - 0.73\,\frac{\bar{\omega}}{\omega_{\mathrm{ho}}}N^{-1/3} - 1.33\,\frac{a_s}{a_{\mathrm{ho}}}N^{1/6}\right)T_c^0, \tag{2.2}$$

where $\bar{\omega}$ is the arithmetic mean of the trap frequencies, a_s is the s-wave scattering length, and $a_{\mathrm{ho}} \coloneqq \sqrt{\hbar/m\omega_{\mathrm{ho}}}$ is the typical length scale of the harmonic oscillator. For $T < T_c$, the fraction of condensed particles in the system is given by

$$\frac{N_0}{N} = 1 - \left(\frac{T}{T_c}\right)^3, \tag{2.3}$$

where N_0 is the number of condensed particles. Further corrections to this model are discussed in [40].

It is worth spending a few words, as a final remark, about the role of interactions in the occurrence of Bose-Einstein condensation: The phenomenon was first predicted in the non-interacting case, leaving the question as to whether it could occur in an interacting system (hence at all in reality) open. As it turned out, while repulsive interactions mostly stabilise the condensate, attractive interactions tend to make it collapse. This effect is contrasted by the so-called quantum pressure from the kinetic term in the Hamiltonian, but above a critical number of condensed particles the interactions dominate and the BEC collapses [40].

2.2 The Gross-Pitaevskii equation

For our typical experimental parameters, we are not able to observe any non-condensed atoms [50, 51]. Therefore, we consider the thermal fraction

of our system as negligible and model our BEC as fully condensed – as a so-called zero-temperature BEC. The exact state of a BEC is given by the N particle Schrödinger equation, which is extremely difficult to solve due to interactions. In this section I will introduce the most common approximation used to model the state of a BEC, a Hartree-Fock ansatz known as the Gross-Pitaevskii equation (GPE) or mean-field approximation [41].

Besides the Hartree-Fock ansatz

$$\Psi(\vec{r}_1, \ldots, \vec{r}_N, t) = \prod_{i=1}^{N} \psi(\vec{r}_i, t), \tag{2.4}$$

where Ψ is the N-particle wave function and ψ is the single-particle wave function, we assume that the particles only interact via pairwise s-scattering interactions, described by the contact potential $g\delta(\vec{r} - \vec{r}')$ with interaction strength

$$g = \frac{4\pi\hbar^2 a_s}{m}. \tag{2.5}$$

Both these assumptions are excellent approximations for weakly-interacting dilute gases, such as our system.

In the static case, by minimising the energy expectation value obtained from Eq. (2.4) with the constraint of the wave function normalisation and dividing by N, we obtain the time-independent GPE (TIGPE)

$$\left(\hat{H}_{\mathrm{sp}}(\vec{r}) + g(N-1)|\psi(\vec{r})|^2\right)\psi(\vec{r}) = \mu\psi(\vec{r}), \tag{2.6}$$

where $\hat{H}_{\mathrm{sp}}(\vec{r}) \coloneqq (\hbar^2/2m)\nabla^2 + V(\vec{r})$ is the single-particle Hamiltonian in the external potential $V(\vec{r})$, the term $g(N-1)|\psi(\vec{r})|^2$ is an effective potential describing the inter-particle interactions as a mean field, and μ is the chemical potential. The chemical potential is the partial derivative of the energy expectation value w.r.t. the atom number, and it can be understood as the energy needed to add one particle to the BEC.

Generalising Eq. (2.6) to the dynamic case yields the time-dependent Gross-Pitaevskii equation (TDGPE)

$$i\hbar\partial_t\psi(\vec{r}, t) = \left(\hat{H}_{\mathrm{sp}}(\vec{r}, t) + g(N-1)|\psi(\vec{r}, t)|^2\right)\psi(\vec{r}, t). \tag{2.7}$$

The GPE has in general no analytic solution, and is typically solved numerically. Two notable exceptions are the harmonic-oscillator limit and the Thomas-Fermi limit. The first one is the non-interacting case, and results in ψ being identical to the single-particle ground-state wave function, which in the case of a harmonic potential corresponds to a Gaussian function. The

Thomas-Fermi limit corresponds to the case where the interaction energy is much larger than the kinetic energy, typically due to the particle number being very large. In this case, the kinetic term in the GPE can be neglected, yielding an inverted parabola as a static solution. Our experimental parameters correspond to neither of these regimes.

2.3 Two-component Bose-Einstein condensates

In this work we treat a BEC composed of atoms that possess an internal degree of freedom, $\{|i\rangle\}_{i\in\{1,\dots,M\}}$, which makes particles in different states distinguishable from each other. Such a system, called multi-component BEC, is described by a system of coupled GPEs. In the time-independent case, this reads

$$\left(\hat{H}^{(i)}_{\mathrm{sp}}(\vec{r}) + g_{ii}(N_i-1)|\psi_i(\vec{r})|^2 \ + \sum_{j\neq i} g_{ij}N_j|\psi_j(\vec{r})|^2\right)\psi_i(\vec{r}) = \mu_i\psi_i(\vec{r}), \quad (2.8)$$

for every $i \in \{1,\dots,M\}$, where ψ_i, N_i, and μ_i are respectively the wave function, the atom number, and the chemical potential of the i-th state, and g_{ij} is the interaction strength between the i-th and the j-th state. The multi-component TDGPE can be obtained in the same way.

2.3.1 The ground state of ^{87}Rb

In this thesis, we consider a two-component BEC constituted by two states in the hyperfine-split ground state of ^{87}Rb, whose structure is briefly reviewed in this section. More detailed information can be found in Ref. [52].

Since ^{87}Rb is an alkali metal, its electronic properties are mainly determined by the one electron populating the outermost orbital, resulting in a simple level structure. The hyperfine splitting results from the coupling between the total angular momenta of the electron, $\hat{\vec{J}}$, and of the nucleus, $\hat{\vec{I}}$. For $J = 1/2$, it takes the simple form

$$\hat{H}_{\mathrm{hfs}} = A_{\mathrm{hfs}}\hat{\vec{I}}\cdot\hat{\vec{J}}, \quad (2.9)$$

where A_{hfs} is the magnetic dipole moment of the involved fine-structure manifold [52]. Eq. (2.9) is diagonalised in the basis formed by the states $|F, m_F\rangle$, where F and m_F are the quantum numbers related respectively

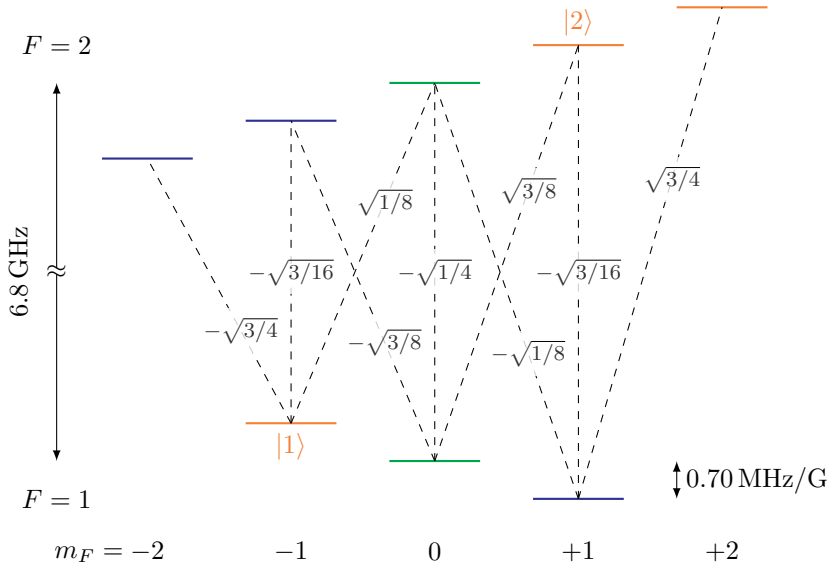

Figure 2.1: Level diagram of the hyperfine split ground state of ^{87}Rb in the linear Zeeman regime. The states are indicated by solid horizontal lines, whose colour represents the sign of the respective magnetic moment: Orange for positive, green for zero, and blue for negative. Dashed lines indicate possible microwave magnetic dipole transitions and the respective non-vanishing matrix elements $\langle F, m_F | \hat{J}_p | F', m'_F \rangle$, where $p \in \{-, z, +\}$. The $\hat{J}_z$ matrix elements are non-vanishing for the transitions with $\Delta m_F = 0$, whereas those relative to $\hat{J}_\pm \coloneqq \hat{J}_x \pm i\hat{J}_y$ are non-vanishing for $\Delta m_F = \pm 1$. The frequency splitting of the states is not to scale.

to the total angular momentum, $\hat{\vec{F}} \coloneqq \hat{\vec{J}} + \hat{\vec{I}}$, and to its projection along the quantisation axis. The ground state of ^{87}Rb is given by $J = 1/2$ and $I = 3/2$, thus it is hyperfine split into $F = 1$ and $F = 2$, separated by $2A_{\mathrm{hfs}} = h \times 6.834\,682\,611\,\mathrm{GHz}$ [52]. In absence of externally applied fields, states with different m_F are degenerate.

An atom coupled to a static magnetic field $\vec{B}$ is described by the Breit-Rabi Hamiltonian

$$\hat{H}_{\mathrm{BR}} = \hat{H}_{\mathrm{hfs}} + \mu_B(g_I \hat{\vec{I}} + g_J \hat{\vec{J}}) \cdot \vec{B}, \tag{2.10}$$

where μ_B is the Bohr magneton, and the g factors related to $\hat{\vec{I}}$ and $\hat{\vec{J}}$ are respectively $g_I \approx -1 \times 10^{-3}$ and $g_J \approx 2.003$ [52]. If we restrict ourselves to the ground state ($J = 1/2$ and $I = 3/2$), Eq. (2.10) can be diagonalised analytically. Since in our experiments we use magnetic fields which induce energy shifts much smaller than the hyperfine splitting, we express the eigenvalues of Eq. (2.10) in the $|F, m_F\rangle$ basis

$$E_{|F,m_F\rangle} = -\frac{A_{\mathrm{hfs}}}{4} + g_I \mu_B m_F B \pm A_{\mathrm{hfs}} \sqrt{1 + m_F \xi + \xi^2}, \tag{2.11}$$

where $\xi \coloneqq (g_J - g_I)\mu_B B/(2A_{\mathrm{hfs}})$, $B \coloneqq |\vec{B}|$, $\pm$ is $+$ $(-)$ for $F = 2$ $(F = 1)$, and where we have chosen the quantisation axis parallel to the magnetic field [52]. For weak magnetic fields, $\xi \ll 1$, the magnetic-field dependence in Eq. (2.11) can be approximated by the linear Zeeman effect

$$E_Z \approx g_F m_F \mu_B B, \tag{2.12}$$

where $g_F \approx \pm 1/2$ (with the same sign convention as above), which yields a relative shift between adjacent m_F levels of $g_F \mu_B \approx h \times 0.70\,\mathrm{MHz/G}$, see Fig. 2.1. This is a good approximation for our experimental parameters.

All states with a positive magnetic moment $g_F m_F \mu_B$ – also known as low-field seeking states, orange in Fig. 2.1 – can be trapped in a minimum of the magnetic field modulus $B(\vec{r})$. Among these,

$$|1\rangle \coloneqq |F = 1, m_F = -1\rangle\,,$$
$$|2\rangle \coloneqq |F = 2, m_F = +1\rangle\,,$$

have nearly identical magnetic moment and thus experience the same trapping potential. In addition to this, they have very similar s-wave-scattering lengths,

$$a_{11} = 100.40\,a_0,$$
$$a_{12} = 98.01\,a_0,$$
$$a_{22} = 95.44\,a_0,$$

where a_0 is the Bohr radius [53]. Thus, using these two states as BEC components guarantees that they maintain nearly perfect overlap for our experimental parameters: From the numerical solution of the two-component TDGPE shown in Ref. [51], it resulted that their overlap oscillates between 97.7 % and 100 % during the so-called *breathing dynamics*. This was also confirmed experimentally by measuring the interferometric visibility of our system, see Sec. 2.3.7, which was observed to be 97 %.

Since in this thesis we are interested in coherent superpositions of $|1\rangle$ and $|2\rangle$, it is desirable to minimise the sensitivity of such superpositions to fluctuations of the magnetic field. From Eq. (2.11) (not in the linear approximation), it results that there is a so-called *magic field* value $B_0 = 3.228\,917\,\mathrm{G}$ around which the differential Zeeman shift between $|1\rangle$ and $|2\rangle$ is first-order magnetic field insensitive,

$$\omega_{12} = \omega_0 + \beta(B - B_0)^2, \tag{2.13}$$

where $\beta = 2\pi \times 431\,\mathrm{HzG}^{-2}$ and $\omega_0 = 2\pi \times 6.834\,678\,114\,\mathrm{GHz}$ [54]. Performing experiments close to the magic field makes it possible to attain coherence times of hundreds of milliseconds with our experimental apparatus [37] and up to several seconds in atomic clock experiments[1] [55, 56].

2.3.2 Collective spin formalism

As discussed in Sec. 2.3.1, the two components of our BEC show nearly perfect overlap. Due to this, we can neglect the spatial dynamics and focus on the internal degree of freedom of the atoms: Since it is a collection of pseudo-spin-1/2 (i.e. two-level) particles, we can describe our system with the collective spin formalism [57].

The collective spin components of the system are defined as the sums of the corresponding individual spin components

$$\hat{S}_{x,y,z} \coloneqq \frac{1}{2}\sum_{i=1}^{N} \hat{\sigma}^{(i)}_{x,y,z}, \tag{2.14}$$

where $\hat{\sigma}^{(i)}_{x,y,z}$ are the Pauli matrices applied to the i-th particle. The collective spin components satisfy the angular momentum commutation relations

$$[\hat{S}_a, \hat{S}_b] = i \sum_{c\in\{x,y,z\}} \varepsilon_{abc}\hat{S}_c, \tag{2.15}$$

[1] Including the effect of spin self-rephasing, coherence times of one minute have been observed [55].

where $a, b, c \in \{x, y, z\}$ and ε_{abc} is the Levi-Civita symbol.

Since our atoms are indistinguishable bosons, we can restrict our discussion to the Hilbert space of states symmetric under particle exchange, known as the fully symmetric subspace, which has dimension $N+1$ and is characterised by the maximal total spin length of $S = N/2$, where S is defined by $S(S+1) \coloneqq \langle \hat{\vec{S}}^2 \rangle$. In this case, we can treat the two states $|1\rangle$ and $|2\rangle$ as bosonic modes and make use of Schwinger's representation of angular momentum [58], i.e. express the collective spin operators in terms of their creation ($\hat{a}_1^\dagger$ and $\hat{a}_2^\dagger$) and annihilation operators ($\hat{a}_1$ and $\hat{a}_2$):

$$\hat{S}_x = \frac{\hat{a}_1^\dagger \hat{a}_2 + \hat{a}_2^\dagger \hat{a}_1}{2} \ , \ \hat{S}_y = \frac{\hat{a}_1^\dagger \hat{a}_2 - \hat{a}_2^\dagger \hat{a}_1}{2i} \ , \ \hat{S}_z = \frac{\hat{a}_1^\dagger \hat{a}_1 - \hat{a}_2^\dagger \hat{a}_2}{2} \ . \tag{2.16}$$

In the same way, the atom number operator of state $|i\rangle$ can be expressed as $\hat{N}_i = \hat{a}_i^\dagger \hat{a}_i$. Thus, we can re-write the total atom number operator as $\hat{N} = \hat{a}_1^\dagger \hat{a}_1 + \hat{a}_2^\dagger \hat{a}_2$ and the z-component of the collective spin as $\hat{S}_z = (\hat{N}_1 - \hat{N}_2)/2$. As described in Sec. 3.4, we measure our system by detecting the atom number present in the two states, thus we can measure directly the z-component of the collective spin. In order to measure other spin directions, we have to perform collective spin rotations before detection, see Sec. 3.4.1.

Assuming that the atom numbers in the two states are tightly distributed around their mean values, $\bar{N}_1$ and $\bar{N}_2$, a Hamiltonian suited to describe the collective spin dynamics can be derived by expanding the full Hamiltonian of the system around $\bar{N}_1$ and $\bar{N}_2$, and omitting the constant terms [59]:

$$\hat{H} = \Big[(\mu_1 - \mu_2) - 2\hbar\chi \langle \hat{S}_z \rangle + \hbar\tilde{\chi}(\hat{N} - \bar{N}) \Big] \hat{S}_z + \hbar\chi \hat{S}_z^2, \tag{2.17}$$

where $\bar{N}$ is the mean total atom number and

$$\chi \coloneqq \frac{1}{2\hbar} \left(\frac{\partial \mu_1}{\partial N_1} + \frac{\partial \mu_2}{\partial N_2} - \frac{\partial \mu_1}{\partial N_2} - \frac{\partial \mu_2}{\partial N_1} \right)_{\bar{N}_1, \bar{N}_2}, \tag{2.18}$$

$$\tilde{\chi} \coloneqq \frac{1}{2\hbar} \left(\frac{\partial \mu_1}{\partial N_1} - \frac{\partial \mu_2}{\partial N_2} \right)_{\bar{N}_1, \bar{N}_2}. \tag{2.19}$$

The second and third term in Eq. (2.17) represent rotations around the z axis proportional to $\langle \hat{S}_z \rangle$ and $(\hat{N} - \bar{N})$, respectively, whereas the last term induces a nonlinear evolution known as *one-axis twisting* (OAT) [60], which is relevant to the generation of entanglement in our system, see Secs. 2.3.5 and 4.3. The chemical potentials are defined as

$$\mu_i \coloneqq \frac{\partial H}{\partial N_i} = \int_{\mathbb{R}^3} \mathrm{d}^3 r \, \psi_i^* \hat{H}_{\mathrm{sp}}^{(i)} \psi_i + \sum_{j \in \{1,2\}} g_{ij} N_j \int_{\mathbb{R}^3} \mathrm{d}^3 r \, |\psi_i|^2 |\psi_j|^2 \tag{2.20}$$

for $i \in \{1, 2\}$. In the weak interaction limit (e.g. for small atom numbers), the mode functions $\psi_{1,2}$ are independent of the atom number and χ and $\tilde{\chi}$ are simplified to

$$\chi = \frac{1}{2\hbar}\left(g_{11}\int_{\mathbb{R}^3} \mathrm{d}^3 r\, |\psi_1|^4 + g_{22}\int_{\mathbb{R}^3} \mathrm{d}^3 r\, |\psi_2|^4 - 2g_{12}\int_{\mathbb{R}^3} \mathrm{d}^3 r\, |\psi_1|^2|\psi_2|^2\right), \tag{2.21}$$

$$\tilde{\chi} = \frac{1}{2\hbar}\left(g_{11}\int_{\mathbb{R}^3} \mathrm{d}^3 r\, |\psi_1|^4 - g_{22}\int_{\mathbb{R}^3} \mathrm{d}^3 r\, |\psi_2|^4\right). \tag{2.22}$$

Although for our experimental parameters we are not fully in the weak interaction limit, these expressions help us understand how χ and $\tilde{\chi}$ depend on the scattering lengths and density overlap of the BEC components. This indicates which experimental parameters can be modified to engineer the collisional phase shifts and the OAT dynamics terms in the Hamiltonian Eq. (2.17). For example, due to the similarity of the scattering lengths, the OAT term is negligible as long as the BEC components overlap, but can be activated by means of state-dependent potentials, see Secs. 2.3.5 and 3.3.3.

2.3.3 Wigner function

The complete description of the state of a system is given by its density matrix. However, this does not help us to gain a visual intuition of the state. A more intuitive – and still complete – representation of the collective spin state is given by the spherical Wigner function [61, 62], which is analogous to the planar Wigner function of a harmonic oscillator, but it is defined on a spherical phase space of radius $S = N/2$ known as *generalised* or *many-particle Bloch sphere*:

$$W(\theta, \varphi) \coloneqq \sum_{k=0}^{2S}\sum_{q=-k}^{k} \rho_{kq} Y_{kq}(\theta, \varphi), \tag{2.23}$$

where Y_{kq} are spherical harmonics, θ and φ are the polar and azimuthal angle, respectively, and the weights ρ_{kq} are the transformed density matrix elements

$$\rho_{kq} \coloneqq \sum_{m=-S}^{S}\sum_{m'=-S}^{S} t_{kq}^{Smm'} \langle S, m|\, \hat{\rho}\, |S, m'\rangle\,. \tag{2.24}$$

The transformation coefficients are defined as

$$t_{kq}^{Smm'} \coloneqq (-1)^{S-m}\sqrt{2k+1}\begin{pmatrix} S & k & S \\ -m & q & m' \end{pmatrix}, \tag{2.25}$$

where the last term in parentheses is the Wigner $3j$ symbol. This allows us to represent the collective spin components on the generalised Bloch sphere.

2.3.4 Coherent spin states

The simultaneous eigenstates of $\hat{S}_z$ and $\hat{\vec{S}}^2 = \hat{S}_x^2 + \hat{S}_y^2 + \hat{S}_z^2$ are the so-called *Dicke states*, which are denoted by $|S, m\rangle$, where $S(S+1)$ and m are the eigenvalues of $\hat{\vec{S}}^2$ and $\hat{S}_z$, respectively. Given that our system is restricted to the fully symmetric subspace, we are only interested in the Dicke states with $S = N/2$. Since they are eigenstates of $\hat{S}_z$, they have fully undetermined phase between the two BEC components and constitute the "natural" measurement basis of our system. However, the only Dicke states that can be prepared in our apparatus are the extremal Dicke states $|S, \pm S\rangle$ – also known as *stretched spin states*. The preparation of all other Dicke states (which are entangled states) would require non-destructive measurements and single-atom resolution.

Coherent spin states (CSS), on the other hand, can be prepared easily in our apparatus. These states are the tensor product of N identical single-particle states in the direction (θ, φ)

$$|\mathrm{CSS} : \theta, \varphi\rangle \coloneqq \left(\cos(\theta/2)\,|1\rangle + e^{i\varphi}\sin(\theta/2)\,|2\rangle\right)^{\otimes N}, \tag{2.26}$$

where $\theta \in [0, \pi]$ and $\varphi \in [0, 2\pi]$, and are therefore considered as the most "classical" states in our system. From their definition it is clear that they are separable, fully symmetric, polarised[2] states. Since CSSs are the collection of independent and identically prepared binary systems, much of their behaviour is given by binomial statistics: For example, the variance of a spin quadrature perpendicular to the mean spin direction is $\mathrm{Var}(\hat{S}_\perp) = S/2$, whereas the variance along $\hat{S}_z$ is $\mathrm{Var}(\hat{S}_z) = \sin^2(\theta)S/2$. Also, the expansion of a CSS in the Dicke basis is a binomial distribution

$$|\mathrm{CSS} : \theta, \varphi\rangle = \sum_{m=-S}^{S} \sqrt{\binom{N}{k} p^k (1-p)^{N-k}}\, e^{-im\varphi}\,|S, m\rangle\,, \tag{2.27}$$

with $N = 2S$, $k \coloneqq S + m$, and $p \coloneqq \cos^2(\theta/2)$. From Eq. (2.27) it is clear that stretched spin states are CSSs: $|S, S\rangle = |\mathrm{CSS} : 0, \varphi\rangle$ and $|S, -S\rangle = |\mathrm{CSS} : \pi, \varphi\rangle$. Any CSS can be obtained from a stretched spin state with one collective spin rotation:

$$|\mathrm{CSS} : \theta, \varphi\rangle = e^{-i\theta\hat{S}_{\varphi+\frac{\pi}{2}}}\,|S, S\rangle = e^{-i(\pi-\theta)\hat{S}_{\varphi-\frac{\pi}{2}}}\,|S, -S\rangle\,. \tag{2.28}$$

This is experimentally relevant, as we typically initialise the system in a stretched spin state and mainly apply Rabi pulses for further manipulations.

[2]Polarised states satisfy $\sqrt{\langle\hat{S}_x\rangle^2 + \langle\hat{S}_y\rangle^2 + \langle\hat{S}_z\rangle^2} \simeq N/2$.

2.3.5 Spin squeezing

CSSs are separable, Heisenberg limited states with equal uncertainty in all quadratures perpendicular to the mean spin direction. This uncertainty follows from the binomial statistics of uncorrelated spin-1/2 measurements and it determines the standard quantum limit (SQL) of metrological sensitivity. The SQL can be overcome, among others, by squeezed spin states (SSSs) [57, 60], which are fully symmetric, polarised states, where in the plane perpendicular to the mean spin direction, $\hat{S}_\mathrm{m}$, there is one quadrature showing reduced uncertainty (squeezed direction $\hat{S}_\mathrm{s}$). As required by the Heisenberg uncertainty principle, this is only possible at the expense of increased noise in the perpendicular quadrature (anti-squeezed direction $\hat{S}_\mathrm{as}$). Since the SQL follows from the uncorrelated measurement outcomes of the atoms, it is clear that SSSs are many-particle entangled states [34, 35, 57].

The noise reduction of a SSS w.r.t. the SQL is quantified by the number squeezing parameter [57],

$$\zeta^2 \coloneqq \frac{4\,\mathrm{Var}(\hat{S}_\mathrm{s})}{N}, \tag{2.29}$$

which is however not a measure of its metrological usefulness, as it does not take into account the interferometric contrast of the state, $2\langle\hat{S}_\mathrm{m}\rangle/N$. This is included by the spin squeezing parameter [63, 64]

$$\xi^2 \coloneqq \frac{N\,\mathrm{Var}(\hat{S}_\mathrm{s})}{\langle\hat{S}_\mathrm{m}\rangle^2}. \tag{2.30}$$

When $\xi^2 < 1$, the state can be used to overcome the SQL in interferometric measurements, thereby also demonstrating many-particle entanglement [34, 63, 64].

SSSs can be prepared starting from a CSS on the equator of the many-particle Bloch sphere $|\mathrm{CSS} : \pi/2, \varphi\rangle$ and applying OAT dynamics $\chi\hat{S}_z^2$ for a time $\lesssim N^{-2/3}/\chi$ [60], which in our experiments is achieved by modifying the overlap between the BEC components by means of state-dependent potentials, see Secs. 2.3.2 and 3.3.3. Both CSSs and SSSs are approximately Gaussian states, i.e. they can be described by first and second moments of the collective spin measurements – such as mean and variance. If we apply OAT for longer than $\sim N^{-2/3}/\chi$, we get oversqueezed states, whose description necessitates higher moments [57, 65, 66]. For the OAT evolution time $\pi/(2\chi)$, we obtain a Schrödinger cat state [57], which in our case is the coherent superposition of two diametrically opposite CSSs.

Although oversqueezing the state yields in principle more resources than normal squeezing [57, 65], SSSs are experimentally very convenient: Firstly,

measuring higher moments of the spin observables is a large experimental overhead and requires an elaborate optimisation of the process or more advanced detection strategies [66–68]. Secondly, SSSs are robust against particle losses, but become increasingly fragile as we oversqueeze – e.g. a cat state is completely destroyed by the loss of one particle.

2.3.6 Atom losses in two-component Bose-Einstein condensates

The dominant atom loss mechanisms in BECs are typically one-, two-, and three-body processes [51, 69]. One-body losses are due to collisions with the residual background gas present in the vacuum chamber. Two-body losses result from inelastic collisions between two atoms in the condensate, which can be subdivided into spin-dipole and spin-exchanging collisions. In ^{87}Rb, spin-dipole collisions are negligible. Spin-exchanging collisions are processes where two colliding particles exchange one quantum of angular momentum. In the case of the states we work with, the allowed spin-exchanging collision processes are

$$|2,1\rangle + |2,1\rangle \mapsto |2,0\rangle + |2,2\rangle\,,$$
$$|1,-1\rangle + |2,1\rangle \mapsto |1,0\rangle + |2,0\rangle\,,$$

where the states are denoted as $|F, m_F\rangle$. Three-body losses are due to processes where two atoms form a molecule and a third one converts the binding energy into kinetic energy. Three-body losses are dominant for large densities (typically reached for atom numbers $N > 10^5$), but negligible for our experimental parameters.

The equation describing the atom number evolution in our system is

$$\frac{\mathrm{d}N_1}{\mathrm{d}t} = -k_1^{(1)} N_1 - k_{12}^{(2)} N_1 N_2, \tag{2.31}$$
$$\frac{\mathrm{d}N_2}{\mathrm{d}t} = -k_2^{(1)} N_2 - k_{12}^{(2)} N_1 N_2 - k_{22}^{(2)} N_2^2, \tag{2.32}$$

where $k_A^{(i)}$ are the i-body loss rates involving the states in the set A. The loss rates depend on the loss constants $\kappa_A^{(i)}$ and on the atom density,

$$k_A^{(i)} = \kappa_A^{(i)} \int_{\mathbb{R}^3} \mathrm{d}^3 r \prod_{j \in A} |\psi_j(\vec{r}, t)|^2. \tag{2.33}$$

The one-body loss constants depend on the background gas density[3] and thus need to be determined experimentally; in our case, they are typically $\kappa_1^{(1)} = \kappa_2^{(1)} \approx 0.1\,\mathrm{s}^{-1}$. All other $\kappa_A^{(i)}$, on the other hand, can be treated as constants – they weakly depend on the magnetic field, which is kept constant in our experiments.

$$\kappa_{12}^{(2)} = 2.0 \times 10^{-20}\,\mathrm{m}^3\mathrm{s}^{-1}, \qquad [37]$$
$$\kappa_{22}^{(2)} = 10.3 \times 10^{-20}\,\mathrm{m}^3\mathrm{s}^{-1}. \qquad [37]$$

From comparing Eq. (2.31) to Eq. (2.32), it is clear that the loss process in our system is asymmetric. Indeed, the atom number in state $|2\rangle$ decays much faster than the one in state $|1\rangle$ [37].

Eqs. (2.31) and (2.32) describe the mean behaviour of atom losses. These are, however, stochastic processes. As described in Sec. 2.3.7, this fact has relevant consequences in the decoherence processes – so relevant, in fact, that it sets a fundamental limit to the coherence of our system [37, 70].

2.3.7 Coherence in two-component Bose-Einstein condensates

In this section I discuss the temporal phase coherence of our system, where by phase it is meant the relative phase between the two BEC components, which has been studied extensively in Ref. [37,51] and is crucial for the results presented in this thesis.

In order to characterise the phase coherence of a system, one typically performs a Ramsey interferometry experiment [71], which consists of preparing the system (assuming it is initialised in state $|1\rangle^{\otimes N}$) in a superposition state $[(|1\rangle + |2\rangle)/\sqrt{2}]^{\otimes N} = |\mathrm{CSS} : \pi/2, 0\rangle$ with a $\pi/2$ pulse, allowing it to evolve for a given interrogation time t_R, and applying a second $\pi/2$ pulse with a phase $\varphi_R \in [0, 2\pi)$ w.r.t. the first one. The second pulse maps the accumulated phase to an atom number imbalance, which is measured. Repeating this procedure with different phases yields a so-called Ramsey fringe, which in absence of phase noise takes the form

$$\langle N_{\mathrm{rel}}(\varphi_R)\rangle = -V\cos(\varphi_R + \varphi), \qquad (2.34)$$

where $N_{\mathrm{rel}} \coloneqq (N_1 - N_2)/(N_1 + N_2) \in [-1, 1]$ is the normalised atom number imbalance, $V \leq 1$ is the interferometric visibility, and φ is the phase accumulated during the state evolution. The visibility describes the mean spin

[3] Since one-body losses are not a limiting factor for the results presented in this thesis, we have not investigated how much of this process is caused by the residual pressure of the vacuum system and how much by the rubidium vapour from which the BEC is produced.

length normalised to $N/2$, which can be smaller than one in case of imperfect overlap between the two states (see Sec. 2.3.1) and of asymmetric losses (see Sec. 2.3.6). On the time scales of the experiments presented in this thesis, the visibility of a CSS (determined as described in Ref. [51]) is 97 %.

In the presence of phase noise, the accumulated phase φ changes from shot to shot, smearing the Ramsey fringe. The resulting measurements can be fitted by the function

$$\langle N_{\mathrm{rel}}(\varphi_R)\rangle = -C\cos(\varphi_R + \bar{\varphi}), \tag{2.35}$$

where C is the interferometric contrast and $\bar{\varphi}$ the average accumulated phase. The difference between the contrast and the visibility is a measure of the phase coherence of the system. In case of Gaussian phase noise, this is given by [72]

$$C = Ve^{-\frac{1}{2}\mathrm{Var}(\varphi)}. \tag{2.36}$$

In order to obtain the temporal behaviour of the coherence of the system, Ramsey fringes are measured for different interrogation times. The results of performing this procedure with our apparatus are presented and analysed in Ref. [37, 51], where they are compared with a quantum trajectory simulation in order to understand the mechanisms that lead to decoherence. In the following I briefly summarise the main results of such an analysis.

The dominant decoherence mechanism in our system originates from the so-called collisional clock shift term in the spin Hamiltonian Eq. (2.17), $\hbar\tilde{\chi}(\hat{N} - \bar{N})\hat{S}_z$, which induces an atom-number-dependent phase shift. Atom number fluctuations come both from preparation noise and from atom losses. If the latter were deterministic, we would be able to reconstruct the atom number at all times from the detected atom number (which is the only measurable piece of information) and we could correct for the clock shift completely. Unfortunately, since atom losses are a stochastic process, the clock-shift correction based on the detected atom number only eliminates part of this phase noise. Since atom losses are unavoidable in BECs, this constitutes a fundamental limitation to the phase coherence in two-component BECs.

The other effects that were considered, namely technical noise and phase diffusion, showed minor contributions to decoherence. An upper bound to technical noise was set by performing Ramsey experiments with a non-condensed atom cloud, where interatomic interactions are suppressed by the low density. Phase diffusion, which consists of the anti-squeezing caused by the OAT term in the Hamiltonian Eq. (2.17), is negligible in our case due to the excellent overlap between the BEC components and the nearly identical scattering lengths (see Sec. 2.3.1).

Chapter 3

Experimental apparatus

All experiments presented in this thesis have been performed on the atom chip apparatus in Prof. Philipp Treutlein's group at the University of Basel [73]. This apparatus allows us to produce two-component ^{87}Rb BECs composed of ~ 1500 atoms magnetically trapped close to a micro-fabricated wire structure, the atom chip, and to manipulate their internal state with homogeneous and inhomogeneous high-frequency electromagnetic fields. In this chapter, I give an overview of the experimental apparatus, spending more time on the parts that have changed over the course of my doctorate. A more complete description can be found in the previous doctoral theses written about this system [38, 42, 51, 69, 74, 75].

3.1 Magnetic fields and vacuum system

Atom chips [76] are micro-fabricated wire structures used to create trapping potentials for ultra-cold atom experiments. The versatile design and the strongly inhomogeneous fields produced close to the chip surface make it possible to engineer a rich variety of magnetic potentials – both static and high frequency – in compact experimental apparatuses. Furthermore, this technology can be easily integrated with a variety of devices (e.g. on-chip optics), making it suitable for a wide range of applications.

Our apparatus is centred around a multi-layer atom chip, see Fig. 3.1, described in [42, 69, 74]. The bottom layer, known as the base chip, provides mechanical support, all electrical connections to the atom chip, and some of the wire structures used in the initial cooling stages. It consists of a 800 µm thick AIN ceramic substrate with a 12 µm thick patterned gold layer, equipped with ribbon-cable-compatible pin headers for DC currents and mini-SMP connectors for high-frequency signals.

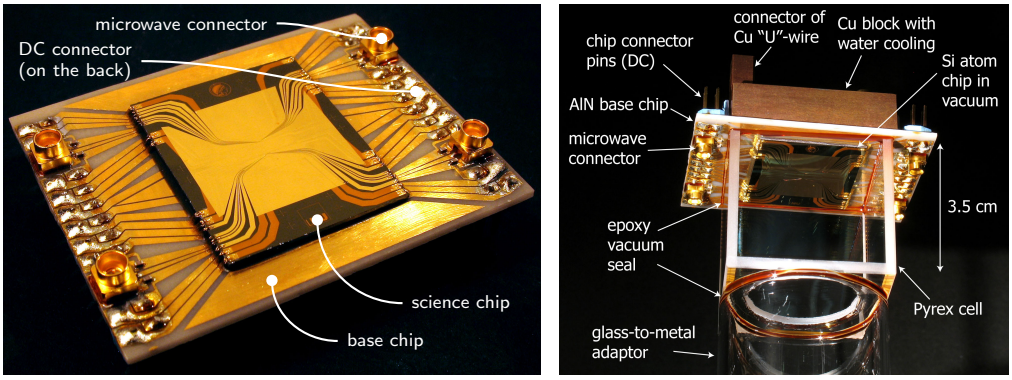

Figure 3.1: Photograph of the atom chip alone (left) and glued to the glass cell (right). Images taken from Ref. [42].

On top of the base chip, two 525 µm thick high-resistivity Si wafers are glued, known as the spacer chip and the science chip – the spacer chip being of course placed between the base and the science chip. The science chip is topped with two layers of gold wire structures: The lower one is 5 µm thick and is structured with interconnected wires that can be used in various configurations, including the dimple, U-shaped, and Z-shaped wires. The top one is 1 µm thick and contains two sets of wire structures, both able to carry DC and microwave (mw) currents. The two layers are separated by a 6 µm thick polyamide layer, which serves both as electrical insulator and as surface planariser. Besides the wire structures, the surface of the science chip is gold coated and is used as a mirror during the laser cooling stages.

Both DC and mw magnetic fields generated by the atom chip can be simulated with a program originally developed in Ref. [42]. The accuracy of the simulated mw amplitude was confirmed experimentally in Ref. [77, 78].

The atom chip is glued to a $(3\,\mathrm{cm})^3$ glass cell, forming the top wall of the so-called science chamber, where every stage of the experimental sequence takes place. The bottom of the glass cell is connected via a six-way stainless-steel cross to a 40 l/s ion pump[1], a Ti-sublimation pump[2], an ion pressure gauge[3], and three Rb dispensers[4]. The ion pump maintains a pressure between 5×10^{-10} mbar and 1×10^{-9} mbar (read from the pressure gauge). Once every few months, when the pressure surpasses 1×10^{-9} mbar (the typ-

[1]Varian VacIon Plus 40 Diode.

[2]A Ti filament driven by Vacom SUBLI-CON 51.

[3]Leybold Ionivac IE514 Extractor.

[4]Two SAES Getters RB/NF/3,4/12FT10+10 and one Alvatec AS-RbIn-5-F, all of which contain the natural mixture of Rb isotopes.

ical BEC lifetime at this pressure is $\sim 6\,\mathrm{s}$), we activate the Ti-sublimation pump. Out of the three Rb dispensers, only one of the SAES Getters is in operation, at the constant current of 2.35 A.

All inhomogeneous magnetic fields are produced by the wire structures on the atom chip, with one exception: On the back of the chip is attached a water-cooled copper block, which contains a U-shaped wire used to create the quadrupole field during the initial magneto-optical trapping stage (called *big U* wire). A water-cooled coil cage, composed of three Helmholtz coils, surrounds the science chamber, providing approximately homogeneous fields in all directions (called *bias fields*). In the x- and z-direction, the coils produce fields of $6.1\,\mathrm{G/A}$ and $1.7\,\mathrm{G/A}$, respectively. In the y-direction, two independent windings provide strong fields ($4.3\,\mathrm{G/A}$) and weaker but more stable fields ($1.7\,\mathrm{G/A}$). The water cooling of both the copper block and the coil cage are connected in series to a thermoelectric chiller[5].

In addition to the coil cage, around the science chamber there are a mw and a rf antenna used for collective spin rotations (see Sec. 3.3.2), fibre output couplers (see Sec. 3.2), and imaging optics (see Sec. 3.4). In order to protect the atoms from magnetic field fluctuations and ambient light, all the aforementioned components are enclosed in a single-layer μ-metal shield.

3.1.1 Magnetic trapping potentials

According to Eq. (2.12), the linear Zeeman shift produces a potential $V(\vec{r}) \coloneqq g_F m_F \mu_B B(\vec{r})$, which allows one to trap atoms in states with positive magnetic moment – low-field-seeking states – in a minimum of the magnetic field modulus $B(\vec{r})$. We produce such minimum by means of Ioffe-Pritchard traps [76, 79–81], which are the combination of a two-dimensional and a one-dimensional trap. Two-dimensional confinement results from the combination of the magnetic field from a current-carrying wire in, say, the x direction and a homogeneous magnetic field in the y direction: The two fields cancel each other along a straight line in the x direction, forming a quadrupole field in the yz plane. In order to have a non-zero field in the trap centre[6] and to obtain a harmonic potential, a homogeneous field is added in the x direction. Confinement in the third dimension is obtained by adding one or more current-carrying wires in the y direction. This can be done by substituting the straight wire with a Z-, U-, or H-shaped one, or by introducing an additional wire crossing the first one – the latter configuration is called *dimple* trap.

[5] Solid State Cooling Systems ThermoCube 10-400L-3G20-2-EF-DC-VD-AR.

[6] This has multiple advantages, such as the hindering of Majorana transitions [76] and the possibility to perform experiments at the magic field (see Sec. 2.3.1).

In our experimental apparatus we use a sequence of traps generated by the homogeneous fields and a Z-shaped wire (called *ioffe*) to capture the laser cooled atoms and move them close to the chip surface. Then, they are transferred into a similar trap produced by a longer Z-shaped wire (*long ioffe*) and subsequently into a sequence of dimple traps, where they are cooled into a BEC and manipulated [42]. The quadrupole field for the dimple traps is produced by the long ioffe wire, which provides a much weaker confinement in the x direction than the dimple. The Z-shaped wires and the one used for the first dimple trap (called *dimple* wire) are patterned on the lower layer of the science chip and carry currents up to a few Ampère. For the final dimple trap, on the other hand, we use three of the small wires on the top layer, which only carry up to a few tens of milli-Ampères.

3.1.2 Current sources

Magnetic fields are among the most critical experimental parameters to both the production and the manipulation of our BEC, as they determine the trapping potential and the Zeeman shifts. Thus, the noise performance and stability of the current sources producing them are crucial to the experiments presented in this thesis.

Most current sources currently in use are the same as described in Ref. [51], where their noise performance and stability were characterised. Based on the characterisation shown in Ref. [51], the current sources connected to the long ioffe wire and to the small wires were replaced by devices developed and built by Tilman Zibold. The new current source for the long Z-shaped wire delivers up to $\pm 1\,\mathrm{A}$ with $1\,\mathrm{MHz}$ bandwidth and 1×10^{-6} stability[7], while those for the small wires provide currents up to $\pm 10\,\mathrm{mA}$ with 2×10^{-6} stability. These replacements were a relevant improvement to the apparatus, because the magnetic fields produced by these wires define (together with the homogeneous fields) the trap where the final cooling stages and the manipulation of the BEC take place and are therefore particularly critical.

I will briefly summarise the properties of the other current sources, see Ref. [42, 51, 69, 74] for more details. The coils providing the homogeneous fields are driven by home-built bipolar current sources capable of up to $\pm 5\,\mathrm{A}$ [42, 82], except for the strong-field winding in the y direction, which is connected to a commercial unipolar device[8]; the latter delivers more current, up to $15\,\mathrm{A}$, but has worse noise and stability performance, hence it is only

[7] The stability was measured in laboratory conditions, with $<1\,^{\circ}\mathrm{C}$ temperature stability.
[8] FUG NLN 350M-20.

used during the initial stages of the experiment. The ioffe and the dimple wire are driven by home-built bipolar current sources [42,82] delivering of up to ±3 A and ±0.5 A, respectively. The current through the U-shaped wire patterned on the base chip (called *base U* wire), which is used during the laser cooling, is provided by a commercial bipolar source[9] capable of ±10 A. The big U wire in the copper block is driven by a commercial unipolar device[10], which delivers up to 70 A.

3.2 Laser system

In our experimental apparatus we use lasers to cool, optically pump, and detect atoms. We do this by addressing several transitions in the D2 line of ^{87}Rb, as shown in Fig. 3.2. The hyperfine splitting of the ground state $5^2S_{1/2}$ is 6.835 GHz, whereas in the excited state manifold $5^2P_{3/2}$ the splittings are on the order of hundreds of MHz. Therefore, it is possible to obtain all desired frequencies with two lasers detuned by roughly the hyperfine splitting of $5^2S_{1/2}$ from each other and acousto-optic modulators (AOMs).

The current laser system is described in detail in Ref. [51], from which Fig. 3.3 and Fig. 3.4 were taken. Both lasers are home-built interference-filter-stabilised diode lasers. The so-called master laser (*seed laser* in Fig. 3.3) is frequency locked to the crossover transition $F = 1 \leftrightarrow F' = (1, 3)$ of a Doppler-free saturated absorption spectroscopy. The slave laser is frequency locked to 6.705 GHz above the master laser frequency with an optical phase lock loop, see Ref. [83]. In order to produce enough cooling power, the light from the master laser is amplified by a tapered amplifier[11] (TA).

The light from both lasers is split into several different beams that pass through AOMs, which produce all desired frequencies and also provide amplitude and timing control of the laser pulses, see Fig. 3.3. The AOM signals are produced by rf generators based on voltage-controlled-oscillators (VCOs), whose frequency and amplitude can be controlled both manually and by means of analogue voltages and that are capable of TTL-controlled fast switching. The timing resolution of the laser pulses is limited by the control system to 10 µs, see Sec. 3.5. To minimise stray light from unused beams, we use mechanical shutters[12] with ~ 1 ms switching time.

All beams are coupled into single-mode polarisation-maintaining optical

[9] HighFinesse BCS106.
[10] Delta Electronic SM4575D.
[11] TOPTICA Photonics BoosTA Pro, controlled by DC HP.
[12] Stanford Research Systems SR475, controlled by SR470.

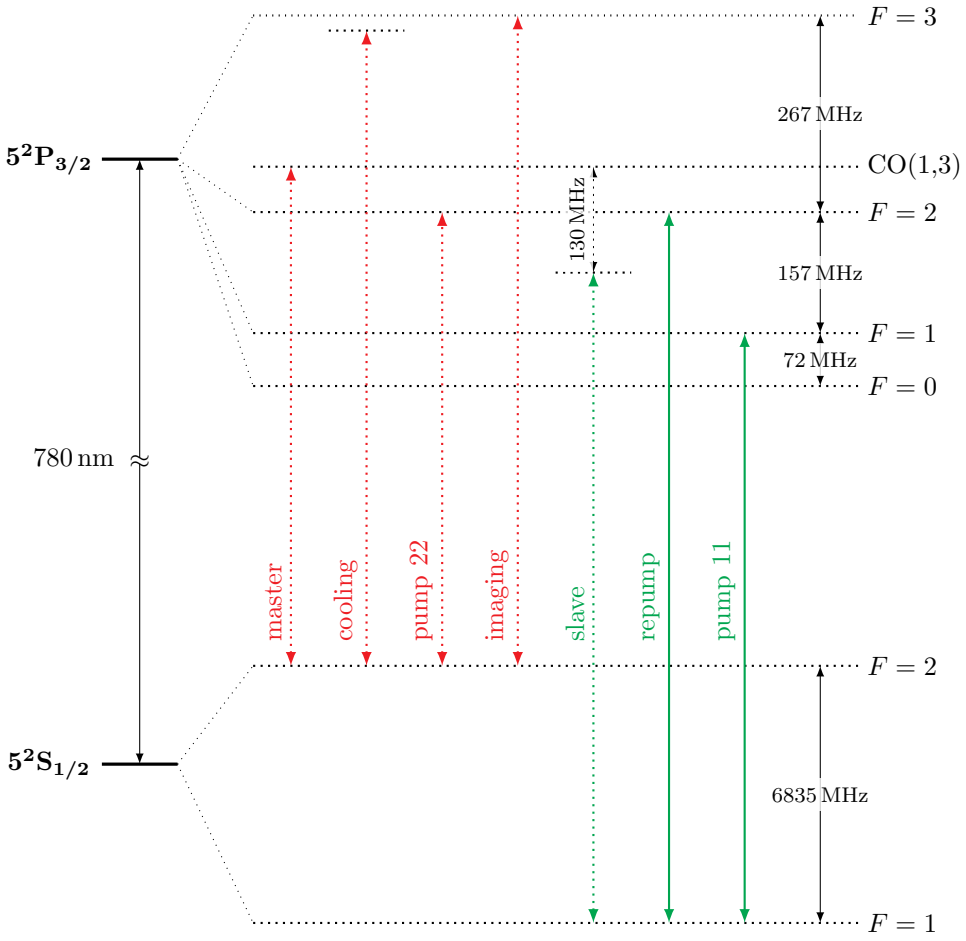

Figure 3.2: Level structure of the ^{87}Rb D2 line and laser frequencies used in our experimental apparatus. Red (green) indicates the frequencies obtained from the master (slave) laser.

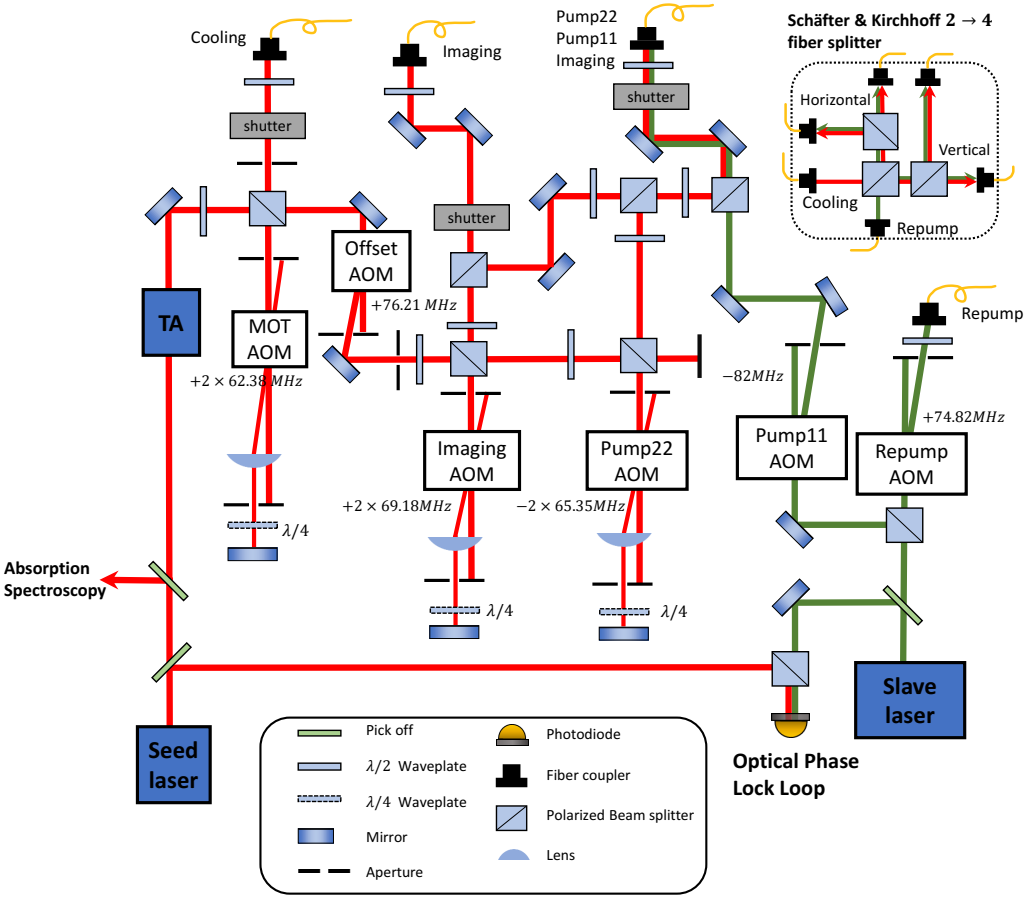

Figure 3.3: Schematic of the laser system. Figure taken from Ref. [51].

the chip surface and broad enough, providing cooling in both the y and z direction. Two horizontal beams provide cooling in the x direction. Together with the magnetic field generated by Helmholtz coils and the U-shaped wire, they form a mirror MOT as shown in Figure 3.5.

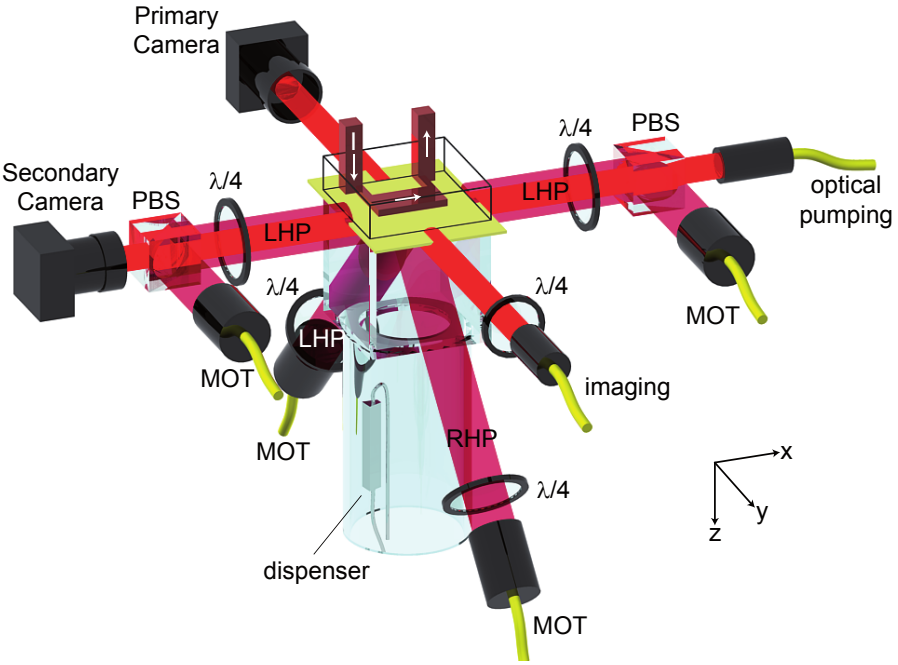

Figure 3.5 **Optics surrounding the science chamber.** Indicated are polarizing beam splitters (PBS), quarter-wave plates ($\lambda/4$), and right-hand and left-hand circular polarization of the MOT cooling beams (RHP and LHP, respectively). Figure adapted from [3].

As a benchmark for laser powers, the typical output power of the master laser is around 30 mW. The tapered amplifier module is able to produce up to 3.5 W of output power at a current of 4.3 A. We use the amplifier at a lower working current of 2.5 A to amplify the laser power to around 1.7 W, which is sufficient for our use.

3.1.4 Current sources and their noise characterization

Current sources play an important role in our experiment apparatus. In our experiment, we need current sources that meet different requirements. The current sources used in the experiment are described in earlier theses [50, 103, 108, 110]. Here we briefly summarize their up-to-date properties in Table 3.1.

During the MOT stage, quadrupole fields are needed. The wires involved are two U-shaped wires (both are no more than a single turn), therefore large currents are required. A current of 52 A is sent through the external U-shaped wire (Fig. 3.5), driven by a commercial

[13] Schäfter+Kirchhoff 48-FPC-2-4-780.

[14] Following the notation used in Ref. [69], here we use the term "radio frequency" to denote the range in the standard radio-frequency spectrum with lower frequency than microwave signals.

3.3 Radio-frequency and microwave generation

In our experimental apparatus we use radio frequency[14] (rf) and microwave (mw) signals for evaporative cooling, coherent spin rotations, and state-dependent dressing potentials. These signals are produced by several commercial function generators, all frequency locked to the 10 MHz outputs of a

GPS-disciplined oven-stabilised quartz reference[15].

3.3.1 Evaporative cooling

The final step to reach Bose-Einstein condensation in our apparatus consists of three stages of rf-induced evaporative cooling [84], each performed in a different dimple trap: The first two are frequency and amplitude ramps, which produce a BEC with a relevant thermal fraction. The third one is a constant signal at a frequency corresponding to much less than the condensation temperature, which has the effect of rendering the thermal fraction of the BEC negligible and stabilising the final atom number[16].

These signals are produced by a USB-controlled rf source[17], amplified by a temperature-stabilised amplifier[18] and emitted by a home-built square coil[19] placed outside of the science chamber [69]. The output of the rf generator is gated by a switch[20] controlled by one of the digital outputs present on the rf generator itself. Since these devices are also used to generate part of the signals used to coherently manipulate the internal state of the BEC, see Sec. 3.3.2, they are shown in the upper half of Fig. 3.6.

The coil-resistor system that constitutes the rf antenna is impedance matched to the 50 Ω transmission line for signals with a frequency of about 1.7 MHz, which is close to the frequencies used in the two final cooling stages, but completely mismatched at most frequencies used during the first rf ramp – up to 14 MHz. In order to minimise the interference effects due to reflections, a 6 dB attenuator[21] was inserted between the amplifier and the coil [51].

3.3.2 Coherent manipulation

As shown in Fig. 3.5, we drive the two-photon transition between $|1\rangle$ and $|2\rangle$ by off-resonantly coupling both states to the intermediate state $|F = 2, m_F = 0\rangle$, with matched detuning $\Delta_{\text{int}} \approx 2\pi \times 500\,\text{kHz}$. Since in our case the Rabi frequencies of the two transitions are much smaller than the detuning to the intermediate state, $\Omega_{\text{rf}}, \Omega_{\text{mw}} \ll \Delta_{\text{int}}$, the latter can be

[15] Stanford Research Systems FS752.

[16] Within a reasonable range, we can choose the atom number in the BEC by changing the frequency of the last evaporative cooling stage without observing any thermal fraction.

[17] Photonics Technologies VFG 150.

[18] Mini-Circuits LZY-22+, temperature stabilised by Thorlabs TED4015.

[19] The coil has 9 windings and 3 cm side length and is connected in series to a 10 Ω resistor. The combination has resistance 10.1 Ω and inductance 4.6 µH [69].

[20] Mini-Circuits ZASWA-2-50DR+.

[21] Mini-Circuits BW-S6W20+.

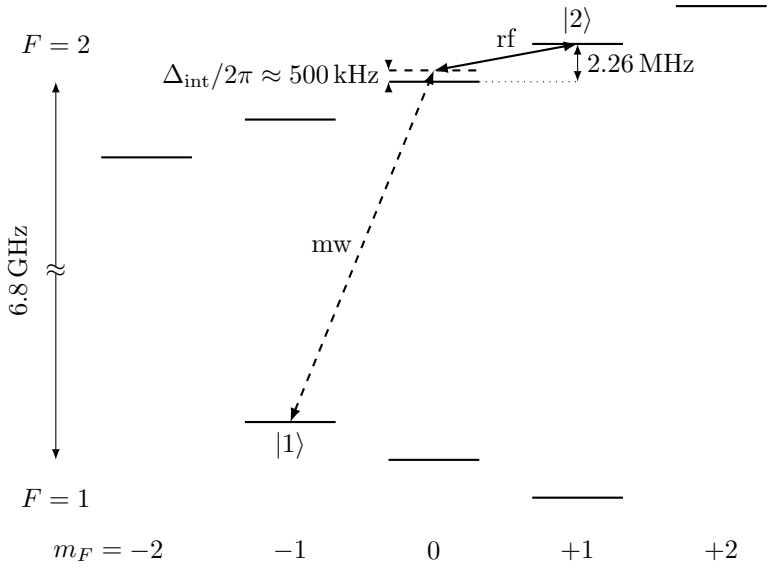

Figure 3.5: Level structure of ^{87}Rb at the magic field 3.23 G with the rf and mw frequencies used to drive the two-photon transition between $|1\rangle$ and $|2\rangle$.

adiabatically eliminated – in the same way as in Raman transitions [85]. The resulting behaviour is the same as that of a two-level system driven with Rabi frequency

$$\Omega \coloneqq \frac{\Omega_{\mathrm{rf}}\Omega_{\mathrm{mw}}}{2\Delta_{\mathrm{int}}}. \tag{3.1}$$

Any two-photon detuning,

$$\Delta \coloneqq \omega_{\mathrm{rf}} + \omega_{\mathrm{mw}} - \omega_{12}, \tag{3.2}$$

where ω_{rf} (ω_{mw}) is the rf (mw) frequency, affects the Rabi oscillations in the same way as a detuning in a two-level system – as long as $\Delta \ll \Delta_{\mathrm{int}}$. Note that the transition frequency ω_{12} is modified by the AC Zeeman shifts.

Thus, the effect of driving the two-photon transition for a time duration t (i.e. applying a *Rabi pulse*) can be written as a collective spin rotation

$$e^{-i\,\vec{\Omega}\cdot\hat{\vec{S}}t}, \tag{3.3}$$

where

$$\vec{\Omega} \coloneqq \begin{pmatrix} \Omega\cos(\varphi) \\ \Omega\sin(\varphi) \\ \Delta \end{pmatrix} \tag{3.4}$$

is the Rabi vector and φ is the combined phase of the two-photon signal [69].

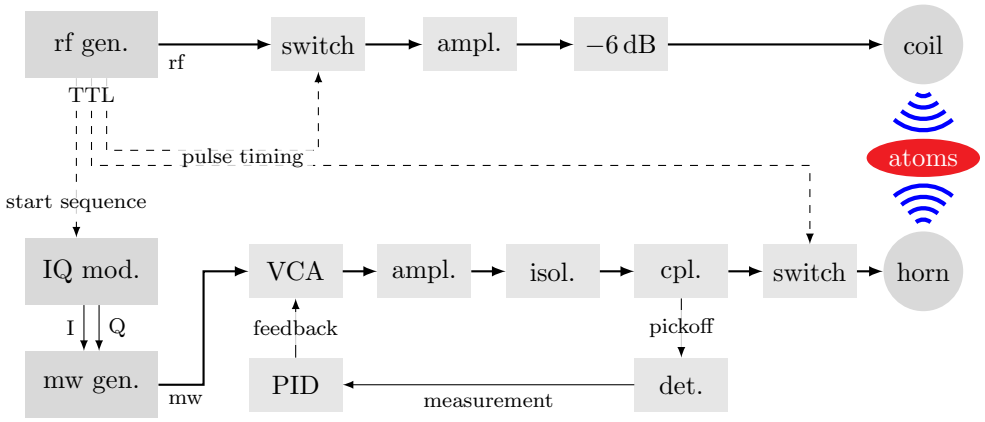

Figure 3.6: Schematic of the signal generation for the coherent manipulation of the BEC, where *gen.* stands for generator, *mod.* for modulator, *ampl.* for amplifier, *isol.* for isolator (here, composed of a three-port circulator and a 50 Ω terminator), *cpl.* for directional coupler, *det.* for mw power detector, *VCA* for voltage-controlled attenuator, and *PID* for PID controller.

Fig. 3.6 shows a schematic of the generation of the driving fields. The rf fields are produced by the same components used for the evaporative cooling, see Sec. 3.3.1. The mw signals are produced by an IQ-modulated mw generator[22], which receives the modulation signal from a two-channel arbitrary waveform generator[23], see appendix A. The mw signal is amplified[24] and passed through a three-way circulator[25], whose third port is terminated to eliminate reflections. To control the mw amplitude, the signal is sampled by a directional coupler[26] and measured by a temperature-stabilised mw detector[27]; the output of the detector is amplified[28] and used as measured value by an analogue PID controller[29], which receives the setpoint by the experiment control system (see Sec. 3.5) and feeds back on a voltage-controlled attenuator[30] connected to the output of the mw generator. The rf and mw signals are coupled to the atoms via antennae placed outside of the science chamber, so as to obtain a homogeneous field strength across the size of the

[22]Rohde & Schwarz SGS100A.
[23]Keysight 33522B.
[24]Kuhne electronic 682 TR UM.
[25]AEROTEK H15-1FFF.
[26]Pulsar CS20-10-435/1.
[27]Agilent 8471E.
[28]By a home-built current-to-voltage pre-amplifier based on an OPA111 low-noise operational amplifier.
[29]Stanford Research Systems SIM960.
[30]Pulsar AAT-25-479/251040.

BEC – which is necessary to drive collective-spin rotations [38]. The rf antenna (*coil* in Fig. 3.6) is the same described in Sec. 3.3.1, whereas the mw one is a rectangular waveguide, which was sawed off a coaxial-to-waveguide coupler[31] (*horn* in Fig. 3.6) [42].

At the beginning of every experimental run, both the rf generator and the IQ modulator are programmed with a sequence of frequencies, amplitudes, and phases. The rf sequence is started by a trigger given by the experiment control system (see Sec. 3.5), whereas the IQ sequence is triggered by one of the digital outputs of the rf generator, so as to get the best possible synchronisation between the two devices. All pulses are timed by gating the signals with absorptive switches controlled by the digital outputs of the rf generator[32], in order to guarantee the synchronisation of the rf and mw pulses – which is particularly important during the two-photon manipulations. All signal generators are frequency locked to the reference clock, see Sec. 3.3.

Microwave polarisation

In order to improve the state selectivity while driving coherent transitions in our system, it would be advantageous to use circularly polarised mw fields, in particular to suppress σ^- transitions – see Sec. 4.4.3. To this end, we tested several home-built and commercial circularly polarised antennae.

To measure the polarisation of mw radiation, we perform Rabi oscillations on single-photon transitions with different changes in m_F: We initialise the atoms in the state $|1\rangle = |F = 1, m_F = -1\rangle$ and irradiate them for variable times at the frequency resonant with the transition to $|F = 2, m_F = -2\rangle$, $|F = 2, m_F = -1\rangle$, or $|F = 2, m_F = 0\rangle$. The measured Rabi frequency is proportional to the respective polarisation component (σ^-, π, and σ^+) and matrix element ($-\sqrt{3/4}$, $-\sqrt{3/16}$, and $\sqrt{1/8}$, see Fig. 2.1).

After performing such experiments for different antennae placed in a variety of ways, it turned out that the best ratio between σ^+ and σ^- polarisation that we could achieve (2.45 amplitude ratio) is obtained by the original configuration, i.e. a linearly polarised antenna placed at the side of the quantisation axis at an angle of about 45° w.r.t. the atom chip surface. Understanding the precise reasons of this is not a trivial task, as many metal structures are present within a mw wavelength from the atoms. It would be possible, for example, that the roughly circular polarisation results from the superposition between the incoming mw field and its reflection off the atom chip.

[31] A-Info LB-OH-159-15-C-SF.

[32] MITEQ N147BNM2 for mw, Mini-Circuits ZASWA-2-50DRA+ for rf.

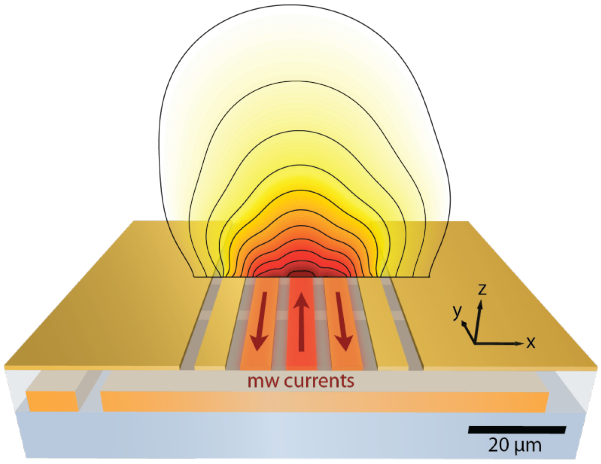

Figure 3.7: Schematic of the mw state-dependent potential generation. Figure taken from Ref. [69].

3.3.3 State-dependent potential

The collective spin rotations discussed in Sec. 3.3.2 are induced by homogeneous electromagnetic fields emitted by antennae placed far from the BEC. Some of the wire structures on the top layer of the science chip, on the other hand, were designed to serve as mw co-planar waveguide (CPW) and are able to irradiate the atoms with a strongly inhomogeneous mw field [42]. If the signals applied to these structures are off resonance with all transitions in the ^{87}Rb ground state, they create spatially dependent AC Zeeman shifts, which take the form of state-dependent potentials [42]

$$V_{\mathrm{mw}}^{1,m_F}(\vec{r}) = +\frac{\hbar}{4}\sum_{m'_F=-2}^{2}\frac{\left|\Omega_{1,m_F}^{2,m'_F}(\vec{r})\right|^2}{\Delta_{1,m_F}^{2,m'_F}} \propto B_{\mathrm{mw}}(\vec{r})^2, \tag{3.5}$$

$$V_{\mathrm{mw}}^{2,m'_F}(\vec{r}) = -\frac{\hbar}{4}\sum_{m_F=-1}^{1}\frac{\left|\Omega_{1,m_F}^{2,m'_F}(\vec{r})\right|^2}{\Delta_{1,m_F}^{2,m'_F}} \propto B_{\mathrm{mw}}(\vec{r})^2, \tag{3.6}$$

where Ω_{F,m_F}^{F',m'_F} and Δ_{F,m_F}^{F',m'_F} are the Rabi frequency and the detuning, respectively, relative to the transition $|F,m_F\rangle \leftrightarrow |F',m'_F\rangle$, and B_{mw} is the modulus of the mw amplitude.

Applying such a state-dependent potential to a two-component BEC shifts the trap minima of the two states away from each other, thereby reducing their overlap. As it can be seen from Eq. (2.21), this results in the activation of the one-axis twisting (OAT) term $\hbar\chi\hat{S}_z^2$ (which is negligible

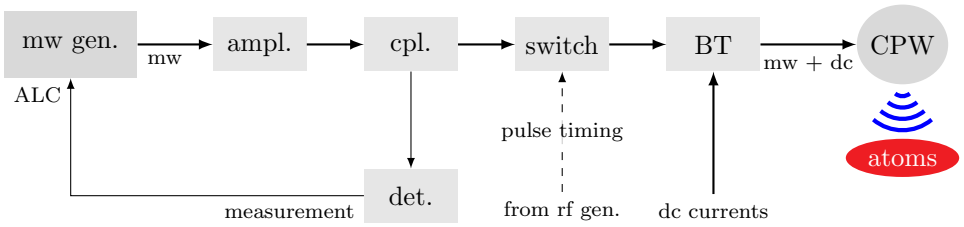

Figure 3.8: Schematic of the signal generation for the state-dependent dressing potentials, where *gen.* stands for generator, *ampl.* for amplifier, *cpl.* for directional coupler, *det.* for mw power detector, *ALC* for automatic level control (which is a built-in amplitude stabilisation feature of the mw generator), *BT* for bias tee, and *CPW* for co-planar waveguide.

for overlapped states) in the collective-spin Hamiltonian, see Eq. (2.17). It is thus possible to obtain a squeezed spin state (SSS) from a coherent spin state (CSS) by applying the state-dependent potential for a controlled time [34,60], see Sec. 2.3.5.

In the experiments presented in this thesis, we activate the OAT dynamics for a duration of up to ∼40 ms. Since the trap frequency in the direction of the splitting is ∼100 Hz, for the BEC to follow adiabatically the shift of the trap minima, the switching of the state-dependent potential would need to take a time comparable to the whole state evolution, resulting in a relevant increase in the total experiment duration. To avoid the additional atom losses and decoherence that this would induce, we switch the CPW mw abruptly. Due to this, when the potential is turned on, the two states start oscillating (typically in opposite directions, due to the sign difference between Eqs. (3.5) and (3.6)) and thus split and recombine periodically. In order to recover the overlap between them and to stop these dynamics, the potential needs to be switched off at a particular time of the oscillation. Therefore, there are discrete times for which we can activate the OAT term; these can be determined by observing the interferometric contrast of the final state, see appendix C. This phenomenon, known as *demixing-remixing dynamics*, is studied in detail for our experimental parameters in Ref. [51].

The fields used to create the state-dependent potentials are generated as shown in Fig. 3.8: The signal is produced by a mw generator[33], amplified[34], and sampled by a directional coupler[35]. The sampled signal is measured by a temperature-stabilised mw detector[36] and fed to the *automatic level*

[33] Agilent E8257D.
[34] Microsemi AML218P3203.
[35] Pulsar CS20-10-435/1.
[36] Agilent 8471E.

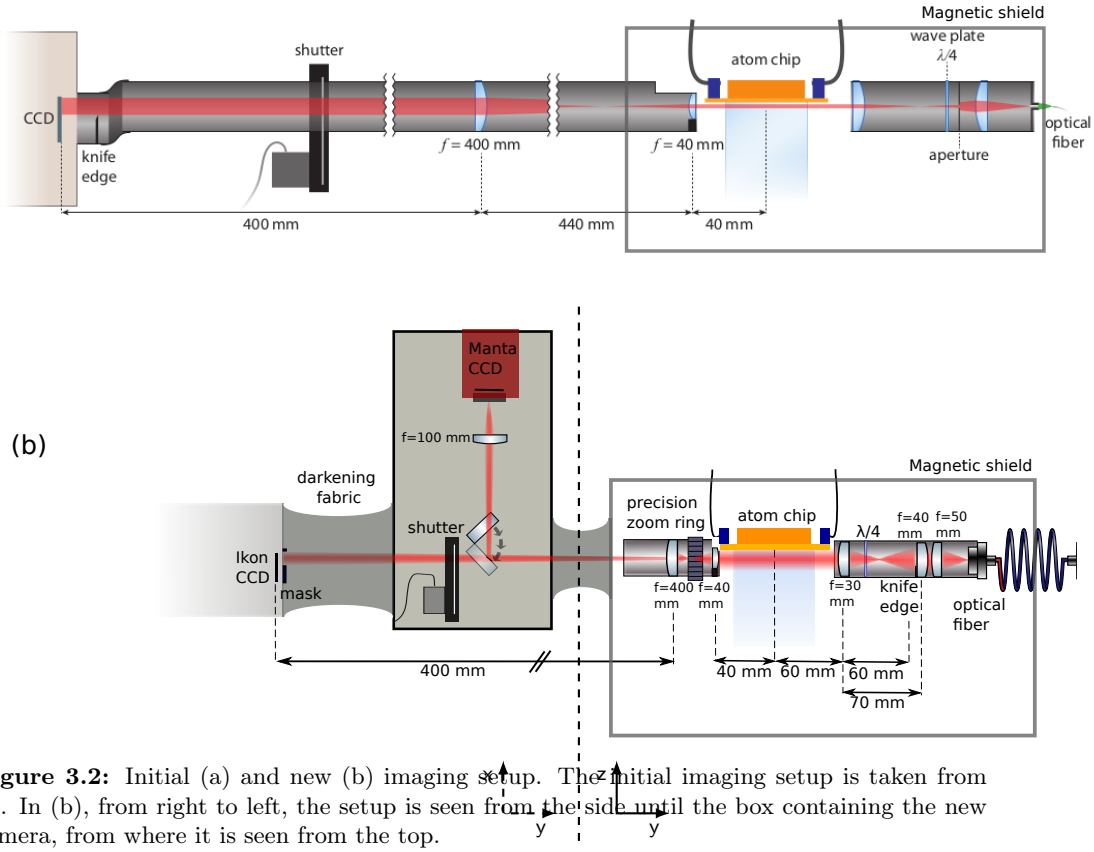

Figure 3.2: Initial (a) and new (b) imaging setup. The initial imaging setup is taken from [7]. In (b), from right to left, the setup is seen from the side until the box containing the new camera, from where it is seen from the top.

Figure 3.9: Schematic of the imaging system. Figure taken from Ref. [86]. The dashed line in the centre indicates a change in coordinate system, which is specified at the bottom.

A first modification was to rotate the Ikon camera by 90°, so that in the frame transfer mode, the CCD is now divided along the x-axis (the horizontal axis in Fig.3.1) instead of the z-axis (the vertical axis in Fig. 3.1) which is the axis of the fall of the atoms. Before, the field of view was extended in the x-direction, which was *control* (ALC) input of the internal attenuator, where it was used to stabilise the of view is extended in the z-direction, which enables us to image the atoms at mw amplitude. The mw generator is programmed at the beginning of every different points of the time of flight (see Fig. 3.3). It can also be advantageous experimental run and it is operated in continuous wave mode. The pulse if, in the future, one wants to split the BEC in more than two clouds. timing is provided by the rf generator – so as to guarantee the synchroni-

Another improvement was to get a flatter intensity of the imaging beam. Indeed, sation of the state-dependent potentials with the coherent manipulations – since the two dressed states are not imaged at the same position, having a spatially which gates the signal via an absorptive switch[37] placed after the directional inhomogeneous dressing field can induce inhomogeneous potentials related to the coupling field. The mw potentials are related to the atoms by the same wire atoms. structures used to produce the final dimple trap, the mw signal is summed We modified the dimensions of the imaging beam as follows. The beam is now to the DC current of the central wire by a bias tee[38], before being fed to the only collimated by one lens (f=50 mm), then it is resized by two lenses of focal atom chip. length f=40 mm and f=30 mm to reach a diameter of 6 mm, insuring a flat enough intensity on a central area of 1 mm² (less than 7% intensity variation), which corresponds to the region of the atoms. We replaced the iris by a knife

3.4 Imaging system

We detect the atoms by resonant absorption imaging [39, 87], which is based on comparing the shadow cast by the atoms in a circularly polarised laser beam resonant with a cycling transition (absorption image) with a reference image taken without atoms. We use the σ^+ cycling transition in the $F = 2 \rightarrow F' = 3$ component of the ^{87}Rb D2 line. Atoms in states with $F = 1$

[37] Miteq N147BDM2.
[38] UMCC BT-5000-HS

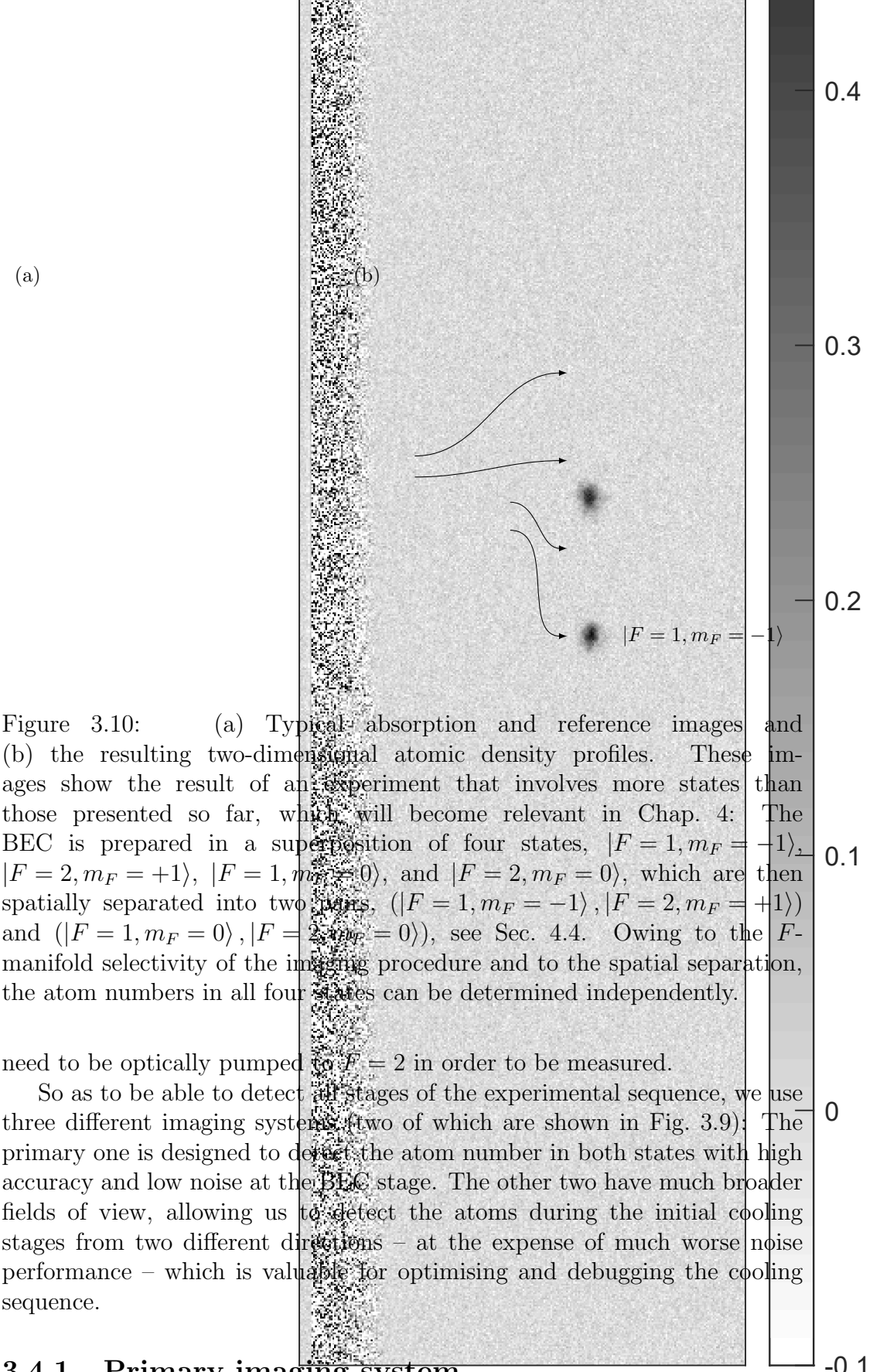

Figure 3.10: (a) Typical absorption and reference images and (b) the resulting two-dimensional atomic density profiles. These images show the result of an experiment that involves more states than those presented so far, which will become relevant in Chap. 4: The BEC is prepared in a superposition of four states, $|F = 1, m_F = -1\rangle$, $|F = 2, m_F = +1\rangle$, $|F = 1, m_F = 0\rangle$, and $|F = 2, m_F = 0\rangle$, which are then spatially separated into two pairs, $(|F = 1, m_F = -1\rangle, |F = 2, m_F = +1\rangle)$ and $(|F = 1, m_F = 0\rangle, |F = 2, m_F = 0\rangle)$, see Sec. 4.4. Owing to the F-manifold selectivity of the imaging procedure and to the spatial separation, the atom numbers in all four states can be determined independently.

need to be optically pumped to $F = 2$ in order to be measured.

So as to be able to detect all stages of the experimental sequence, we use three different imaging systems (two of which are shown in Fig. 3.9): The primary one is designed to detect the atom number in both states with high accuracy and low noise at the BEC stage. The other two have much broader fields of view, allowing us to detect the atoms during the initial cooling stages from two different directions – at the expense of much worse noise performance – which is valuable for optimising and debugging the cooling sequence.

3.4.1 Primary imaging system

The primary imaging system is used to perform collective spin measurements of the two-component BEC, which requires detecting the atom number in

both states. This is done sequentially: At the end of the experimental sequence, the atoms are released from the magnetic trap and allowed to expand while they fall under the effect of gravity. To control the expansion time (called *time of flight*, TOF), at the beginning of the free fall they are accelerated by a magnetic field gradient, which is produced by the long ioffe wire and applied for a typical duration of $\sim$1 ms. Once the BEC reaches the desired density and position, all atoms in states with $F = 2$ are detected by a σ^+ polarised laser pulse resonant with the imaging transition. The radiative pressure and the recoils from the re-emitted photons cause the involved atoms to accelerate and diffuse, making them undetectable by any further pulse. Subsequently, the atoms in states with $F = 1$ are optically pumped to $F = 2$ and detected by an imaging pulse identical to the first one. Finally, a third image without atoms (the reference image) is recorded. An example of typical absorption and reference images and of the extracted two-dimensional atomic density profiles is shown in Fig. 3.10.

With respect to previous PhD theses [38, 51, 69], major changes were brought to this part of the apparatus during Clara Piekarski's master's thesis [86]. In particular, the illumination optics, the imaging objective, and the spatial orientation of the camera were modified, see Fig. 3.9.

The illumination optics were designed to produce collimated light at the position of the atoms, while imaging a knife edge[39] at that same position. This ensures that the atom chip is not illuminated and that a sharp image of the knife edge is formed on the camera sensor, minimising the related diffraction effects. In addition to what is shown in Fig. 3.9, an iris[40] used for alignment is mounted a few millimetres before the knife edge. All these components are now mounted in a Thorlabs cage system, which makes it easy to adjust their longitudinal position. All metallic components were chosen to be made of non-magnetic materials – mainly aluminium.

The imaging objective is no longer in a $4f$ configuration. Rather, the two objective lenses are placed as close to each other as possible, to minimise losses and stray light from reflections. Since the alignment of the objective is very sensitive to the position of the first lens[41], the latter is mounted on a precision helical housing[42]. In addition to this, the whole objective is mounted in a way that ensures both stability and precise adjustment in both transverse directions. The focal lengths of the objective lenses are 40 mm and 400 mm, respectively. Thus, the image of the atoms is formed at about

[39] Thorlabs VA100C/M, from which we removed one blade to obtain an adjustable knife edge.

[40] Thorlabs CP20D.

[41] Melles Griot 06 LAI 005/076.

[42] Thorlabs SM1ZM

400 mm from the second lens and is magnified by about 10 times. The precise magnification factor is 9.90(10), which was determined by recording the cloud position for different TOFs and fitting it with a free fall trajectory.

The objective is mounted with a system of anodised aluminium tubes, whose interior was coated with velvet to minimise internal reflections. Outside of the magnetic shield, the optical path is protected against ambient light by darkening fabric. Before reaching the camera sensor, the imaging beam passes through a large-aperture shutter[43], which prevents the sensor from being exposed to stray light during the cooling stages. The shutter is placed in the same darkened box as one of the secondary imaging systems; to protect the experiment from the vibrations it produces, it is mounted on a sorbothane layer.

We use a back-illuminated deep-depletion CCD camera[44] (*Ikon* in Fig. 3.9), whose sensor is cooled by a thermoelectric element (typically at −80 °C) and reaches a quantum efficiency of 0.9 at our wavelength. In order to take images in rapid succession, we operate the camera in the so-called frame transfer mode: The images are recorded on a fraction of the CCD, while the rest is covered by a mask made of anodised aluminium foil and placed a few millimetres from the sensor. In between the exposures the camera shifts the images into the darkened region, allowing us to take pictures at 1.4 ms from each other.

While testing the changes to the imaging system, we noticed that the part of the darkened region close to the edge of the mask is exposed to small amounts of stray light. To ensure that the reference image is comparable to the absorption ones, we decided to expose 1/4 of the sensor and perform four imaging pulses – in this way the amount of stray light received by the three images is very similar.

The frame transfer mode of the camera works in a specific direction: CCD rows are shifted into the readout direction. Thus, the sensor can only be subdivided into horizontal slices. However, since the atoms are detected during the free fall, it is more useful to have a vertically elongated detection region. We therefore rotated the camera by 90°, obtaining a field of view of 0.34×1.34 mm.

Measuring different spin directions

Since the primary imaging system is able to detect the atom number in the two states $|1\rangle = |F = 1, m_F = -1\rangle$ and $|2\rangle = |F = 2, m_F = +1\rangle$, the only collective spin component that can be directly measured is $\hat{S}_z$. Other spin

[43] Sutter SmartShutter.

[44] Andor Ikon-M DU934N-BR-DD.

directions can be measured by performing a collective spin rotation before detection: According to Eq. (3.3), a resonant Rabi pulse with pulse area Ωt and phase φ can be written as the collective spin rotation

$$\hat{U}_{\Omega t,\varphi} = e^{-i\Omega t(\cos(\varphi)\hat{S}_x + \sin(\varphi)\hat{S}_y)}. \tag{3.7}$$

Choosing $\Omega t = \pi/2$ (a so-called $\pi/2$ pulse) and $\varphi = 0$ results in a collective spin rotation by $\pi/2$ around the x axis, which corresponds to a change of basis between y and z, $\hat{U}_{\frac{\pi}{2},0}\hat{S}_y\hat{U}^\dagger_{\frac{\pi}{2},0} = \hat{S}_z$. Similarly, $\Omega t = \pi/2$ and $\varphi = \pi/2$ yields a $\pi/2$ rotation around the y axis, corresponding to a change of basis between x and z, $\hat{U}_{\frac{\pi}{2},\frac{\pi}{2}}\hat{S}_x\hat{U}^\dagger_{\frac{\pi}{2},\frac{\pi}{2}} = \hat{S}_z$. Thus, performing a $\pi/2$ pulse with phase $\varphi = 0$ ($\varphi = \pi/2$) before detecting $\hat{S}_z$ results in effectively measuring $\hat{S}_y$ ($\hat{S}_x$).

3.4.2 Secondary imaging systems

Besides detecting BECs, it is important to image all cooling stages for optimising and debugging the experimental sequence. Since the field of view of the primary imaging system is too narrow for this, we have two secondary systems, oriented perpendicular to each other.

The first one, not shown in Fig. 3.9, detects the atoms with a laser beam in the $-x$ direction, which is carried by the fibre used for optical pumping – i.e. perpendicular to the main imaging system. The images are produced by an objective with magnification factor 2.23 and acquired by a compact CCD camera[45], resulting in a field of view of $2.9 \times 2.1\,\mathrm{mm}$. More information about this system can be found in Ref. [69].

The second one was added during Clara Piekarski's master's thesis [86] in order to extend the field of view in the direction of the main imaging system. Owing to this, we are now able to image the early stages of the experimental sequence from two different directions, making it possible to obtain complete information about the shape and position of the atomic cloud. As shown in Fig. 3.9, this imaging system uses the same imaging beam (deviated by a mirror with kinematic mount) and objective as the main system, but with an additional lens with focal length 100 mm that reduces the magnification to 3.39(1). The images are acquired by a compact CMOS camera[46] (*Manta* in Fig. 3.9), which yields a field of view of $3.3 \times 3.3\,\mathrm{mm}$. The kinematic mirror, the 100 mm lens, and the Manta camera are placed in a darkened box (which also fits the shutter of the main camera) consisting of an elevated breadboard between the magnetic shield and the Ikon camera.

[45] Allied Vision Guppy F-044B NIR.
[46] Allied Vision Manta G-419 NIR.

Due to the limited frame rate of both these compact cameras, the secondary imaging systems are only able to take one absorption image per experimental run, making it impossible to detect both states: We can either measure only the states with $F = 2$ or the sum of $F = 2$ and $F = 1$ (by optically pumping the latter to $F = 2$ before detection). Since these imaging systems are used to image early stages of the experimental sequence, where no superposition state is prepared, this is not a limitation.

3.4.3 Imaging calibration

We can calculate the two-dimensional atomic density profile from the absorption and the reference image by means of the Beer-Lambert law [87],

$$n_{2\mathrm{D}} = \frac{1}{\sigma_0}\left(\ln\left(\frac{I_{\mathrm{ref}}}{I_{\mathrm{abs}}}\right) + \frac{I_{\mathrm{ref}} - I_{\mathrm{abs}}}{I_{\mathrm{sat}}}\right), \tag{3.8}$$

where I_{abs} (I_{ref}) is the intensity profile of the absorption (reference) image, $\sigma_0 \coloneqq 3\lambda^2/2\pi$ is the resonant absorption cross section of the imaging transition, $I_{\mathrm{sat}} \coloneqq 2\pi^2\hbar c\Gamma/3\lambda^3$ is its saturation intensity, λ is its wavelength, Γ is its natural line width, $\hbar$ is the reduced Planck constant, and c is the vacuum speed of light. The imaging transition is the σ^+ cycling transition in the $F = 2 \to F' = 3$ component of the ^{87}Rb D2 line ($\lambda = 780\,\mathrm{nm}$, $\Gamma = 2\pi \cdot 6.07\,\mathrm{MHz}$, $I_{\mathrm{sat}} = 1.67\,\mathrm{mW/cm^2}$, [52]), which allows us to detect all atoms in states with $F = 2$.

The images measured by the camera correspond to the photon count matrices $A_{ij} = \langle I_{\mathrm{abs}}\rangle_{ij}\, q\, p\, t/E_\lambda$ and $R_{ij} = \langle I_{\mathrm{ref}}\rangle_{ij}\, q\, p\, t/E_\lambda$, where $\langle\cdot\rangle_{ij}$ is the mean over the pixel with index (i, j), q is the quantum efficiency of the camera, p the effective pixel area[47], t the exposure time, and $E_\lambda = 2\pi\hbar c/\lambda$ the energy per photon. Substituting I_{sat} with its definition, we obtain the atom number in the pixel with index (i, j),

$$N_{ij} = \frac{p}{\sigma_0}\ln\left(\frac{R_{ij}}{A_{ij}}\right) + \frac{2}{q\,t\,\Gamma}\left(R_{ij} - A_{ij}\right). \tag{3.9}$$

In order to correct for stray light and back illumination of the camera sensor, once a day we take an image without atoms nor probe light (dark image), which is subtracted from both the absorption and the reference image.

Eqs. (3.8) and (3.9) are valid for the resonant coupling to a collection of two-level systems by a perfectly σ^+ polarised laser beam with negligible losses between the atoms and the camera. It is also assumed that none of

[47] The effective pixel area is the area captured by one pixel at the position of the atoms, i.e. the pixel area divided by the square of the magnification factor of the imaging objective.

the re-emitted photons are absorbed by other atoms in the condensate. In order to take into account the atomic multi-level structure and experimental imperfections, we introduce the correction factors α for I_{sat} and β for σ_0, which have to be determined experimentally. Due to the atomic structure, these parameters differ for the detection of different states. Eq. (3.9) can be thus re-written for the detection of state $|k\rangle$ as

$$N_{ij} = \frac{1}{\beta_k}\left[\frac{p}{\sigma_0}\ln\left(\frac{R_{ij}}{A_{ij}}\right) + \frac{2}{\alpha_k\, q\, t\, \Gamma}\left(R_{ij} - A_{ij}\right)\right], \tag{3.10}$$

where α_k and β_k are the correction factors relative to state $|k\rangle$. The calibration of the imaging system consists of the experimental determination of these correction factors for all involved states. Since the experimental criteria that we use to demonstrate entanglement and the EPR paradox (Eqs. (4.3) and (4.2)) depend on the atom number, the results presented in this thesis rely on the accuracy of this procedure.

Despite the correction factors, Eq. (3.10) is based on an approximate model. Thus, the calibration measurements are performed with settings as close as possible to those used in the experiments the calibration is to be applied to. This includes choosing a similar atom number, imaging pulse duration and intensity, cloud expansion time, etc. As opposed to previous work performed with our apparatus, the experiments presented in this thesis involve mainly equal superpositions of the four states $|F = 1, m_F = -1\rangle$, $|F = 2, m_F = +1\rangle$, $|F = 1, m_F = 0\rangle$, and $|F = 2, m_F = 0\rangle$, see Chap. 4. This does not change the imaging calibration procedure substantially, but it requires preparing a similar distribution of the atoms among these states. The pulse sequences used to this end are devised to avoid the off-resonant coupling to unwanted transitions discussed in Sec. 4.4.3, which, however weak, would affect the atom number.

The calibration procedure, described in detail in Ref. [51], consists of three types of measurement. Firstly, the conversion from absorbed light to atom number is rendered independent of the laser intensity following the method described in Ref. [87]: Having fixed the imaging pulse duration, the atoms are prepared in an equal superposition of all four states and detected with probe intensities ranging from $\approx 0.5 I_{\mathrm{sat}}$ to $\approx 2 I_{\mathrm{sat}}$, see Fig. 3.11. For each state $|k\rangle$, the parameter α_k is chosen to minimise the dependence of the detected atom number on the light intensity – paying special attention to the values close to the typical operation point, $\approx 1.4 I_{\mathrm{sat}}$.

Secondly, the relative detectivity of the four states is calibrated: Different superposition states are prepared by driving Rabi oscillations, see Fig. 3.12. The ratios between the β_k are chosen to make the total detected atom number independent of the distribution of the atoms among the four states.

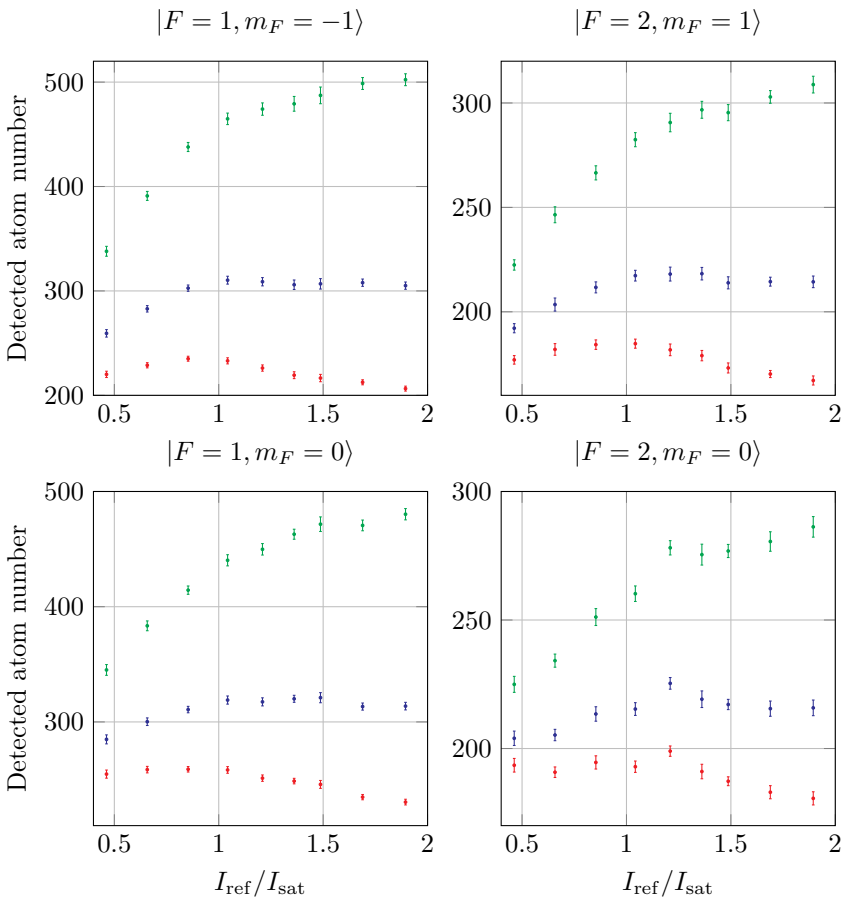

Figure 3.11: Detected atom number in the four involved states as a function of the probe intensity (estimated based on the reference image) for the chosen values of α_k (blue), for half of the chosen values (green), and for twice the chosen values (red). In the experiment shown here, the atoms are prepared in an equal superposition of the four states. The detected atom number varies from state to state due to the β_k not having been calibrated yet (i.e. still being equal to 1).

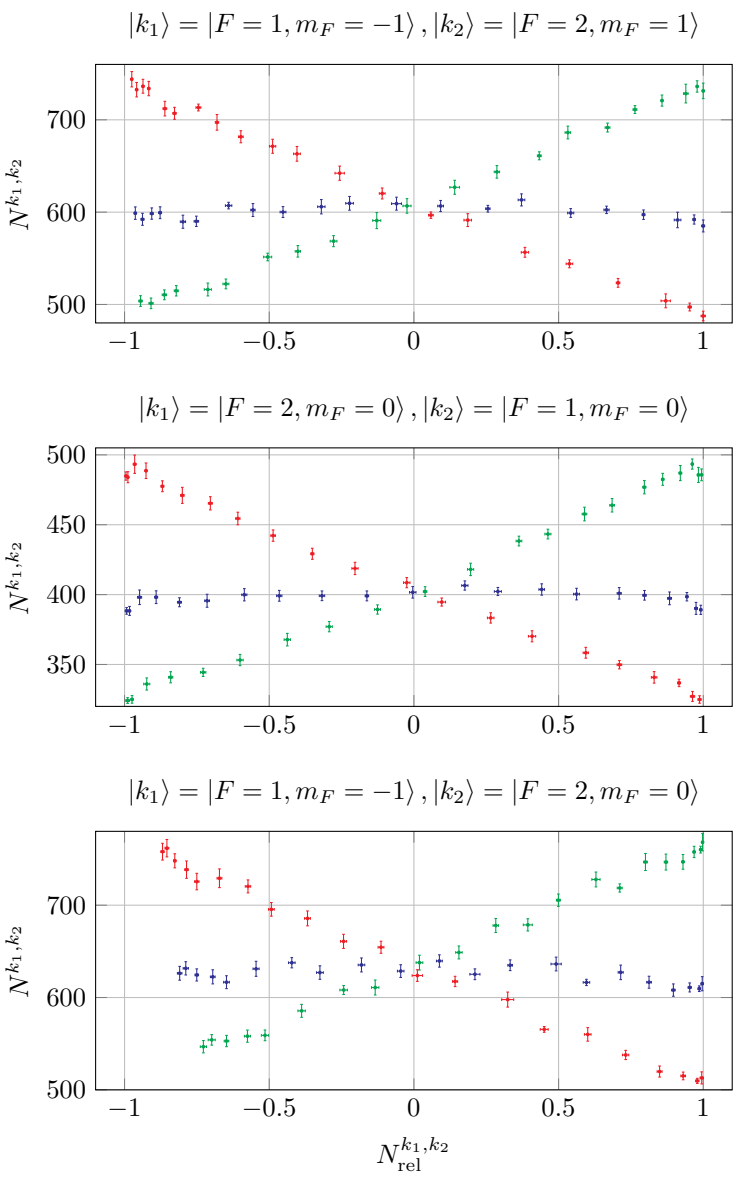

Figure 3.12: Total detected atom number $N^{k_1,k_2} := N_{k_1} + N_{k_2}$ as a function of the normalised atom number imbalance $N^{k_1,k_2}_{\text{rel}} := (N_{k_1} - N_{k_2})/N^{k_1,k_2}$ for the chosen ratios β_{k_1}/β_{k_2} (blue), for 2/3 of the chosen ratios (green), and for 3/2 of the chosen ratios. The detected atom number varies from state to state due to the β_k not having been fully calibrated yet at this stage – to determine the optimal ratios we vary β_{k_1} and β_{k_2} starting from 1.

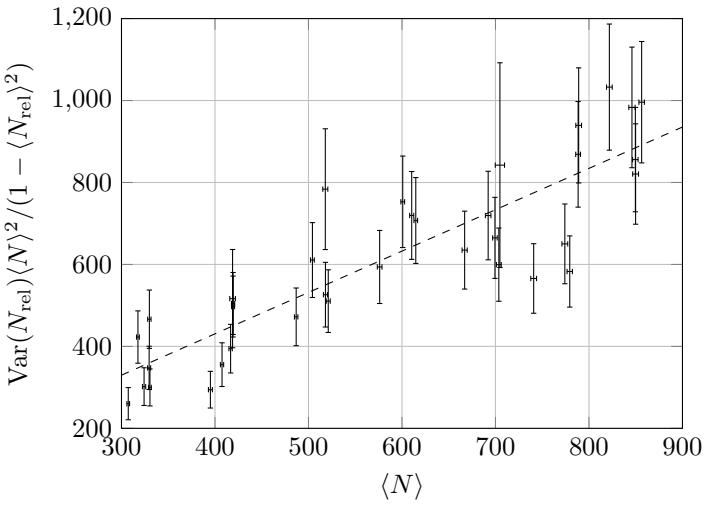

Figure 3.13: Projection noise of a CSS as a function of the atom number. The atoms are prepared in an equal superposition of all four relevant states, but only $|F=1, m_F=-1\rangle$ and $|F=2, m_F=+1\rangle$ are considered in this plot. Each data point represents a group of ∼100 repetitions. The dashed line shows a linear fit of the data. In the calibration procedure, the β_k are chosen to be such, that the slope of the linear fit is equal to 1.

Lastly, the total atom number is calibrated by observing the projection noise of a coherent spin state (CSS) as a function of the atom number [88], which is varied by changing the frequency of the last rf cooling stage, see Fig. 3.13: From binomial statistics, projection noise constitutes the linear component in

$$\mathrm{Var}(N_{\mathrm{rel}})\langle N\rangle^2 = (1-\langle N_{\mathrm{rel}}\rangle^2)\langle N\rangle + \sigma^2_{\mathrm{det},1} + \sigma^2_{\mathrm{det},2} + \sigma^2_{\mathrm{pulse}}\langle N\rangle^2, \qquad (3.11)$$

where $N_{\mathrm{rel}} \coloneqq (N_1 - N_2)/(N_1 + N_2)$ is the normalised atom number imbalance, $N \coloneqq N_1 + N_2$ is the total atom number, $\sigma^2_{\mathrm{det},k}$ is the variance associated with the detection noise of state $|k\rangle$, and $\sigma^2_{\mathrm{pulse}}$ is the variance originating from pulse area noise, which in our apparatus is negligible w.r.t. the other terms. Since the optical density of our atomic cloud is much smaller than 1, detection noise (which is mainly composed of photon shot noise, see Sec. 3.4.4) can be considered as independent of the atom number. Pulse area noise depends on the homogeneous coupling to the atoms of the mw and rf fields described in Sec. 3.3.2 and is thus also independent of the total atom number.

In order to perform the total atom number calibration measurement close to the relevant experimental parameters, we prepare an equal superposition

State	α_k	β_k
$\|F = 1, m_F = -1\rangle$	1.4158	0.8408
$\|F = 2, m_F = +1\rangle$	2.6061	0.5935
$\|F = 1, m_F = 0\rangle$	1.7757	0.7436
$\|F = 2, m_F = 0\rangle$	3.6252	0.5237

Table 3.1: Imaging correction parameters resulting from the calibration procedure described in Sec. 3.4.3.

of the four states mentioned above and consider the CSS constituted by two of them – typically $|F = 1, m_F = -1\rangle$ and $|F = 2, m_F = +1\rangle$. Enforcing the correct slope of the projection noise as a function of the atom number allows us to determine the combined detectivity of these two states, from which all β_k can be extracted via the ratios obtained as described above.

The results of the calibration procedure are listed in Tab. 3.1. The fact that all β_k are smaller than one indicates a smaller effective coupling strength of the atoms to the probe light than in the ideal case. Similarly, the values of all α_k are larger than one, which reflects the fact that a larger detected intensity is required to saturate the imaging transition. Both of these effects can be explained by the multi-level structure of the atoms and by the experimental imperfections mentioned at the beginning of this section.

3.4.4 Imaging noise and typical imaging parameters

Since the criteria Eqs. (4.2) and (4.3) are based on measuring quantum noise, any source of technical noise directly affects our results and should thus be minimised. This includes, of course, imaging noise, which in our experimental apparatus is mainly composed of photon shot noise: The average camera counts per pixel are ~ 5000, which corresponds to a photon shot noise of $\sigma_{\mathrm{psn}} \sim 70$ counts, whereas the camera manufacturer specifies a readout noise of $\sigma_{\mathrm{camera}} = 6.2$ counts for the settings we use. To minimise the detection noise, we optimise both the imaging parameters and the data analysis.

Due to the signal-to-noise ratio related to photon shot noise, the imaging noise can be improved by increasing the number of photons scattered during the process, which can be done by increasing either the imaging light intensity or the pulse duration. However, the intensity is chosen to be $\approx 1.4 I_{\mathrm{sat}}$, because around this value it is possible to perform a robust atom number calibration. Hence, we maximise the pulse length. The limitation to this is the atom diffusion caused by photon scattering, which increases the cloud size and forces us to analyse larger regions of interest, causing us to include detection noise from a larger area and eventually outbalancing the benefits of

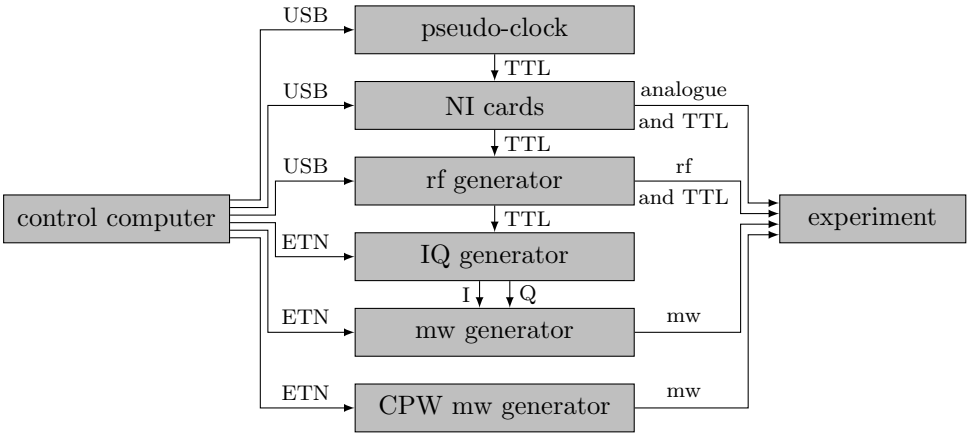

Figure 3.14: Schematic of the experiment control.

this strategy. We find the lowest imaging noise for a pulse duration of 70 µs. During this time the radiation pressure accelerates the atoms, inducing a relevant Doppler shift. To maintain the resonance throughout the process, we chirp the frequency of the imaging pulses.

Since every pixel contributes to the imaging noise, we choose the regions of interest for counting atoms to be as small as possible, while still including nearly all of the atomic signal. We do this by selecting elliptical regions that include ≈97 % of the total detected atom number, see appendix B. To avoid any artificial noise reduction due to the small discarded signal (see the supplementary materials of Ref. [30] for a discussion of this effect), we perform the atom number calibration after the region of interest has been determined.

Finally, we use a fringe removal algorithm to produce optimised reference images with linear combinations of measured reference images [89]. Besides minimising the effect of interference fringes on the reference images, this procedure strongly reduces the contribution of photon shot noise of the reference images.

The resulting detection noise, which we measure by taking images without atoms, corresponds to about $\sigma_{\mathrm{det}} \approx 3$ atoms in every state.

3.5 Experiment control and data acquisition

The experiment control, which was built during Simon Josephy's master's thesis [90], is centred around a computer running the Labscript suite [91] (the *control computer*), see Fig. 3.14. Most devices – e.g. current sources and AOM drivers – are controlled via analogue and digital voltages provided

by National Instruments I/O cards[48] (*NI cards*). The NI cards are stacked in a DC powered rack[49], which is connected to the control computer via an optical Thunderbolt 3 cable[50]. Their shared clock is provided by a pseudo-clock[51], which is connected to the control computer via USB. The function generators (see Sec. 3.3) are too complex to be fully controlled by the NI cards and are connected to the control computer by ethernet (*ETN* in Fig. 3.14) or USB.

At the beginning of every experimental run, the pseudo-clock, the NI cards, and the function generators are programmed by the control computer. This amounts to transmitting a sequence of instructions to these devices, with the exception of the mw sources, which are operated in continuous-wave mode and are just set to a given frequency and amplitude. After receiving a software trigger, the pseudo-clock manages the timing of the experiment by sending a trigger to the NI cards every time they have to advance by one step in their sequence. The rf generator, which provides the rf signal both for the evaporative cooling and for the coherent manipulations of the BEC, executes its sequence sector by sector, every time after receiving a trigger from the NI cards. The IQ modulator executes its sequence after receiving a trigger from the rf generator, which allows for a better synchronisation between these two devices than what would be possible by triggering both of them with the NI cards.

The cameras (see Sec. 3.4) are controlled by a separate computer running MatCam[52], an acquisition program written in Matlab [69]. At the beginning of every experimental run, the control computer transmits to MatCam some information about the experimental parameters, which are saved together with the measured data. In order to guarantee the synchronisation with the experimental sequence, the arming of the camera and the exposure are started by a trigger from the NI cards.

With respect to the previous version of the control system (described in Ref. [69]), the current one has a few advantages. First of all, Labscript is more flexible than the previous program (GoodTime): Among others, it

[48] Three PXI-6733 cards, for a total of 24 analogue I/O channels with 16 bit resolution, and two PXIe-6535 cards, for a total of 64 digital I/O channels. Every PXI-6733 card is connected to the devices via the breakout box BNC-2110, whereas the breakout box for the PXIe-6535 has been custom built for us by the electronics workshop of the Physics Department of the University of Basel.

[49] PXIe-1082DC, powered by the DC current supply Rhode&Schwarz HMP2020.

[50] Areca KAB-THB3/THB3-1500.

[51] PineBlaster, a pseudo-clock programmed by the developers of the Labscript Suite to run on the Digilent chipKIT Max32 board.

[52] The Ikon camera is connected to the MatCam computer via USB, the Guppy via FireWire, and the Manta via ethernet.

is relatively simple to integrate devices into Labscript, whereas GoodTime could only control the NI cards and Matlab was used to interface it with the rest. Secondly, we improved the separation between low-noise signals and devices from noisier ones. E.g., we no longer stack the NI cards inside the control computer, we do not use the digital I/O channels of the analogue NI cards any more, and we group devices by noise level both in the connections to the NI cards and in the power outlets. Thirdly, we simplified the connections to ground by introducing galvanic isolation between several devices, e.g. between the control computer and the NI cards[53], in most ethernet connections[54], in some USB connections[55], and in some TTL connections[56]. Also, many devices – including the NI cards – are powered by floating-ground current sources. Of course, since the experimental apparatus is composed of tens of interconnected devices, it is impossible to obtain ideal ground connections and complete isolation between different devices, but its stability has improved to the point where it can run for days unattended.

3.6 Typical experimental sequence

The experimental sequence takes place entirely in the science chamber. The atoms are initially collected from the background gas by a magneto-optical trap (MOT), whose parameters have been chosen to maximise the number of trapped atoms: The cooling laser frequency is set to $3.3\,\Gamma$ below the cooling transition and the quadrupole field is produced by sending 52 A through the big U wire (see Sec. 3.1). After a typical "MOT loading" time of 12 s, the atoms are transferred to a smaller MOT that cools them further and brings them closer to the atom chip ($-5.5\,\Gamma$ detuning to the cooling transition and quadrupole field produced by 3.25 A through the base U wire, see Sec. 3.1.2). The final laser cooling stage consists of an optical molasses with $-14\,\Gamma$ detuning to the cooling transition, which yields $\sim 5 \times 10^5$ atoms with a temperature of $\sim 2\,\mu$K.

The laser cooled atoms are optically pumped to the state $|F = 1, m_F = -1\rangle$, trapped in a Ioffe-Pritchard trap generated by the ioffe wire and the y bias field, and moved closer to the chip surface. Subsequently, the ioffe wire is substituted by the long ioffe wire and a dimple trap is produced by the dimple wire. In all magnetic traps the x bias field is kept at a non-zero value, so as to render the traps harmonic and to prevent Majorana flips.

[53] Using the optical cable Areca KAB-THB3/THB3-1500.
[54] Using the network isolator Delock 62619.
[55] With the USB isolation HUB Analog Devices EVAL-CN0158-EB1Z.
[56] With opto-couplers.

After having been loaded into the dimple trap, the atoms undergo the first rf cooling stage – a 2.5 s long frequency ramp from 13.5 MHz to 2.3 MHz. Then, they are transferred into a dimple trap generated by the small wires, where a second rf cooling stage (a 1.4 s long frequency ramp from 2.1 MHz to ∼1.8 MHz) achieves Bose-Einstein condensation. After this, the BEC is loaded into the final trap, which is a dimple trap produced by the small wires, with frequencies $(\omega_x, \omega_y, \omega_z) = 2\pi \times (113, 301, 301)$ Hz [51], and centred 40 µm from the chip surface. There, the thermal fraction of the BEC is rendered negligible by a 0.2 s long rf signal with a frequency corresponding to less than the condensation temperature (typically ∼2.3 MHz). This process eliminates a fraction of condensed atoms (it "cuts into the BEC"), allowing us to set the final atom number by changing the frequency of the signal. This also has the effect of stabilising the atom number against fluctuations.

At this stage, a fully condensed BEC composed of typically ∼1500 atoms in the internal state $|F = 1, m_F = -1\rangle$ has been produced. This is the starting point of the so-called *science* part of the experimental sequence, during which the internal state of the atoms is manipulated by means of homogeneous (Rabi pulses, see Sec. 3.3.2) and inhomogeneous (state-dependent potentials, see Sec. 3.3.3) mw and rf signals. The magnetic field at the trap centre (mainly composed of the x bias field) is set to the magic field value of ≈3.23 G, so as to maximise the coherence time of the BEC (see Sec. 2.3.1). A few examples of a possible science part can be found in Chap. 4 and appendix C.

After the science part, the atoms are detected as described in Sec. 3.4.1. In order to measure any spin direction other than $\hat{S}_z$, a collective spin rotation has to be performed before detection, see Sec. 3.4.1.

Chapter 4

Einstein-Podolsky-Rosen experiment with two Bose-Einstein condensates

In 1935, Einstein, Podolsky, and Rosen (EPR) challenged quantum mechanics by showing the inconsistency between its completeness and the classical principle of local realism [1]. EPR's work was seminal both for the study of fundamental physics and for quantum technology, as it was the first to reveal some of what today are considered the most distinctive features of quantum theory. Among others, it led to the definition of entanglement and steering [2, 3] and, eventually, to Bell's proof that the predictions made by quantum mechanics cannot be reproduced by any local-hidden-variable theory [4]. Although the EPR paradox has been observed with few photons or atoms (both in its original form [6–10] and in the form of Bell tests [11–18]), how far quantum behaviour extends into the macroscopic world is an open question, which can be addressed by performing EPR experiments with increasingly macroscopic, massive systems [9, 20, 21].

In this chapter I briefly review the EPR paradox, introduce the criteria that allow us to investigate it experimentally, and present the main result of this thesis, namely an EPR experiment with two spatially separated and individually addressable BECs. Analogous to the original Gedankenexperiment, we first use interatomic interactions to generate many-particle entanglement in a single BEC, which we then split into two spatially separated condensates. As shown in Ref. [92], the many-particle entanglement present in the initial BEC results in bipartite entanglement between the split systems, which in our case is strong enough to show the EPR paradox.

With respect to previous work [30, 31, 93], the novelty here resides in the ability to coherently split a two-component BEC, while maintaining nearly

perfect overlap and coherence between the spin components of the two resulting condensates. This allows us to carry out high-fidelity coherent spin rotations on each condensate separately.

The results reported in this chapter were published in Ref. [36], which is partly reproduced here. For a more extensive review of the EPR paradox, I refer the reader to Ref. [9].

4.1 The Einstein-Podolsky-Rosen paradox

In their paper from 1935 [1], EPR posed the question whether the description of reality made by quantum mechanics can be considered complete, or whether there are some "hidden" degrees of freedom that predetermine the measurement outcomes, which the theory considers probabilistic. EPR conceived a Gedankenexperiment with which they showed that the completeness of quantum mechanics is inconsistent with the classical principle of local realism. The latter is the union of local causality, which forbids any causal connection between space-like separated events, and realism, which requires all physical properties of a system to have a definite value at all times and independent of observation. This principle is so deeply rooted in classical physics, that it was given by EPR as a requirement for a physical theory to be considered acceptable.

EPR's original Gedankenexperiment considers the translational degree of freedom of two particles. Here, I discuss its spin variant proposed by Bohm [32,33], which is conceptually closer to our experiment. Bohm's variant considers two spin-1/2 particles, A and B, prepared in a singlet state, which are separated by a process that conserves the total spin. Once they can no longer interact, the spin of one of them (say, A) is measured along some component. Since the total spin is zero, the same spin component of B is then necessarily opposite to that of A. This represents no conceptual difficulty in classical physics, where all spin components have a definite value at all times. In quantum mechanics, on the other hand, different spin components are non-commuting observables. When A is measured, both particles are collapsed onto a state in which the chosen spin component has a definite value, while the perpendicular ones are undetermined and, if measured, will show no correlation. Thus, although the two particles no longer interact, the choice of measurement performed on A determines which component of B has a definite value – an effect denominated *steering* by Schrödinger [2, 3].

If one assumed the validity of local realism, this instantaneous and remote influence of the measurement choice of A on the state of B could not exist, and the measurement of any other spin component of B would be per-

fectly legitimate and reveal a predetermined property of the system. Due to the measurement correlations predicted by quantum mechanics for such a state, however, the measurement result obtained from A would also reveal a pre-existing property of system B, allowing an experimenter to determine simultaneously two non-commuting spin components of B [2,3], which is inconsistent with the quantum state representation of the system. Therefore, accepting both local realism and the completeness of quantum mechanics leads to a contradiction, which became known as the EPR paradox.

Since they believed in the validity of local realism, EPR concluded quantum theory to be incomplete. However, the EPR paradox shows the inconsistency between the completeness of quantum theory and local realism, but it does not make a statement about which needs to be refused. In 1964, Bell conceived a scenario in which quantum mechanics and local realist theories make different predictions [4], which was further developed into experimentally useful criteria, such as the CHSH inequality [94]. All experiments conducted since have yielded results consistent with quantum mechanics [11–18].

In principle, any pure entangled state can be used to observe the EPR paradox and Bell nonlocality. However, only a strict subset of mixed entangled states, so-called *EPR entangled* states, show strong enough correlations to demonstrate the EPR paradox [95]. Similarly, only a strict subset of the latter are able to show Bell nonlocality [96]. These distinctions can be formalised in terms of the ability to perform different tasks [95], which hints at the fact that stronger correlations can be exploited as a resource for different applications in quantum technology. This is indeed the case: For example, EPR entanglement guarantees the efficacy of certain quantum information protocols, such as quantum teleportation, entanglement swapping, one-sided device independent quantum key distribution, or randomness certification [9, 97, 98].

As a final remark, it is worth noting that the remote measurement correlations resulting from quantum entanglement do not violate local causality in the strict special relativistic sense. Indeed, since the experimenter with access to system A cannot decide the measurement results, they cannot influence the measurement statistics of system B and thus they cannot transmit any information via the measurement process [99]. Although the non-local character of quantum measurements remains, a proper treatment of this requires a more rigorous definition of causation (see for example Ref. [100]), which is beyond the scope of this thesis.

4.2 The Einstein-Podolsky-Rosen paradox with many-particle systems

The EPR paradox was originally conceived and later observed for few particles [1, 5–8, 10–18, 32, 33]. However, the principle of local realism originates from classical physics and is satisfied by macroscopic phenomena. It is therefore interesting to investigate whether the EPR paradox can be demonstrated with macroscopic objects, where we are used to assuming the validity of local realism still nowadays [19]. To perform an EPR experiment with two large systems, these need to be entangled and no longer able to interact when the measurements are performed. In addition to this, the experimenter must be able to measure at least two non-commuting observables of at least one of them. In recent years, remarkable progress has been made in this direction, with the demonstration of entanglement between spatially separated macroscopic objects [22–27] and the observation of EPR entanglement within individual many-particle systems [28–31].

As opposed to the case of the Gedankenexperiment discussed in Sec. 4.1, perfect correlations do not exist in any realistic scenario. In addition to this, imperfectly correlated states are commonly used in many-particle systems, where maximally entangled states are often experimentally inaccessible or very fragile, see Sec. 2.3.5. In order to discern the EPR paradox in this case, one needs quantitative criteria; in the following I introduce the ones that are used in this thesis. Let us consider two spin systems $\hat{\vec{S}}^A$ and $\hat{\vec{S}}^B$. Both systems satisfy Heisenberg relations, such as

$$\mathcal{E}^B_{\mathrm{Hei}} \coloneqq \frac{4\ \mathrm{Var}\left(\hat{S}^B_z\right)\mathrm{Var}\left(\hat{S}^B_y\right)}{\left|\left\langle \hat{S}^B_x \right\rangle\right|^2} \geq 1. \tag{4.1}$$

Inequalities like Eq. (4.1) are to be understood as applied to repeated measurements of identically prepared quantum states, as every experimental repetition can only yield one valid measurement outcome [101]. If the two spins are entangled, their measurement outcomes will be correlated, allowing us to use the results obtained on, say, $\hat{\vec{S}}^A$ to infer those on $\hat{\vec{S}}^B$. In our case, this is achieved by the linear estimates $\hat{S}^{B,\mathrm{inf}}_{z,y} \coloneqq -g^{A\to B}_{z,y}\hat{S}^A_{z,y} + c^{A\to B}_{z,y}$, where $g^{A\to B}_{z,y}$ and $c^{A\to B}_{z,y}$ are real numbers that can be chosen. The accuracy of the inference is quantified by the so-called *inference variances*, $\mathrm{Var}_{\mathrm{inf}}(\hat{S}^B_{z,y}) \coloneqq \mathrm{Var}(\hat{S}^B_{z,y} - \hat{S}^{B,\mathrm{inf}}_{z,y})$. If we assumed a local realist description of the total system, it should be possible to assign to any measurement outcome of $\hat{\vec{S}}^A$ a local quantum state of system B [95]. Due to this, the

inference variances should obey the same uncertainty relations as the normal observables of $\hat{\vec{S}}^B$ [9, 102]. Therefore, the EPR paradox is demonstrated if an inequality of the form

$$\mathcal{E}_{\mathrm{EPR}}^{A\to B} \coloneqq \frac{4\ \mathrm{Var}_{\mathrm{inf}}\left(\hat{S}_z^B\right)\mathrm{Var}_{\mathrm{inf}}\left(\hat{S}_y^B\right)}{\left|\left\langle \hat{S}_x^B \right\rangle\right|^2} \geq 1 \tag{4.2}$$

is violated [9, 102]. In other words, the EPR paradox is shown if the information gained from the remote system $\hat{\vec{S}}^A$ allows an experimenter to make better predictions about $\hat{\vec{S}}^B$ than what is possible by having access to $\hat{\vec{S}}^B$ alone, which in a local realist world would not respect Heisenberg's uncertainty principle. The parameters $g_{z,y}^{A\to B}$ (called *gain factors*) can be determined experimentally by minimising the inference variances, whereas $c_{z,y}^{A\to B}$ constitute an additive constant in the variances and can be dropped. A similar criterion can be derived for the scenario where the measurement outcomes on $\hat{\vec{S}}^B$ are used to infer those on $\hat{\vec{S}}^A$, $\mathcal{E}_{\mathrm{EPR}}^{B\to A} \geq 1$. Note that, since the EPR paradox originates from an asymmetric scenario and is an asymmetric concept, a violation of $\mathcal{E}_{\mathrm{EPR}}^{B\to A} \geq 1$ does not imply a violation of $\mathcal{E}_{\mathrm{EPR}}^{A\to B} \geq 1$, and vice versa.

A criterion for entanglement (non-separability) similar to Eq. (4.2) was derived in Ref. [103]: Two spins $\hat{\vec{S}}^A$ and $\hat{\vec{S}}^B$ are in an entangled state if the inequality

$$\mathcal{E}_{\mathrm{ent}} \coloneqq \frac{4\ \mathrm{Var}\left(g_z^{A\to B}\hat{S}_z^A + \hat{S}_z^B\right)\mathrm{Var}\left(g_y^{A\to B}\hat{S}_y^A + \hat{S}_y^B\right)}{\left(\left|g_z^{A\to B}g_y^{A\to B}\right|\left|\left\langle \hat{S}_x^A \right\rangle\right| + \left|\left\langle \hat{S}_x^B \right\rangle\right|\right)^2} \geq 1 \tag{4.3}$$

is violated. The values of $g_{z,y}^{A\to B}$ that minimise $\mathcal{E}_{\mathrm{ent}}$ are in general not the same as the optimal ones for $\mathcal{E}_{\mathrm{EPR}}^{A\to B}$. It is worth noting that $\mathcal{E}_{\mathrm{ent}}$ can be rewritten with $\hat{\vec{S}}_B$ as inferring system without changing its value, with $g_{z,y}^{B\to A} = 1/g_{z,y}^{A\to B}$, which is consistent with entanglement being a symmetric concept.

Although similar, there is an important difference between the EPR and entanglement criterion: Eq. (4.2) applies to inference variances in general, whereas Eq. (4.3) was derived specifically for linear combinations of observables. Thus, any information obtained about the inferring system and any classical information can be used to violate Eq. (4.2), but not Eq. (4.3). It is also worth noting that, as long as the same inference variances are used, $\mathcal{E}_{\mathrm{EPR}}^{A\to B}$ is always larger than or equal to $\mathcal{E}_{\mathrm{ent}}$, reflecting the fact that an observation

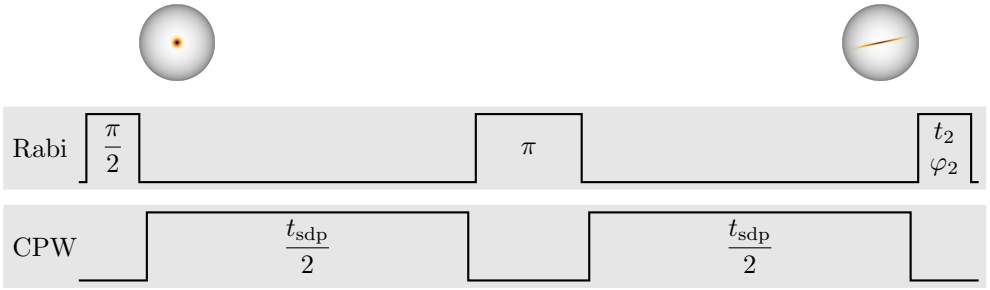

Figure 4.1: Schematic of the spin squeezing sequence with spin echo. Top: Qualitative representation on a Bloch sphere of the state of the BEC at different stages. Bottom: Time schematic of the Rabi coupling and of the CPW mw. The BEC is initially prepared in a CSS on the equator of the Bloch sphere (see the Bloch sphere on the top left) by a $\pi/2$ pulse. Then, the CPW mw is turned on for a total time t_{sdp}, inducing the OAT dynamics and producing a SSS (see the Bloch sphere on the top right). At half of t_{sdp}, the CPW mw is switched off and the echo π pulse is performed. Finally, a further Rabi pulse can be applied, e.g. to align the squeezed direction with the $\hat{S}_z$ axis.

of the EPR paradox requires stronger correlations than a demonstration of entanglement [95].

In this work we do not address Bell nonlocality. The reason for this is that all currently known criteria for Bell nonlocality with two many-particle systems require non-Gaussian measurements or state preparation, e.g. single-atom resolving detection [104]. Bell-type correlations among the atoms in a single BEC have been shown indirectly by evaluating a witness that only necessitates collective measurements [29].

4.3 Generation of entanglement in a Bose-Einstein condensate

The first step of an EPR experiment is the preparation of an entangled state. As explained in Secs. 2.3.5 and 3.3.3, in our experiment we generate many-particle entanglement in the form of spin squeezing [34,35,60]. We do this by activating the one-axis-twisting term $\hbar\chi\hat{S}_z^2$ in the collective-spin Hamiltonian (Eq. (2.17)) for a duration t_{sdp} by means of a state-dependent mw dressing potential, see Fig. 4.1. To reduce shot-to-shot phase fluctuations, we perform a spin echo pulse [105] during the spin squeezing sequence: At half t_{sdp}, the state-dependent potential is switched off and a Rabi π pulse (the *echo pulse*)

is applied.

We choose t_{sdp} to correspond to the second revival of the demixing-remixing dynamics (see Sec. 3.3.3), which corresponds to ≈40 ms. In this way, the echo pulse takes place at the first revival and is able to perform a collective spin rotation, which would be impossible if the two BEC components were not overlapped. The calibration measurement used to determine the precise value of t_{sdp} is described in appendix C.6.1.

After t_{sdp}, a Rabi pulse rotates the collective spin around its mean direction, so as to align the squeezed direction along $\hat{S}_z$. The angle by which it needs to be rotated (*squeezing angle*) is determined experimentally by observing for which angle the spin noise is minimised, see appendix C.7. In the measurements presented in this thesis, the squeezing angle was found to be 10°, i.e. the duration of the last pulse was $t_2 = (10/90)\, t_{\pi/2}$. We typically measure a number squeezing of $\zeta^2 \simeq -7$ dB, anti-squeezing of ≃14 dB, and interferometric contrast of 96 %, see Fig. C.6. We attribute the excess noise w.r.t the Heisenberg limit to technical noise, see Refs. [51, 86] for a more detailed analysis. The reduction of the measured contrast w.r.t. the 97 % visibility reported in Sec. 2.3.7 is compatible with the effect of the state wrapping around the Bloch sphere for our squeezing parameters, which is expected to be a factor of ≈0.99 [51, 64].

When analysing the experimental data, we include in the expression for projection noise the factor $1 - \langle N_{\mathrm{rel}} \rangle^2$, which takes into account the possibility that the state is not perfectly on the equator of the many-particle Bloch sphere ($\langle \hat{S}_z \rangle \neq 0$). We also typically express for convenience the number squeezing parameter in terms of the relative number imbalance, N_{rel}, obtaining

$$\zeta^2 = \frac{\mathrm{Var(N_{rel})\langle N \rangle}}{1 - \langle N_{\mathrm{rel}} \rangle^2}. \tag{4.4}$$

The squeezing values presented here were obtained without any clock shift correction (see Ref. [51]) and technical noise subtraction.

4.4 Coherently splitting a two-component Bose-Einstein condensate

After generating entanglement in the initial BEC, we need to coherently split it into two spatially separated two-component condensates, which we are able to measure in all the spin directions necessary to evaluate the criteria Eq. (4.2) and (4.3). Our splitting technique consists of two parts, namely a beam splitter in spin space and a Stern-Gerlach-like spatial separation.

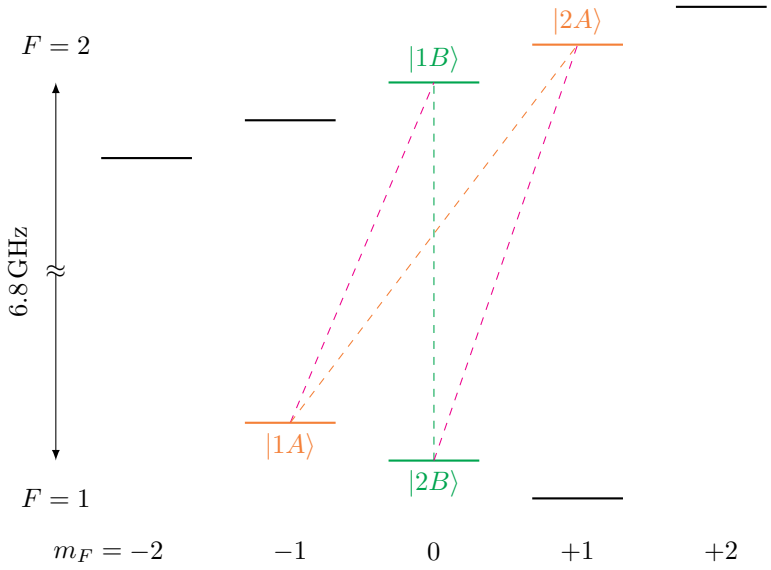

Figure 4.2: Level diagram of the hyperfine split ground state of ^{87}Rb in the linear Zeeman regime. The states are indicated by solid horizontal lines. Dashed lines indicate the transitions involved in the splitting process and individual manipulations (note that the one relative to condensate A is the two-photon transition discussed in Sec. 3.3.2). Orange and green colour refer to condensate A and B, respectively, whereas magenta represents the splitting transitions.

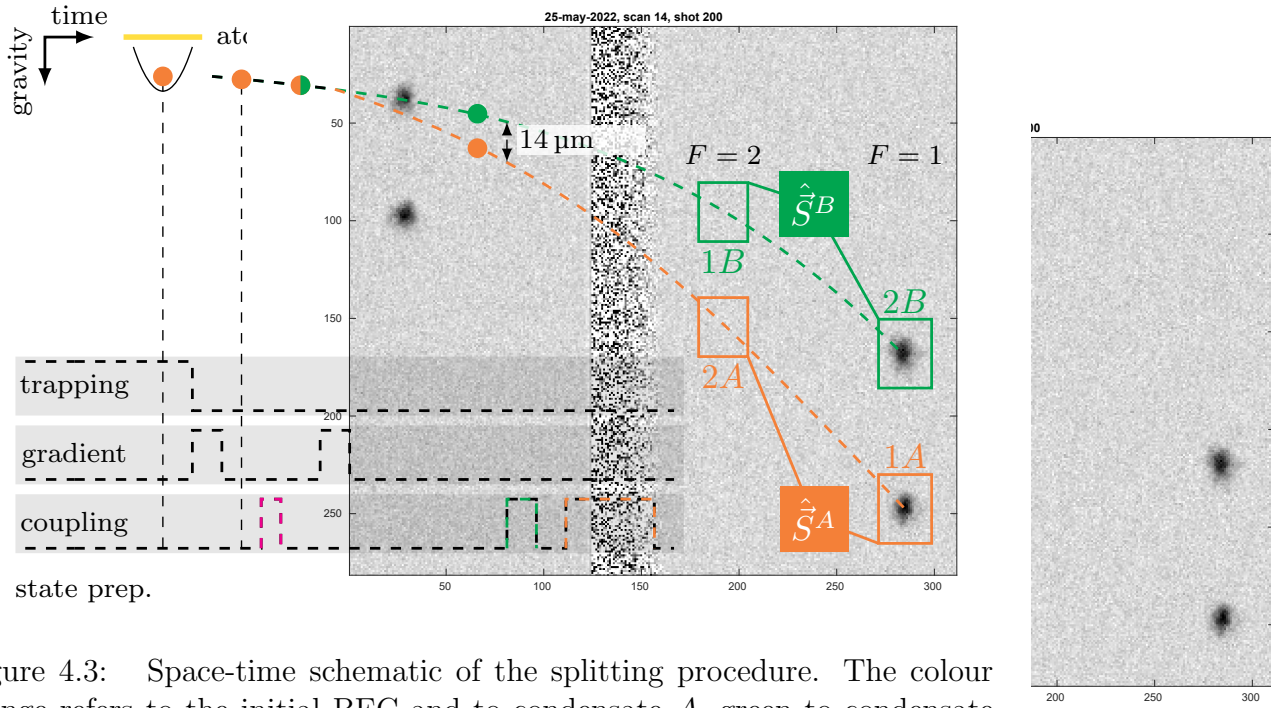

Figure 4.3: Space-time schematic of the splitting procedure. The colour orange refers to the initial BEC and to condensate A, green to condensate B, and magenta represents the splitting pulse. Bottom left: main control parameters for splitting and state manipulation, where *trapping* indicates the magnetic trap (see Secs. 3.1.1 and 3.6), *gradient* the magnetic field gradient used to accelerate the BEC before the time of flight (see Sec. 3.4.1), and *coupling* the coherent drive of the transitions indicated by the colour coding. The timing is aligned with the sketch above, but not to scale. On the right, typical absorption images are shown, from which the atom numbers in all four states are determined. This corresponds to a measurement of the selected components of the collective spins $\hat{\vec{S}}^A$ and $\hat{\vec{S}}^B$.

The first is implemented by coherently driving the transitions between both BEC components and two states with zero magnetic moment, see Fig. 4.2. The spatial separation is obtained by exploiting the difference in magnetic moment between the two pairs of states: A magnetic field gradient selectively accelerates the states with non-zero magnetic moment. This results in two pairs of overlapped states moving away from each other, which can thus be described as two collective spins. Since the two pairs of states are connected by different transitions, we can perform individual rotations of their collective spins, which allows us to measure any of their spin components independently.

It is worth noting that, after the splitting, all atoms are in a coherent superposition of all four involved states, making it impossible to describe the two condensates as systems with fixed atom number. It is therefore incorrect to define their collective spins with Eq. (2.14). Rather, one has to use Schwinger's bosonic-operator-based representation of angular momentum, see Eq. (2.16).

I will now give a more detailed description of the splitting experimental sequence. Although it would be possible to drive the splitting transitions when the BEC is trapped, we decided to first release it from the trap for two reasons. Firstly, these transitions connect states with different magnetic moments and are thus strongly affected by magnetic-field changes ($\approx 0.7\,\mathrm{MHz/G}$). The field gradient due to the magnetic trap[1] is sufficient to induce a measurable space-dependent phase shift across the BEC during the splitting pulses. Secondly, to reduce the imaging noise it is important for us to shorten the expansion time before detection, which we usually do by accelerating the BEC with a magnetic-field gradient (see Sec. 3.4.1). Since the states defining one of the split condensates have zero magnetic moment, we can only influence their expansion time by accelerating the initial BEC.

The splitting procedure (sketched in Fig. 4.3) begins by releasing the BEC from the trap and accelerating it with a magnetic field gradient, which reduces the expansion time before detection. Then, we apply the beam splitter in spin space by simultaneously driving the transitions

$$|1A\rangle \coloneqq |F=1, m_F=-1\rangle \longleftrightarrow |1B\rangle \coloneqq |F=2, m_F=0\rangle\,,$$
$$|2A\rangle \coloneqq |F=2, m_F=+1\rangle \longleftrightarrow |2B\rangle \coloneqq |F=1, m_F=0\rangle\,,$$

(magenta in Figs. 4.2 and 4.3) with a two-tone mw pulse (see Sec. 3.3.2). We choose to apply a 50:50 beam splitter, which corresponds to a pulse duration of $t_{\pi/2}^{\mathrm{split}} \approx 70\,\mu\mathrm{s}$ for both transitions. A subsequent pulse of the magnetic field

[1] This is increased by the fact that the position of the trapped BEC is shifted by gravity w.r.t. the field minimum by a few micrometers.

gradient selectively accelerates the states $|1A\rangle$ and $|2A\rangle$, spatially separating the system into two distinct two-component BECs, which we call system A (composed of states $|1A\rangle$ and $|2A\rangle$, orange in Fig. 4.2) and system B (composed of states $|1B\rangle$ and $|2B\rangle$, green in Fig. 4.2).

Since $|1A\rangle$ ($|1B\rangle$) and $|2A\rangle$ ($|2B\rangle$) have the same magnetic moment, the overlap between the states in each system is preserved by the splitting mechanism, allowing us to describe them as two collective spins, $\hat{\vec{S}}^A$ and $\hat{\vec{S}}^B$. Once the two condensates are split, we can coherently drive the transitions $|1A\rangle \leftrightarrow |2A\rangle$ and $|1B\rangle \leftrightarrow |2B\rangle$ with distinct radio-frequency and microwave signals, which allows us to perform arbitrary spin rotations on $\hat{\vec{S}}^A$ and $\hat{\vec{S}}^B$ independently, see Sec. 4.4.2.

We detect the split BECs in the same way as described in Sec. 3.4. We acquire two absorption images: The first one detects atoms in states with $F = 2$ ($|2A\rangle$ and $|1B\rangle$) and the second one detects those with $F = 1$ ($|1A\rangle$ and $|2B\rangle$) – after they have been optically pumped to $F = 2$. Due to the large separation between the two BECs ($\approx$80 µm at the time of the first image and $\approx$100 µm at the time of the second), we can count the atoms present in all four states separately and thus obtain a measurement of the spin components $\hat{S}_z^A = (\hat{N}_1^A - \hat{N}_2^A)/2$ and $\hat{S}_z^B = (\hat{N}_1^B - \hat{N}_2^B)/2$ (see Fig. 4.3). Other spin components can be measured by coherently rotating the collective spins before detection (see Secs. 3.4.1 and 4.4.2).

4.4.1 Cloud separation

Performing an EPR experiment requires selecting the measurement basis when the two systems are no longer able to interact. It is therefore important for us to estimate the separation between the two BECs at the beginning of the individual collective spin rotations, t_{rot}.

Although it is possible for us to acquire images of the BECs at t_{rot}, see Fig. 4.4, it is difficult to determine the cloud size and distance at this time from these images. Indeed, the cloud size at t_{rot} is comparable to the optical resolution of the imaging apparatus, whose point-spread function has an estimated rms value of 1.5 µm (see the supplementary material of Ref. [30]). Furthermore, at this time the atoms are located close to the upper edge of our field of view, where there are visible aberrations. Due to these fringes, from Fig. 4.4 the distance between the two BECs can only be estimated roughly by counting the pixels between the apparent cloud centres – which yields a value of 14.4(13) µm. We therefore estimate the BEC distance and size at t_{rot} based on images acquired at later times.

To determine the distance between A and B at t_{rot}, we perform an ex-

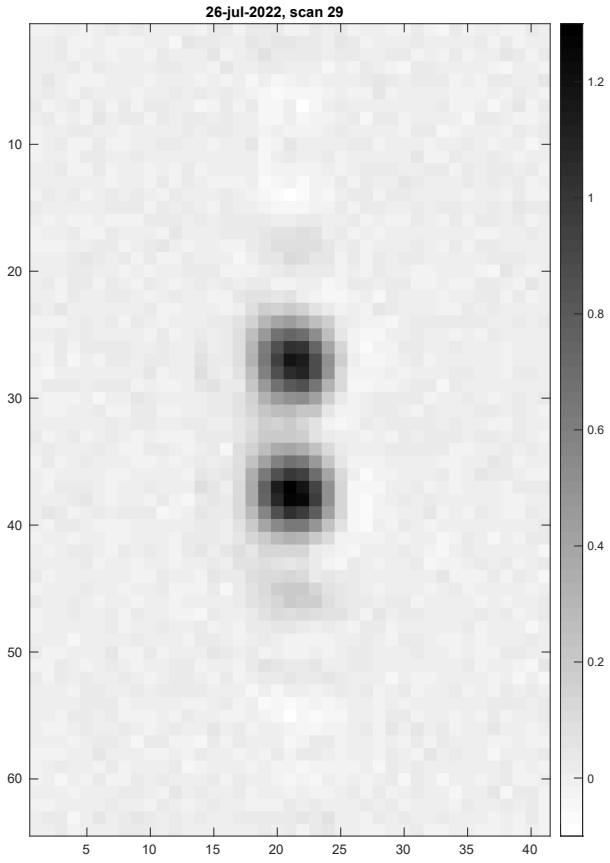

Figure 4.4: Image of the two condensates at the beginning of the individual rotations (averaged over ~ 30 repetitions). The scale indicates distances in units of pixels – each pixel corresponds to 1.3 µm at the position of the atoms. The imaging pulses were kept as short as possible (10 µs) to minimise blurring from the displacement and diffusion of the atoms. Due to aberrations and to the optical resolution of the imaging apparatus, it is difficult to use these images to determine the size and separation of the split condensates.

periment where we vary the time of flight (TOF, see Sec. 3.4.1) – a so-called *free fall experiment*. To reduce the blurring due to the displacement and diffusion of the atoms during the imaging pulses, these were kept as short as possible[2], 20 µs. For every value of the TOF, we fit the atom density profiles (averaged over ∼25 repetitions) with a two-dimensional Gaussian profile to obtain the BEC position. This position as a function of time is fitted with a free fall trajectory model, which yields a distance of 15.2(35) µm at the time t_{rot} (which is compatible with the image shown in Fig. 4.4).

The cloud size at t_{rot} was estimated with two methods, one based on simulations and the other on the free fall experiment described above. Before discussing them, it is worth spending a few words about the definition of the cloud size. As mentioned in Sec. 2.2, our BEC is in an intermediate regime between the non-interacting case and the Thomas-Fermi limit. We define the cloud size as the distance from the centre containing 99.9 % of the atoms – which in our case means that for both system A and B on average less than one atom should be found out of this radius. To be able to extract this quantity from measured atom density profiles, we simulate the BEC density profile in the trap (by solving the TIGPE with a program written by Roman Schmied), fit it with a two-dimensional Gaussian profile, and calculate the ratio between the cloud size as we defined it and the Gaussian radius (we obtain a factor of 2.9 for the vertical direction). Due to the self-similar expansion of BECs [106], this ratio remains constant throughout the TOF.

We place an upper bound to the cloud size by means of a numerical estimate: Using the simulated density profile mentioned above as a starting point, we numerically solve the differential equation for the BEC expansion from Ref. [107], obtaining a vertical cloud size of 6.0 µm at the time t_{rot}. Since this differential equation was derived for the Thomas-Fermi limit, where interatomic interactions are stronger than in our case, this is not an accurate estimate of the cloud size, but rather an upper bound. Note that, even if this were the real value, the clouds would be completely separated.

From the cloud expansion simulation we see that, at the time t_{rot}, the expansion is already in the ballistic regime. We can thus estimate the vertical cloud size at that time by performing a linear fit of the results from the free fall experiment mentioned above, obtaining 4.1(4) µm. Therefore, we conclude that the two BECs are fully separated already at the time t_{rot}.

While the estimated distance does not ensure space-like separation between the measurements of the two BECs, there are no known interactions between the two condensates that could couple their collective spins across

[2]Because of the more dilute clouds detected in the free-fall experiment, the imaging pulses here are not as short as in the image shown in Fig. 4.4.

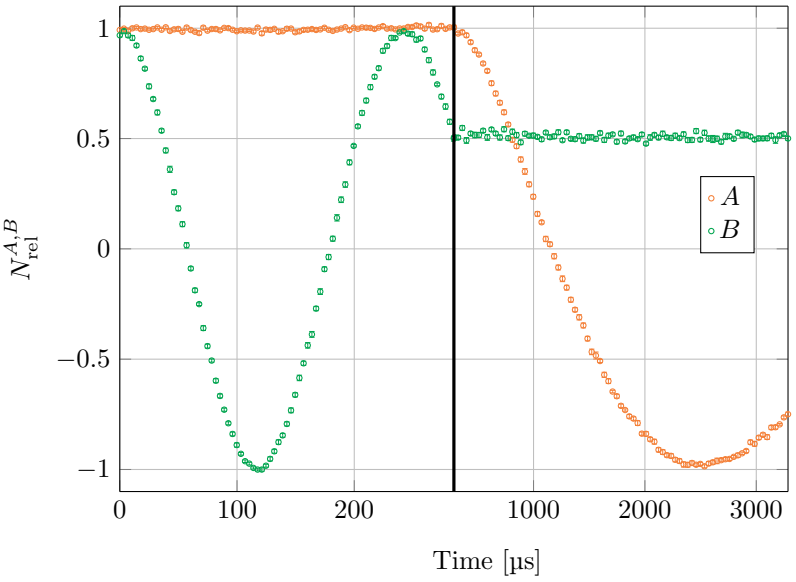

Figure 4.5: Individual Rabi oscillations of $\hat{\vec{S}}^A$ and $\hat{\vec{S}}^B$. The experimental sequence begins by splitting the BEC initialised in state $|F = 1, m_F = -1\rangle^{\otimes N}$ (see Sec. 3.6) 50:50 into system A and B. Once the two condensates are fully separated, we first drive Rabi oscillations on system B alone, then on system A. The data are obtained by interrupting this procedure at different times (shown on the horizontal axis) and detecting. The plot shows the normalised spin components $N_{\mathrm{rel}}^{A,B} = (N_1^{A,B} - N_2^{A,B})/(N_1^{A,B} + N_2^{A,B})$. The thick vertical line denotes a change in time scale.

this distance on the timescale of the experiment: First of all, the fact that the two BECs are fully separated at t_{rot} rules out any influence of collisional interactions. Secondly, the effect of magnetic dipole-dipole coupling, which is the dominant type of long-range interaction in our system, is rendered completely negligible by the fact that in each system the two BEC components have nearly identical magnetic moments and thus the related interaction energy has a very weak dependence on the state of the collective spins.

4.4.2 Individual manipulation of the split condensates

Since system A is composed of the same states discussed in Chaps. 2 and 3, we can perform collective spin rotations of $\hat{\vec{S}}^A$ in the same way as described in Sec. 3.3.2. The states that constitute system B, on the other hand, are connected by a single-photon mw transition, which can be addressed by means of mw pulses (see Fig. 4.2). Individual Rabi oscillations of the two collective

spins are shown in Fig. 4.5, from which it can be seen that the Rabi frequency attainable for system B is over 10 times larger than for system A.

Given that both systems are characterised by transitions whose frequencies only depend weakly on the magnetic field, both are robust to dephasing from magnetic field fluctuations [37]. In particular, the derivative of the transition frequency of system A w.r.t. the magnetic field is zero at $B_0 \approx 3.23\,\mathrm{G}$ (see Sec. 2.3.1), whereas for system B this occurs at $0\,\mathrm{G}$ [52]. Due to this, the coherence times of the two systems are maximised at different fields. Because of the much larger Rabi frequency attainable for system B, we chose to maintain the magnetic field during the individual manipulations of the BECs at B_0 (where $\mathrm{d}\omega_B/\mathrm{d}B \simeq 2\pi\, 3.7\,\mathrm{kHz/G}$) and to perform the rotation of $\hat{\vec{S}}^B$ first.

Although the mw, rf, and bias fields are homogeneous across the BEC size (see Secs. 3.1 and 3.3.2), this is not the case over much larger distances and during the TOF the condensates experience varying fields. The static magnetic field, which can be determined by observing the change in resonance frequency of a transition with large differential Zeeman shift, changes only slightly and can be kept close enough to B_0 by adjusting the current in the x bias coil, such that the shift it induces in $\hat{\vec{S}}^A$ and $\hat{\vec{S}}^B$ can be neglected.

On the other hand, we observe that the Rabi frequencies relative to both systems decrease relevantly during the TOF. The change in microwave level shifts caused by this is estimated to be on the order of a few tens of Hz, most of which can be corrected for by calibrating the frequency of the driving signals. We do, however, notice that we cannot obtain a better contrast than 98 % in the Rabi oscillations of system A, which can be due to the mw and rf amplitude variations during the Rabi pulse itself, see Fig. 4.5. Since for the results presented in this thesis we never need to perform more than a $\pi/2$ pulse on system A, this effect is not a limitation. In addition to influencing the light shifts, the time-varying Rabi frequencies require adjusting the pulse times individually for different pulse areas, see appendix C.8.

Performing the individual manipulations during the TOF also introduces time (thus pulse area) constraints on the feasible rotations: With the current experimental parameters we can perform up to a 2π pulse on system B and up to a π pulse on system A, see Fig. 4.5, which allow us to perform arbitrary collective spin rotations on both systems. Increasing the duration of the TOF would be possible, but at the expense of more dilute clouds at the time of the imaging, which would result in larger imaging noise (see Sec. 3.4.4).

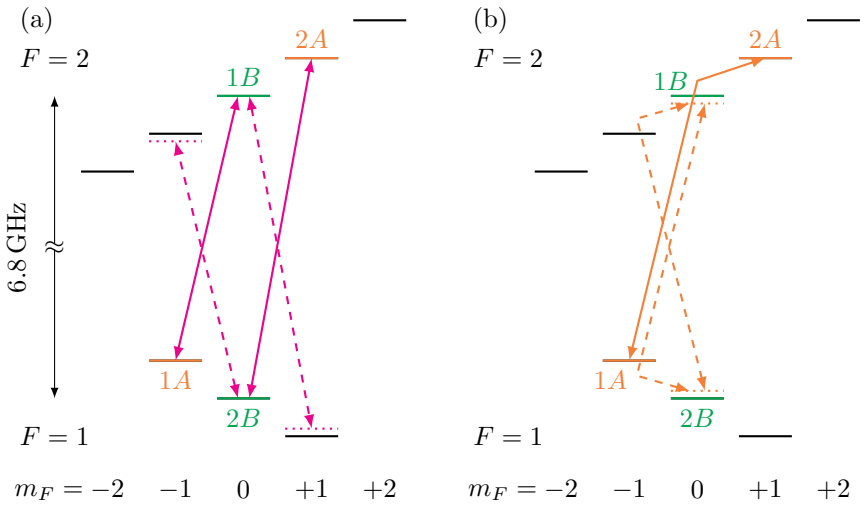

Figure 4.6: Level structure of the ^{87}Rb hyperfine split ground state in the linear Zeeman regime (not to scale). Orange indicates system A, green system B, and magenta the splitting transitions. The desired transitions are indicated by solid lines, the undesired close-to-resonance transitions are represented by dashed lines. (a) Transitions involved in the splitting of the condensate into systems A and B. (b) Transitions involved in driving spin rotations of $\hat{\vec{S}}^A$ after splitting.

4.4.3 Addressability and strength of the transitions

Several transitions in the ^{87}Rb hyperfine split ground state are nearly degenerate and differ only by quadratic Zeeman shifts, which are of the same order of magnitude as the Rabi frequencies (1-10 kHz). In the experimental sequence up until the splitting, the populated states and applied driving frequencies are such that they do not lead to any undesired couplings. However, the driving fields used for the splitting pulse and for the subsequent rotations of $\hat{\vec{S}}^A$ are close to resonance with other relevant transitions, see Fig. 4.6. It is thus essential to carefully choose the parameters of these pulses, so as to prevent the spurious driving of undesired transitions.

It is in principle possible to suppress the undesired transitions by only using driving fields with the correct circular polarisation. However, since the BECs are close to the metallic atom chip surface, this is challenging to attain in our experiment and we observe that the driving fields contain all polarisation components (see Sec. 3.3.2). We therefore have to ensure the selectivity by carefully choosing the frequency and strength of the driving fields.

In the case of the splitting pulse (see Fig. 4.6(a)), the desired transition $|1A\rangle \leftrightarrow |1B\rangle$ is close to resonance with $|2B\rangle \leftrightarrow |F = 2, m_F = -1\rangle$ and the desired $|2A\rangle \leftrightarrow |2B\rangle$ with $|1B\rangle \leftrightarrow |F = 1, m_F = 1\rangle$ (both with 9 kHz detuning). These additional close-to-resonant transitions can cause atoms to be transferred from system B to states with different magnetic moments, where they are lost during the application of the magnetic gradient pulse. This loss mechanism is mitigated by the fact that states $|1B\rangle$ and $|2B\rangle$ are initially unpopulated and become populated only during the splitting pulse. Since in the case of the splitting we only need to perform a $\pi/2$ pulse, we choose for this pulse a combination of detuning and small enough Rabi frequency, for which we observe no losses to the undesired states, corresponding to a detuning of 2.2 kHz (adding to the 9 kHz mentioned above) and a pulse duration $t_{\pi/2}^{\text{split}} \approx 70\,\mu\text{s}$.

The fields used to rotate $\hat{\vec{S}}^A$ after the splitting (see Fig. 4.6(b)) are close to resonance with the transition $|1B\rangle \leftrightarrow |2B\rangle$, driven as a two-photon transition with intermediate states $|F = 2, m_F = -1\rangle$ and $|F = 1, m_F = -1\rangle$ (with 10 kHz detuning). However, since two-photon transitions have weak effective Rabi frequencies, this two-photon detuning can be exploited to ensure good selectivity of the pulse. The desired transition $|1A\rangle \leftrightarrow |2A\rangle$ is driven on two-photon resonance with $\pi/2$ time of $t_{\pi/2}^A \approx 850\,\mu\text{s}$, ensuring that the two-photon detuning of the undesired transitions is sufficient to render spurious rotations of $\hat{\vec{S}}^B$ negligible, see Fig. 4.5.

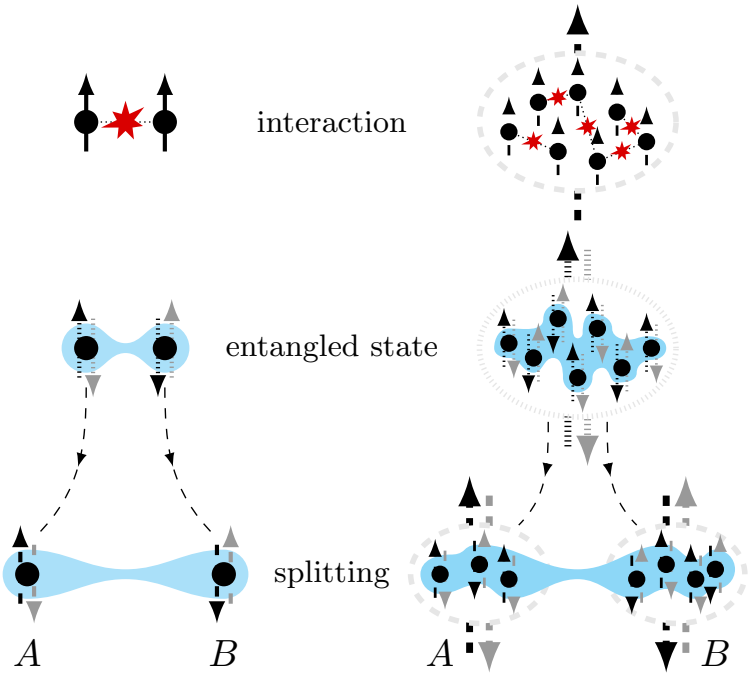

Figure 4.7: Schematic of an EPR experiment with two particles (left) and with two many-particle systems (right), where the spin degree of freedom is considered [32, 33]. In both cases, the particles are entangled by interactions and subsequently split into two different locations. In the case of the many-particle system, the interactions produce multipartite entanglement, which is inherited by the split systems in form of bipartite entanglement between their collective spins [92].

4.5 Einstein-Podolsky-Rosen experiment with two Bose-Einstein condensates

I will now describe how we use the tools discussed in Secs. 4.3 and 4.4 to observe the EPR paradox with two spatially separated, massive many-particle systems [36]. Following closely Bohm's version of the Gedankenexperiment [32, 33] (see Fig. 4.7), we first use interactions to generate entanglement in a BEC. Then, we physically split the entangled system into two distinct condensates, which can be individually manipulated and detected. The two BECs inherit entanglement from the initial state, resulting in correlated measurement outcomes of their collective spins [92].

In detail, the experimental sequence (see Fig. 4.8) begins by preparing the BEC (initialised in $|F = 1, m_F = -1\rangle^{\otimes N}$, see Sec. 3.6) in a coherent spin

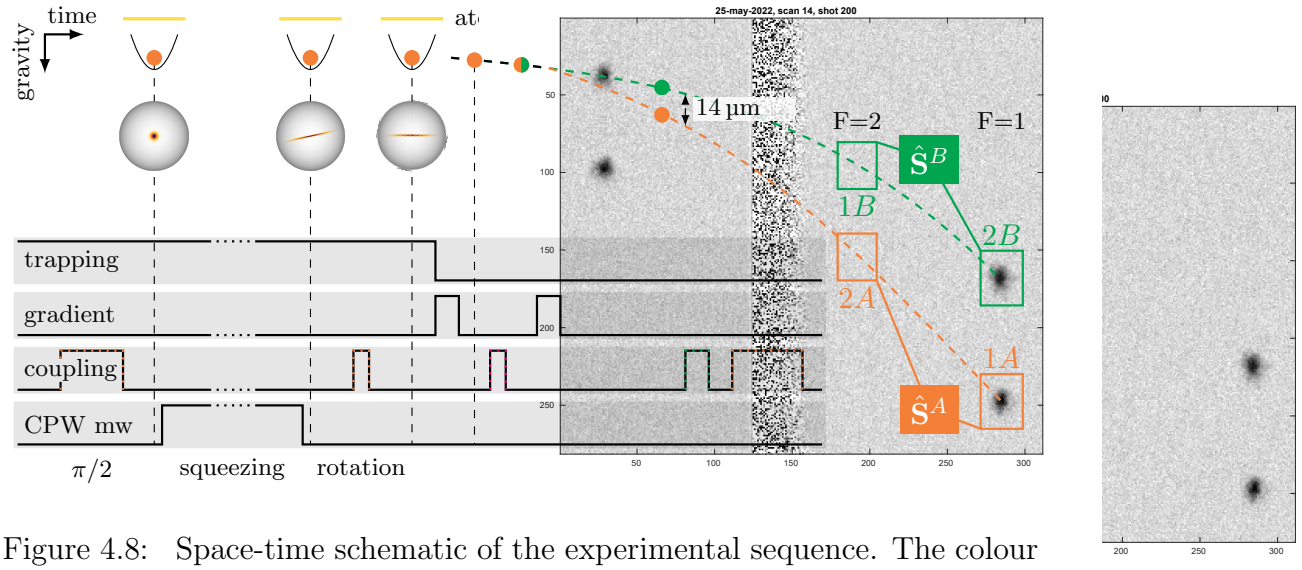

Figure 4.8: Space-time schematic of the experimental sequence. The colour orange refers to the initial BEC and to condensate A, green to condensate B, and magenta represents the splitting pulse. Bottom: main control parameters for splitting and state manipulation, where *trapping* indicates the magnetic trap (see Secs. 3.1.1 and 3.6), *gradient* the magnetic field gradient used to accelerate the BEC before the time of flight (see Sec. 3.4.1), *coupling* the coherent drive of the transitions indicated by the colour coding, and *CPW mw* the application of the state-dependent potential (see Secs. 3.3.3 and 4.3). The timing is aligned with the sketch above, but not to scale. The dotted segment indicates that the squeezing sequence is much longer than all other experimental parts (the echo pulse is not shown due to space constraints). The Bloch spheres give a qualitative representation of the state of the system at different stages. On the right, typical absorption images are shown, from which the atom numbers in all four states are determined. This corresponds to a measurement of the selected components of the collective spins $\hat{\vec{S}}^A$ and $\hat{\vec{S}}^B$.

state on the equator of the Bloch sphere, $|\mathrm{CSS} : \pi/2, 0\rangle$, with a $\pi/2$ pulse, see Secs. 2.3.4 and 3.3.2. Then, we turn on the mw state-dependent dressing potential for a total time of $t_{\mathrm{sdp}} \approx 40\,\mathrm{ms}$, applying an echo π pulse at half of that time (which is not shown in Fig. 4.8, due to space limitations). After rotating the state by 10° around its mean spin direction, we obtain a squeezed spin state polarised along the $\hat{S}_x$ component with a number squeezing of $-7\,\mathrm{dB}$ in the $\hat{S}_z$ direction, see Sec. 4.3. We then release the BEC from the magnetic trap and split it as described in Sec. 4.4. Once the split condensates are fully separated, we select their measurement bases by individually rotating their collective spins, see Secs. 3.4.1, 4.4.1, and 4.4.2. Owing to the large spatial separation of the two systems, we can measure the selected collective spin components of both with absorption imaging, see Secs. 3.4.1 and 4.4.

As discussed in Sec. 4.2, to demonstrate the presence of entanglement and the EPR paradox, one needs to evaluate the criteria Eqs. (4.3) and (4.2), respectively. This requires repeating the experiment with identical state preparation a sufficient number of times to get small enough error bars on the criteria, each time measuring either the x, y, or z component of both collective spins. Since $\hat{S}_x^{A,B}$ are measured to determine their mean values, whereas $\hat{S}_y^{A,B}$ and $\hat{S}_z^{A,B}$ are detected to evaluate the inference variances, we gather about five times more measurements of the y and z components than of $\hat{S}_x^{A,B}$.

The outcome of every measurement of $(\hat{S}_{z,y}^A, \hat{S}_{z,y}^B)$ (≈ 1600 repetitions in each basis) is represented by a point[3] in the correlation plots shown in Fig. 4.9. The strong correlations between the two systems can be explained as follows: Since A and B result from splitting a squeezed spin state with a beam-splitter-like process, combining the measurement results from the two systems recovers the modified fluctuations of the original state (up to experimental imperfections), i.e. $\mathrm{Var}(\hat{S}_{z,y}^A + \hat{S}_{z,y}^B) \simeq \mathrm{Var}(\hat{S}_{z,y}^{\mathrm{initial}})$. Considered individually, on the other hand, each system shows reduced squeezing and anti-squeezing, as this corresponds to tracing out the other one. Thus, the variance of the combined measurement results in the squeezed (anti-squeezed) spin component is smaller (larger) than the sum of the variances evaluated on the individual systems,

$$\mathrm{Var}(\hat{S}_z^A + \hat{S}_z^B) < \mathrm{Var}(\hat{S}_z^A) + \mathrm{Var}(\hat{S}_z^B), \tag{4.5}$$

$$\mathrm{Var}(\hat{S}_y^A + \hat{S}_y^B) > \mathrm{Var}(\hat{S}_y^A) + \mathrm{Var}(\hat{S}_y^B). \tag{4.6}$$

Because of this and of the fact, that

$$\mathrm{Var}(\hat{S}_{z,y}^A + \hat{S}_{z,y}^B) = \mathrm{Var}(\hat{S}_{z,y}^A) + \mathrm{Var}(\hat{S}_{z,y}^B) + 2\,\mathrm{Cov}(\hat{S}_{z,y}^A, \hat{S}_{z,y}^B), \tag{4.7}$$

[3]The measured values of S_y^B shown in Fig. 4.9 include the correction of phase shifts induced by measured triggering delay fluctuations in the signal generation, see Sec. 4.5.2.

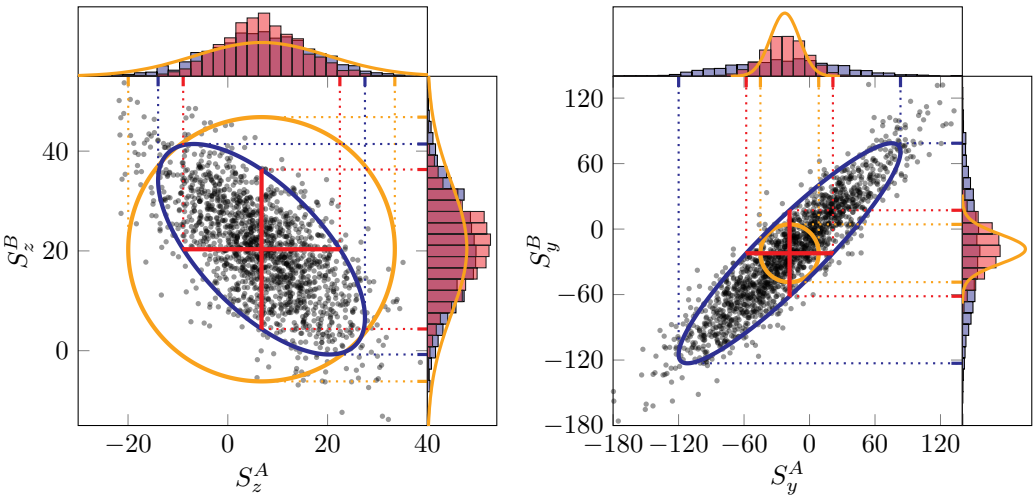

Figure 4.9: Spin correlations between the two BECs and illustration of the inference mechanism. The semitransparent grey dots are individual data points of simultaneous measurements of spin components $\hat{S}_z^A$ and $\hat{S}_z^B$ (left plot) and $\hat{S}_y^A$ and $\hat{S}_y^B$ (right plot) of the two systems. Data points for S_y^B are corrected for the phase shift due to the measured trigger jitter of the microwave generator (see Sec. 4.5.2). The blue histograms are their marginal distributions, 2σ intervals are indicated by blue dotted lines. The correlations of measurement results (2σ covariance ellipses in blue) allow one to infer measurement results of one system from the other. This reduces the variance of the prediction as shown by the histograms and the reduced 2σ intervals in red. For comparison, the 2σ variance ellipses of ideal non-entangled states with the same number of atoms are shown in yellow.

where $\mathrm{Cov}(\hat{S}^A_{z,y}, \hat{S}^B_{z,y})$ is the covariance of $\hat{S}^A_{z,y}$ and $\hat{S}^B_{z,y}$, the measurements of the squeezed (anti-squeezed) component of the two systems are expected to show negative (positive) correlations, in agreement with Fig. 4.9.

As discussed in Sec. 4.2, these correlations allow us to use the measurement results from one system to infer those of the other with an accuracy quantified by the inference variances, which are combined in the criteria Eqs. (4.2) and (4.3). In the following I illustrate a few features of the inference variances by focussing on the example

$$\mathrm{Var}_{\mathrm{inf}}\left(\hat{S}^B_z\right) = \mathrm{Var}\left(\hat{S}^B_z - \hat{S}^{B,\mathrm{inf}}_z\right) = \mathrm{Var}\left(\hat{S}^B_z + g^{A\to B}_z \hat{S}^A_z - c^{A\to B}_z\right), \quad (4.8)$$

but the discussion applies to $\mathrm{Var}_{\mathrm{inf}}(\hat{S}^B_y)$, $\mathrm{Var}_{\mathrm{inf}}(\hat{S}^A_z)$, and $\mathrm{Var}_{\mathrm{inf}}(\hat{S}^A_y)$, as well. The value of the gain factor that minimises the inference variance is given by

$$g^{A\to B}_z = -\frac{\mathrm{Cov}(\hat{S}^A_z, \hat{S}^B_z)}{\mathrm{Var}(\hat{S}^A_z)}, \quad (4.9)$$

which can be determined experimentally. The parameter $c^{A\to B}_z$, on the other hand, is chosen to make the mean value of the estimate ($\hat{S}^{B,\mathrm{inf}}_z$) coincide with that of the inferred quantity ($\hat{S}^B_z$), but has no effect on the inference variance, since it is an additive constant.

The quantity whose variance is taken in Eq. (4.8) can be visualised on the correlation plot as an affine transformation of the data points,

$$\left(S^A_z, S^B_z\right) \mapsto \left(S^A_z, S^B_z + g^{A\to B}_z S^A_z - c^{A\to B}_z\right), \quad (4.10)$$

which reduces the width of their distribution in the direction of the inferred spin component, S^B_z. The effect of this transformation can be understood with the help of the 2σ covariance ellipse of the data (blue in Fig. 4.9), which is deformed in the inferred direction until its width is minimised. The minimal width achievable by such a transformation corresponds to the width of the initial ellipse in the inferred direction at its centre, shown by the solid red lines in Fig. 4.9.

The variance reduction obtained by the inference corresponds to the difference between the 2σ interval of the data (given by the projection of their covariance ellipse onto the S_B axis, shown by the dashed blue lines in Fig. 4.9) and that of the transformed quantity from Eq. (4.10) (red solid lines). The distributions of S^B_z and $S^B_z + g^{A\to B}_z S^A_z - c^{A\to B}_z$ can be seen from the corresponding marginal histograms (blue and red in Fig. 4.9, respectively). Quantitatively, the variances of $S^{A,B}_z$ are reduced by a factor of 1.7 and those of $S^{A,B}_y$ by 7. The difference between these factors can be explained by the

comparison between the correlated and uncorrelated noise in the two cases: The correlated noise of $S_z^{A,B}$ consists almost entirely of quantum fluctuations, whereas in the case of $S_y^{A,B}$ it also includes the phase noise from the initial state preparation[4] (see Sec. 4.3). In addition to this, the quantum fluctuations of $S_z^{A,B}$ are much smaller than those of $S_y^{A,B}$, while several sources of technical uncorrelated noise (e.g., detection noise) affect both spin directions in the same way. Therefore, the noise that is eliminated by the inference (i.e. the correlated one) in the z spin direction constitutes a much smaller fraction of the total variance than in the y direction. This is also reflected by the values of the optimal gain factors,

$$\begin{aligned} g_z^{A\to B} &= -0.65(2), \\ g_z^{B\to A} &= -0.65(2), \\ g_y^{B\to B} &= 0.91(1), \\ g_y^{B\to A} &= 0.92(1). \end{aligned}$$

Although both the entanglement and the EPR criteria are based on the variance reduction described above, the optimal gain factors for $\mathcal{E}_{\mathrm{ent}}$ are different from those that minimise the inference variances (hence $\mathcal{E}_{\mathrm{EPR}}^{A\to B}$ and $\mathcal{E}_{\mathrm{EPR}}^{B\to A}$), see Sec. 4.2. In particular, since they also contribute to the numerator of $\mathcal{E}_{\mathrm{ent}}$, those for the entanglement criteria tend to be larger,

$$\begin{aligned} g_z^{A\to B,\mathrm{ent}} &= -1.01(1), \\ g_y^{A\to B,\mathrm{ent}} &= 1.03(2). \end{aligned}$$

The yellow elements in Fig. 4.9 represent the 2σ variance ellipses and marginal distributions that one would expect if the two systems were prepared in ideal coherent spin states with the same atom numbers as in the measurements. From the comparison between these and the blue ellipses and histograms, it can be seen that both collective spin components retain part of the squeezing and anti-squeezing of the initial state. Indeed, the number squeezing of the two condensates considered individually amounts to

$$\begin{aligned} \zeta^2(\hat{S}_z^A) &= -2.2(2)\,\mathrm{dB}, \\ \zeta^2(\hat{S}_z^B) &= -2.2(2)\,\mathrm{dB}, \\ \zeta^2(\hat{S}_y^A) &= 11.5(2)\,\mathrm{dB}, \\ \zeta^2(\hat{S}_y^B) &= 11.9(1)\,\mathrm{dB}. \end{aligned}$$

[4]It is also worth noting that the phase noise from the initial state preparation results in positive correlations between S_y^A and S_y^B, i.e. with the same sign as the quantum correlations in this spin direction.

The combined measurement results, on the other hand, recover the statistics of the initial state, $\zeta^2(\hat{S}_z^A + \hat{S}_z^B) = -6.6(3)\,\mathrm{dB}$ and $\zeta^2(\hat{S}_y^A + \hat{S}_y^B) = 14.6(2)\,\mathrm{dB}$, consistent with our expectations.

As mentioned earlier, evaluating the criteria Eqs. (4.2) and (4.3) also requires measuring $\langle \hat{S}_x^{A,B} \rangle$, which quantify the lengths of the collective spins. In the case of the EPR criteria, these determine the Heisenberg uncertainty bounds which the inference variances have to violate to demonstrate the EPR paradox, as $[\hat{S}_y^{A,B}, \hat{S}_z^{A,B}] = i\hat{S}_x^{A,B}$. In the entanglement criterion, on the other hand, the denominator of $\mathcal{E}_{\mathrm{ent}}$ is a result of the mathematical derivation and has no simple interpretation. The collective spin lengths normalised to half the atom numbers correspond to the interferometric contrasts, $2|\langle \hat{S}_x^{A,B} \rangle|/\langle \hat{N}^{A,B} \rangle$, which are measures of the overall coherence of the process[5] [57]. We obtain $96.2(1)\,\%$ contrast for both $\hat{\vec{S}}^A$ and $\hat{\vec{S}}^B$, which is comparable to the contrast we measure without splitting the condensate (see Sec. 4.3). This indicates that the coherence and overlap between the spin components in each system are preserved by the splitting procedure.

Combining all measurements to evaluate the criteria Eqs. (4.2) and (4.3), we obtain the values

$$\begin{aligned} \mathcal{E}_{\mathrm{Ent}} &= 0.35(2), \\ \mathcal{E}_{\mathrm{EPR}}^{A\to B} &= 0.81(3), \\ \mathcal{E}_{\mathrm{EPR}}^{B\to A} &= 0.77(3), \end{aligned}$$

demonstrating both entanglement and the EPR paradox between the condensates A and B, inferring both from $A \to B$ and from $B \to A$. The measured values of S_y^B used for the evaluation of the EPR criteria are corrected for phase shifts induced by triggering delay fluctuations in the signal generation, see Sec. 4.5.2. In addition to the criteria, we evaluate the Heisenberg uncertainty products defined in Eq. (4.1), obtaining

$$\begin{aligned} \mathcal{E}_{\mathrm{Hei}}^{B} &= 10.2(4), \\ \mathcal{E}_{\mathrm{Hei}}^{A} &= 9.2(5). \end{aligned}$$

Since ideal squeezed spin states saturate the Heisenberg limit, we conclude that $\mathcal{E}_{\mathrm{Hei}}^A$ and $\mathcal{E}_{\mathrm{Hei}}^B$ are larger than unity due to technical noise. Comparing $\mathcal{E}_{\mathrm{EPR}}^{A\to B}$ to $\mathcal{E}_{\mathrm{Hei}}^B$ and $\mathcal{E}_{\mathrm{EPR}}^{B\to A}$ to $\mathcal{E}_{\mathrm{Hei}}^A$ allows us to quantify the variance reduction gained by the inference.

[5] This can be understood from the fact that, because of the spin rotations used to measure $\hat{S}_x^{A,B}$ and $\hat{S}_y^{A,B}$ (see Sec. 3.4.1), the measurements of these spin directions correspond to the maximum and the zero crossing of a Ramsey fringe, respectively.

All criteria are determined without any technical noise subtraction, i.e. we do not subtract from the inference variances any estimated contribution from technical noise. Due to this, the entanglement and EPR entanglement demonstrated here are directly accessible experimentally and can be used as resources in applications, see Sec. 5.2.

4.5.1 Data analysis

The results listed in Sec. 4.5 were obtained by taking a total of about 4500 measurements within 42 hours of measurement time. We subdivide the data into blocks for which we evaluate the criteria separately. Each block consists of hundred $\hat{S}_z$, hundred $\hat{S}_y$, and twenty $\hat{S}_x$ measurements. The measurements along $\hat{S}_x$ are performed ten times along both the positive and the negative spin direction, to reduce bias from a potential difference in the detectivity of different states – which we did however not observe. The subdivision into blocks renders the analysis robust against the effect of small, slow drifts of the experimental conditions during the tens of hours of measurement time, while the quantum noise of the atoms, which is present in each shot of the experiment, is unchanged. The values of the EPR and entanglement criteria listed in Sec. 4.5 are the averages of the values obtained for the individual blocks. We verified that analysing the whole data set in one block does not change the conclusions of our work qualitatively: In this case we obtain $\mathcal{E}_{\mathrm{EPR}}^{A\to B} = 0.87(4)$ and $\mathcal{E}_{\mathrm{EPR}}^{B\to A} = 0.82(4)$.

Since the imaging calibration relies on projection noise measurements performed with equal superpositions of all involved states (see Sec. 3.4.3), it is most accurate for the measurements of $\hat{S}_y^{A,B}$ and $\hat{S}_z^{A,B}$. In the measurements of $\hat{S}_x^{A,B}$, on the other hand, nearly all atoms occupy two states, and we observe a decrease on the order of 3 % in the detected total atom number. Since the only difference between the pulse sequences used to measure $\hat{S}_x^{A,B}$ and $\hat{S}_y^{A,B}$ is the phase of the individual rotations, we exclude that this effect is due to atom losses and we attribute it to an effective decrease in detectivity due to the larger density of the cloud. To correct for this effect, we determine the mean value of $\hat{S}_x^{A,B}$ as $\langle \hat{S}_x^{A,B} \rangle = \langle N_{\mathrm{rel},x}^{A,B} \rangle \langle N_{z,y}^{A,B} \rangle / 2$, i.e. we take the mean value of the relative atom number imbalance in the $\hat{S}_x^{A,B}$ measurements, $N_{\mathrm{rel},x}^{A,B} \coloneqq (N_{1,x}^{A,B} - N_{2,x}^{A,B})/(N_{1,x}^{A,B} + N_{2,x}^{A,B})$, and multiply it by half the total atom number detected in the measurements along y and z, $\langle N_{z,y}^{A,B} \rangle / 2$.

In the following I list the variances, inference variances (those used for the EPR criteria), and mean values that result from our measurements. Like the criteria, these quantities were evaluated individually for every block of data, then averaged to obtain the values listed below. Because of this, combining

these values into the criteria yields slightly different results than those listed in Sec. 4.5.

$$\begin{aligned}
\mathrm{Var}(\hat{S}_y^A) &= 2535(105),\\
\mathrm{Var}(\hat{S}_z^A) &= 103.5(41),\\
\mathrm{Var}(\hat{S}_y^B) &= 2667(101),\\
\mathrm{Var}(\hat{S}_z^B) &= 106.8(44),\\
\mathrm{Var}_{\mathrm{inf}}(\hat{S}_y^A) &= 378(10),\\
\mathrm{Var}_{\mathrm{inf}}(\hat{S}_z^A) &= 60.5(20),\\
\mathrm{Var}_{\mathrm{inf}}(\hat{S}_y^B) &= 373(9),\\
\mathrm{Var}_{\mathrm{inf}}(\hat{S}_z^B) &= 62.3(20),\\
\langle \hat{S}_x^A \rangle &= 344(1),\\
\langle \hat{S}_x^B \rangle &= 338(1).
\end{aligned}$$

4.5.2 Signal generation and local oscillator noise

As described in Sec. 3.3.2, the mw and rf driving fields are generated by three commercial function generators, namely an IQ-modulated mw generator, a two-channel arbitrary waveform generator (that provides the IQ modulation signal), and a rf generator. The mw generator is operated in continuous-wave mode, whereas the other two devices are programmed with lists of frequencies, amplitudes, and phases that are executed upon trigger. In particular, the IQ modulator is triggered by the rf generator, which in turn is triggered by the experiment control system. Since these devices do not share a common sampling clock, their relative phases change between different experimental repetitions: The mw phase is completely random, whereas the phase difference between the rf generator and the IQ modulator varies based on the trigger delay fluctuations of the latter.

As long as we address the states $|1A\rangle$ and $|2A\rangle$ alone (e.g. in a standard Ramsey experiment), the phases of the signals only influence the absolute phase of the two-photon driving fields, which has no physical effect. Our sequence, on the other hand, is more complicated and the phase of the different signals does matter. Indeed, it turns out that the triggering delay fluctuations on the order of nanoseconds in the IQ generator result in phase fluctuations of system B that are large enough to degrade the EPR signal.

To illustrate this effect, let us consider a simplified experimental sequence, where the initial BEC is prepared in a coherent spin state on the equator

of the Bloch sphere by a $\pi/2$ pulse at the time t_0. After a duration t_1, the BEC is split into condensate A and B, and after t_2 the phases of the two systems are read out by another $\pi/2$ pulse. We assume for simplicity that all pulses are done instantaneously, or equivalently that their detuning with respect to the atomic transition does not matter. As shown in appendix D, this scenario results in the following measured phases of the two systems,

$$\phi_A = 0, \tag{4.11}$$

$$\phi_B = \omega_{\mathrm{rf}} \delta t, \tag{4.12}$$

where $\omega_{\mathrm{rf}} \simeq 1.79\,\mathrm{MHz}$ is the rf frequency and δt is the triggering delay of the IQ generator. We measure typical timing fluctuations of δt of $\sigma_{\delta t} = 4.0\,\mathrm{ns}$, which result in phase fluctuations of $\sigma_{\phi_B} = 4.5 \times 10^{-2}\,\mathrm{rad}$ and thus in the additional collective spin variance of ≈ 260 in the phase-sensitive measurements of system B, i.e. along $\hat{S}_y^B$. Since the latter is the anti-squeezed direction, this effect is actually small when compared to the measured variance, see Sec. 4.5.1. For the much smaller inference variances, on the other hand, it is relevant.

These fluctuations are a technical limitation, which we plan to overcome in the future by generating the rf and the IQ signals with a single device (i.e. sharing the same sampling clock). In the present work, we correct for them by directly measuring δt, which we determine in each shot of the experiment by comparing with an oscilloscope the phase of the radio-frequency generator with the starting time of the IQ modulator sequence. This classical information can be used for a better estimation of $\hat{S}_y^B = \hat{S}_{y,\mathrm{measured}}^B + g_{\delta t}\delta t$, where $g_{\delta t}$ is a gain parameter chosen to minimise the variance of $\hat{S}_y^B$. We use this correction both in the data points of S_y^B shown in Fig. 4.9 and in the evaluation of the EPR criterion, Eq. (4.2). We stress that, while this correction can reduce classical noise, it cannot lead to a violation of the EPR inequality, which can only be achieved by sufficiently strong entanglement between the two systems [9]. On the other hand, this correction is not applied in the evaluation of the entanglement criterion, Eq. (4.3), which was derived following a different principle (see Sec. 4.2).

4.6 Measuring the two systems in different bases

Although we rotate $\hat{\vec{S}}^A$ and $\hat{\vec{S}}^B$ individually, the results presented in Sec. 4.5 are obtained by measuring the two spins in the same basis. Since many applications of EPR entanglement require performing different measurements

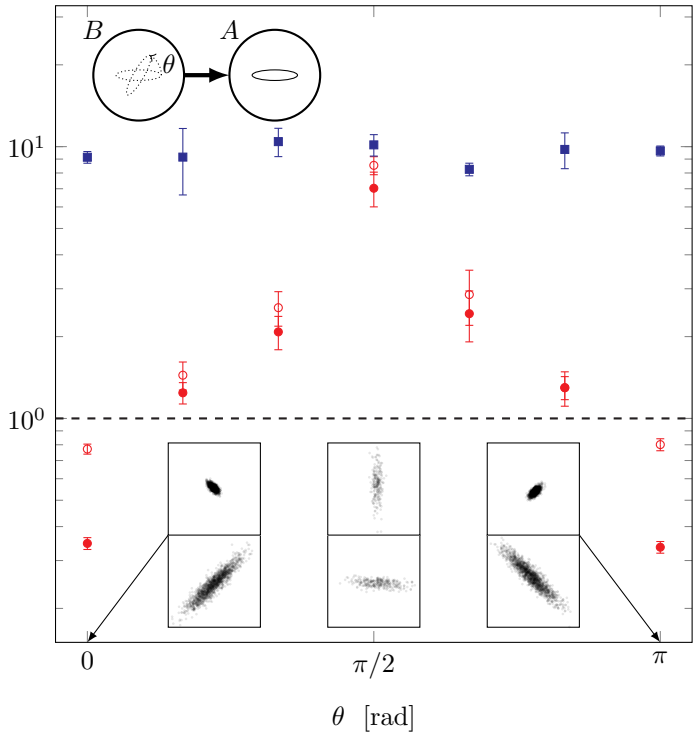

Figure 4.10: Individual manipulation of the two entangled BECs. The plot shows the results of EPR experiments in which $\hat{\vec{S}}^B$ is rotated by an angle θ around the x axis with respect to $\hat{\vec{S}}^A$, as sketched in the inset on the top left. The red filled circles represent $\mathcal{E}_{\mathrm{ent}}$, red empty circles $\mathcal{E}_{\mathrm{EPR}}^{B\to A}$, and blue squares $\mathcal{E}_{\mathrm{Hei}}^{A}$. The EPR paradox (entanglement) is observed if $\mathcal{E}_{\mathrm{EPR}}^{B\to A}$ ($\mathcal{E}_{\mathrm{ent}}$) falls below the dashed line at unity. The insets at the bottom show the spin correlations similar to Fig. 4.9, with $\hat{S}_z$ on top and $\hat{S}_y$ at the bottom, for $\theta = 0,\ \pi/2$, and π. The numerical values of the criteria and Heisenberg products are listed in Tab. 4.1.

θ	$\mathcal{E}_{\mathrm{ent}}$	$\mathcal{E}_{\mathrm{EPR}}^{B\to A}$	$\mathcal{E}_{\mathrm{Hei}}^{A}$
0°	0.35(2)	0.77(3)	9.2(5)
30°	1.2(1)	1.4(2)	9.2(25)
60°	2.1(3)	2.6(4)	10(1)
90°	7.0(10)	8.5(6)	10(1)
120°	2.4(5)	2.9(7)	8.3(4)
150°	1.3(2)	1.3(1)	9.8(14)
180°	0.34(2)	0.80(4)	9.6(4)

Table 4.1: Numerical values of the criteria and Heisenberg products plotted in Fig. 4.10, i.e. the results of EPR experiments in which $\hat{\vec{S}}^B$ is rotated by an angle θ around the x axis with respect to $\hat{\vec{S}}^A$. The EPR paradox (entanglement) is observed if $\mathcal{E}_{\mathrm{EPR}}^{B\to A}$ ($\mathcal{E}_{\mathrm{ent}}$) is smaller than 1.

on the two systems, it is important to demonstrate that our experiment is able to maintain the entanglement between $\hat{\vec{S}}^A$ and $\hat{\vec{S}}^B$ in this process. Figure 4.10 shows the results of EPR experiments in which $\hat{\vec{S}}^B$ is rotated by an angle θ around the x axis with respect to $\hat{\vec{S}}^A$, as sketched in the inset on the top left. The numerical values of the criteria and Heisenberg products are listed in Tab. 4.1.

The experimental sequence here is the same as in Sec. 4.5, but the individual rotation of system B is modified to obtain the desired angle. In the case of the $\hat{S}_z^{A,B}$ measurements, which require no change of basis before detection, this amounts to introducing a θ rotation around the $\hat{S}_x^B$ axis. For the $\hat{S}_y^{A,B}$ measurements, the angle θ is added to the $\pi/2$ rotation that carries out the change of basis (see Sec. 3.4.1); if $\pi/2+\theta>\pi$, we perform a rotation by $2\pi-(\pi/2+\theta)$ around the $-\hat{S}_x^B$ axis instead (i.e. in the opposite direction), in order to minimise the pulse duration. The $\hat{S}_x^{A,B}$ measurements are unchanged w.r.t. Sec. 4.5, as the additional rotation does not have any measurable effect on this spin component.

The case $\theta=0$ (leftmost points in Fig. 4.10) corresponds to the same configuration as in Sec. 4.5, i.e. simultaneous measurements of the same spin component. As θ increases, the correlations decrease and vanish almost completely for $\theta=\pi/2$, where orthogonal spin components are measured on the two condensates (see in the inset plot at the bottom centre of Fig. 4.10). Since the inference is based on the correlations, the values of $\mathcal{E}_{\mathrm{EPR}}^{B\to A}$ and $\mathcal{E}_{\mathrm{ent}}$ increase as these get weaker, and for $\theta=\pi/2$ the value of $\mathcal{E}_{\mathrm{EPR}}^{B\to A}$ is compatible with $\mathcal{E}_{\mathrm{Hei}}^{A}$, indicating that no meaningful noise reduction can be obtained.

Increasing θ further than $\pi/2$, the correlations gradually reappear, but

with opposite sign, since the spin components are now being anti-aligned, see the inset plot at the bottom right of Fig. 4.10. At $\theta = \pi$, the criteria $\mathcal{E}_{\rm ent}$ and $\mathcal{E}_{\rm EPR}^{B\to A}$ reach comparable values as for $\theta = 0$, demonstrating that the manipulation does not degrade the entanglement between the two condensates. It is worth noting that in this case an additional π pulse is applied to system B w.r.t. $\theta = 0$; the fact that we obtain comparable values for $\mathcal{E}_{\rm ent}$ and $\mathcal{E}_{\rm EPR}^{B\to A}$ in these two cases shows the high quality of the rotations of $\hat{\vec{S}}^B$.

In the setting $\theta = \pi/2$ our experiment realises a situation discussed by Schrödinger in his reaction to the EPR paradox [2, 3], where the values of two non-commuting observables of system A are apparently measured in a single experimental run: One (say, $\hat{S}_z^A$) by direct measurement on A and the other ($\hat{S}_y^A$) by exploiting the strong correlations to infer its value from the simultaneous measurement on B. Under the local realist assumptions that measurements reveal pre-existing properties of a system and that simultaneous measurements on spatially separated systems do not disturb each other, the restrictions imposed by the Heisenberg uncertainty relation could thus be overcome [2, 3]. Today, however, we know that local realism is inconsistent with the results of increasingly rigorous experimental tests of Bell inequalities [11–18]. In the spirit of Peres' statement that "unperformed experiments have no results" [108], we should thus refrain from inferring a value for $\hat{S}_y^A$ if it is not actually measured on system A.

Chapter 5

Summary and outlook

5.1 Summary

In this thesis I report the observation of the EPR paradox between two spatially separated, massive many-particle systems [36]. Our experiment begins by preparing a two-component BEC composed of ≈ 1400 ^{87}Rb atoms in a squeezed spin state with number squeezing $\zeta^2 = -7\,\mathrm{dB}$. We then implement a beam splitter in spin space by coherently transferring half of the atoms in the two BEC components to different states. The difference in magnetic moment between the initial and the new states allows us to split them into two spatially separated two-component BECs by means of magnetic field gradients. This procedure preserves both the overlap and the coherence between the components of the resulting condensates, allowing us to individually rotate their collective spins. The many-particle entanglement present in the initial BEC is inherited in the form of bipartite entanglement between the split condensates [92], which turns out to be strong enough to violate the EPR-Reid inequality, Eq. (4.2).

Our work is relevant in the context of testing quantum mechanics with systems of increasing size and complexity. Indeed, although the EPR paradox and Bell nonlocality have been observed with systems composed of few particles, how far these quantum effects extend into the macroscopic world (where local realism is still accepted nowadays) remains an open question. Our result shows that the conflict between quantum mechanics and local realism does not disappear in systems composed of 10^3 massive particles.

5.2 Outlook

EPR entanglement of two spatially separated systems in conjunction with the ability to individually manipulate them opens up a variety of possibilities. On the fundamental side, being able to measure the two collective spins in different bases brings us closer to a Bell test with many-particle systems, which however requires non-Gaussian measurements or state preparation, e.g. single-atom resolving detection [104].

From the perspective of applications, EPR entanglement is a valuable resource for quantum technology. The noise reduction gained from the inference in Eq. (4.2), quantified by the difference between the Heisenberg products and the EPR criteria, translates to a metrological enhancement that can be exploited in quantum sensing [109–112]. Furthermore, EPR entanglement is the resource that guarantees the efficacy of certain quantum information protocols, such as quantum teleportation, entanglement swapping, one-sided device-independent quantum key distribution, or randomness certification [9, 97, 98].

Our experiment is particularly suited for quantum metrology applications [35, 78]. One can, e.g., use one of the two systems as a small sensor to probe fields and forces with high spatial resolution and the other one as a reference to reduce the quantum noise of the first system. Moreover, the experimental techniques demonstrated here will enable entanglement-enhanced multiparameter estimation along the lines of Ref. [112], which proposes a protocol to measure field distributions with an array of individually addressable systems originating from the splitting of a squeezed spin state, and demonstrates that the entanglement inherited from the initial state enhances the field sensitivity.

The metrology applications mentioned above can be implemented without any modification to the experimental apparatus. However, in the future it can be interesting to make a few changes to the experiment, in order to further improve its performance and gain new possibilities. First of all, we plan to solve the problem of phase noise due to trigger delay oscillations in the signal generators, discussed in Sec. 4.5.2, by replacing the IQ modulator and the rf generator with a single device, since producing both signals with a common sampling clock would guarantee their relative phase stability.

As discussed in Sec. 4.4.3, the splitting pulses and the individual rotations of the two condensates pose the problem of avoiding the accidental driving of undesired close-to-resonance transitions. Although in the experiments presented here this could be solved by frequency selectivity alone, it sets several constraints on the Rabi frequencies and pulse durations that can be chosen. For this reason, having control over the polarisation of the driving

fields would give us much more flexibility. However, this is not achievable with the current mw and rf driving fields, due to the presence of several metallic structures within a wavelength from the atoms, see Sec. 3.3.2. To circumvent this, one could think of using lasers to perform the coherent manipulations via Raman transitions, instead.

Finally, it can be interesting to investigate the production of stronger entanglement in our system. The most straightforward way to achieve this with our apparatus is by increasing either the strength of the state-dependent potential or the time for which it is activated: As mentioned in Sec. 2.3.5, for $\chi t \gtrsim N^{-2/3}$ the state of the system is over-squeezed, and for $\chi t = \pi/2$ a Schrödinger cat state is produced[1]. This would yield more resources for applications (e.g. for metrology [57, 65]) and possibly enable us to perform a Bell test with two multi-particle systems, as mentioned above. However, these states are less robust against noise and particle losses than squeezed spin states (to make an extreme example, a Schrödinger cat state is destroyed by the loss of one atom) and require more elaborate detection schemes (e.g. see Ref. [66–68]). Thus, working in this regime would necessitate the development of an experimental scheme robust to decoherence (e.g. see Ref. [113]) and further improvements in the stability and noise performance of our apparatus (the values of the Heisenberg products listed in Sec. 4.5 show a relevant amount of technical noise).

Thus, there are prospects for performing exciting experiments with our current apparatus, as well as for developing it further to improve its performance and explore new possibilities.

[1] In our case the one-axis-twisting parameter χ is not constant in time, thus the product χt should be substituted by the integral $\int_0^t \chi(t')\mathrm{d}t'$.

Appendix A

IQ modulation programming

With respect to previous work performed with our apparatus, the experiments presented in this thesis require a higher degree of control on the mw signals: In the previous version of the mw generation (described in Ref. [69]) a continuous-wave mw signal – gated by a switch for pulse timing – was used. Now several pulses at different frequencies and with independent phase control, some of which contain two tones, are needed. Since all required mw frequencies are a few MHz apart, this was achieved by an IQ-modulated mw generator[1], which receives the modulation signal by a two-channel waveform generator[2], see Sec. 3.3.2. This device is required to emit a sequence of one- and two-tone signals with independent frequency, amplitude, and phase control. Although the device has two DDS-like sources for each channel, its firmware is not capable of programming suitable signals, forcing us to program them point by point and play them as arbitrary waveforms.

The number of samples that we can program is limited both by the memory of the device (16 MSamples) and by the time taken by the upload process, which can exceed the duration of the initial cooling stages and cause the waveform generator not to be ready to execute the sequence when it is supposed to. Due to this, we substitute the single-tone signals with repeated shorter waveforms. These shorter waveforms need to last an integer number of samples, which in most cases forces us to approximate the frequency of these signals. To find the best approximation, we first calculate the maximum number of periods that fit in the the largest number of samples allowed

[1] Rohde & Schwarz SGS100A.

[2] Keysight 33522B, 30 MHz bandwidth, 250 MHz sampling rate, with the following optional additions: IQ baseband signal player, high-stability OCXO timebase, and 16 MSample memory.

in one waveform, $N_{\text{samp}}^{\max}$,

$$N_{\text{per}}^{\max} = \left\lfloor \frac{f\, N_{\text{samp}}^{\max}}{f_{\text{samp}}} \right\rfloor, \tag{A.1}$$

where f is the desired frequency[3], f_{samp} is the sampling rate, and $\lfloor x \rfloor$ is the largest integer smaller than x. For every possible number of periods $N_{\text{per}} \in \{1, \ldots, N_{\text{per}}^{\max}\}$, we find the number of samples which best approximates its duration,

$$N_{\text{samp}}^{\text{appr}}(N_{\text{per}}) = \left\lfloor \frac{f_{\text{samp}}\, N_{\text{per}}}{f} \right\rceil, \tag{A.2}$$

where $\lfloor x \rceil$ is the closest integer to x. This corresponds to the approximated frequency

$$f^{\text{appr}}(N_{\text{per}}) = \frac{f_{\text{samp}}\, N_{\text{per}}}{N_{\text{samp}}^{\text{appr}}(N_{\text{per}})}, \tag{A.3}$$

which has an error w.r.t. the desired frequency

$$f^{\text{err}}(N_{\text{per}}) = |f - f^{\text{appr}}(N_{\text{per}})|. \tag{A.4}$$

We choose the value of N_{per} for which the error is minimal (in case this is not unique, we choose the smallest such value of N_{per}). We can estimate the maximum error as the half free spectral range between two contiguous samples for the largest possible number of periods, $N_{\text{per}} = N_{\text{per}}^{\max}$, which represents the worst-case scenario where no smaller choice of N_{per} yields a better result,

$$f^{\text{err}}(N_{\text{per}}^{\text{best}}) \lesssim \frac{f}{2N_{\text{samp}}^{\max}}. \tag{A.5}$$

Note that this is merely an upper bound to the frequency error and that in most cases the approximation is much better.

Since the total duration of the signals does not in general coincide with an integer number of repeated waveforms, we add a smaller "rest waveform" after the repetitions to ensure the timing accuracy of the signals.

The substitution with repeated smaller waveforms cannot be done reasonably for two-tone signals, which have a potentially very long periodicity. However, in the experiments presented in this thesis we only execute two-tone signals for less than a millisecond, as opposed to the hundreds of milliseconds during which single-tone signals are needed. Thus, programming the whole two-tone part point by point does not cause any memory issue.

[3]We assume $f \geq 0$. For $f < 0$, the absolute value of f is used by the algorithm and its sign is added to the result.

Appendix B

Elliptical regions of interest

As mentioned in Sec. 3.4.4, in order to reduce photon shot noise, we choose the regions of interest to count atoms from the acquired images to be as small as possible, while still including nearly all of the atomic signal. Because of the shape of the expanded BEC, this is achieved by elliptical regions, see Fig. B.1. These are selected individually for each state, starting from large rectangular regions (which include all of the atomic signal). Our algorithm produces all possible elliptical regions[1] included in the rectangular ones and, for each of them, calculates the included fraction of the total atomic signal, based on the average of the measured images. It then selects the smallest one including a fraction of the atomic signal above a user-defined threshold.

Executing this algorithm with a threshold close to unity causes the placement of the regions to depend strongly on the signal at the edge of the atomic clouds, which is dominated by noise and small interference fringes. This can result in regions de-centred by a few pixels with respect to the clouds. In order to circumvent this problem, we execute the algorithm with a lower threshold (typically 85 %) and add a few pixels to the ellipse radii (typically 3 pixels in all directions). In this way, the position and shape of the ellipses are chosen based on the strong-signal part of the images, and the resulting regions of interest include $\approx 97\,\%$ of the total atomic signal. An example of averaged images alongside the resulting regions of interest is shown in Fig. B.1.

[1] The possible elliptical regions are restricted to those with size and position that can be expressed by an integer number of pixels.

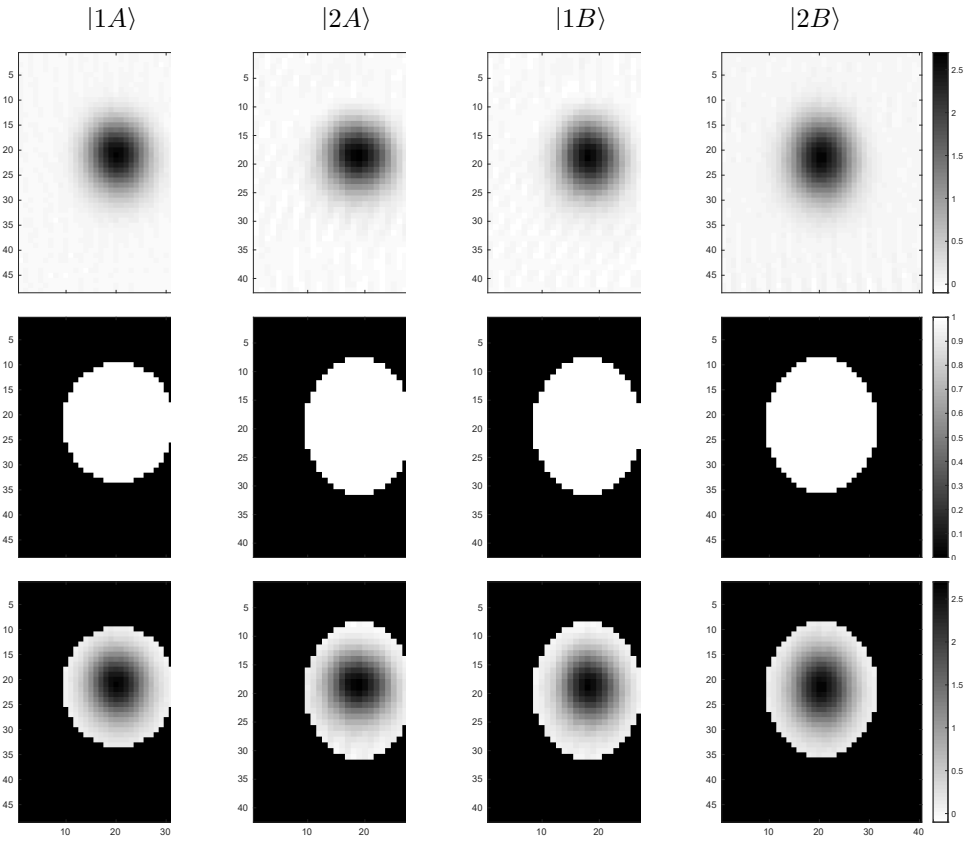

Figure B.1: Typical averaged images (top row), the selected elliptical regions of interest (middle row), and their overlap (bottom row).

Appendix C

Typical calibration measurements

In this appendix I review the most common calibration measurements performed in our experiment. In the following I will refer to the act of repeating a certain experimental sequence while changing the value of a certain parameter to cover a given range of values as *scanning* that parameter.

C.1 Cooling sequence

The cooling sequence is optimised to obtain as many atoms as possible in the BEC. This is typically done by scanning some experimental parameters and measuring the atom number after the second-to-last evaporative cooling stage[1]. The parameters that we scan on a regular basis are the bias field values during all laser cooling stages and the laser power during the optical pumping. All other parameters (e.g. those relevant to the evaporative cooling sequence) normally do not require being modified as often and are checked at most once a year.

C.2 Magnetic field calibration

In order to make sure that the total magnetic field at the centre of the trap is equal to the magic field (see Sec. 2.3.1), we perform the spectroscopy of the transition $|F = 1, m_F = -1\rangle \leftrightarrow |F = 2, m_F = 0\rangle$, which has a large differential Zeeman shift and is thus sensitive to magnetic field variations: After

[1]The reason why we do not base our calibrations on the final atom number is that the last evaporative cooling stage has the effect of stabilising it (see Secs. 3.3.1 and 3.6), making it a less sensitive signal.

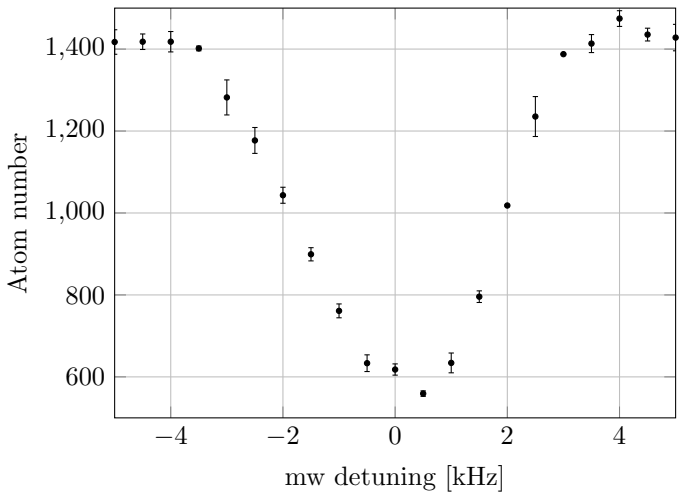

Figure C.1: Single-photon mw spectroscopy of the transition $|F = 1, m_F = -1\rangle \leftrightarrow |F = 2, m_F = 0\rangle$, used to calibrate the magnetic field at the trap centre. The horizontal axis represents the detuning of the applied mw field w.r.t. its theoretical value at the magic field.

preparing the BEC, we apply a mw Rabi pulse with pulse area $\Omega^{2,0}_{1,-1}t \approx \pi/2$, whose frequency is scanned around the theoretical value for this transition at the magic field. At the frequencies close to resonance with the transition, a part of the atoms will be transferred to the state $|F = 2, m_F = 0\rangle$ and will not be detected, see Fig. C.1. The detuning from the theoretical value, together with the magnetic field dependence of the transition ($\approx 0.70\,\mathrm{MHz/G}$, see Sec. 2.3.1), allows us to correct the value of the x bias field.

To reduce the power and Fourier broadening of the transition, we use much lower mw power and longer pulse duration than for normal internal state manipulations, typically $t \approx 20\,\mathrm{ms}$. This yields a spectroscopic resolution better than 0.5 kHz, which is finer than what we can correct for – the resolution of the analogue channels of the NI cards limits the control of the x bias field to steps equivalent to 0.9 kHz.

C.3 Rabi frequency calibration

The Rabi frequency calibration consists of adjusting the Rabi pulse duration to obtain the wished pulse area Ωt. Thus, we commonly use the so-called $\pi/2$ time $t_{\pi/2}$ (defined by $\Omega t_{\pi/2} = \pi/2$) as a parameter instead of the Rabi frequency itself.

We calibrate $t_{\pi/2}$ by driving Rabi oscillations – i.e. by scanning the Rabi

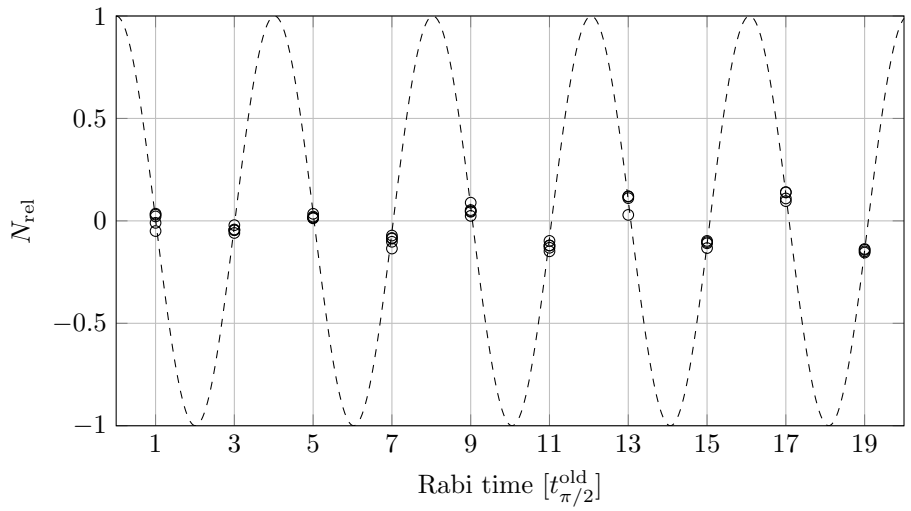

Figure C.2: Rabi frequency calibration measurement. The horizontal axis shows the Rabi time and the vertical axis the normalised atom number imbalance, N_{rel}. The empty circles show the experimental data, whereas the dashed curve represents the Rabi oscillation fit given by Eq. (C.1).

pulse duration and measuring the atom number in the two states. If we already have a good guess of its value $t^{\mathrm{old}}_{\pi/2}$ (which is mostly the case), we only measure odd multiples of $t^{\mathrm{old}}_{\pi/2}$, i.e. where $\langle N_{\mathrm{rel}}\rangle = \langle (N_1 - N_2)/(N_1 + N_2)\rangle \simeq 0$ is most sensitive to variations. Assuming the Rabi oscillations are driven resonantly, $\langle N_{\mathrm{rel}}\rangle$ after a pulse of duration $nt^{\mathrm{old}}_{\pi/2}$, where n is an odd integer, is given by

$$\langle N_{\mathrm{rel}}\rangle_n = \cos\left(n\frac{\pi}{2}\frac{t^{\mathrm{old}}_{\pi/2}}{t_{\pi/2}}\right), \tag{C.1}$$

see Fig. C.2. Typically, we scan n from 1 to about 19 and fit $\langle N_{\mathrm{rel}}\rangle_n$ as a function of n to obtain $t_{\pi/2}$. Due to their higher sensitivity to Rabi frequency variations, we give higher fit weight to data points with larger n, whereas we measure those with small n to avoid issues with periodicity (as long as $t^{\mathrm{old}}_{\pi/2} < 2t_{\pi/2}$).

C.4 Two-photon resonance

The typical two-photon Rabi frequency of the collective spin rotations is $\Omega \approx 2\pi \times 750\,\mathrm{Hz}$. Thus, in order to attain high-fidelity manipulations, we need the detuning of the two-photon signal, Δ, to be at most on the level of few Hz.

Assuming $\Delta \ll \Omega$, we use a Ramsey-like experiment to measure the phase accumulation caused by the detuning (see Sec. 3.3.2): We first perform a $\pi/2$ pulse, during which a phase $\Delta t_{\pi/2}$ is accumulated. Then, we perform a second $\pi/2$ pulse with a phase of $\varphi = \pm\pi/2$ w.r.t. the first one, which maps the accumulated phase to an atom-number imbalance, $\langle N_{\mathrm{rel}}\rangle_{\pm} \simeq \pm\sin\big(\Delta t_{\pi/2}\big) \simeq \pm\Delta t_{\pi/2}$, where we made use of the assumption that $\Delta \ll \Omega$. The detuning is thus given by

$$\Delta \simeq \frac{\langle N_{\mathrm{rel}}\rangle_{+} - \langle N_{\mathrm{rel}}\rangle_{-}}{2t_{\pi/2}}, \tag{C.2}$$

where we expressed Δ in terms of $t_{\pi/2}$ instead of Ω, because $t_{\pi/2}$ is the more commonly used parameter of the two – we usually calibrate the pulse duration, see appendix C.3. It is worth noting that it is not necessary to measure both $\varphi = +\pi/2$ and $\varphi = -\pi/2$, but doing so accounts for small errors in the detection balance calibration (see Sec. 3.4.3), making our estimate of Δ more reliable.

C.5 Ramsey phase calibration

As the results presented in this thesis are based on a sequence of collective spin rotations, between which phase-changing processes take place, it is important to determine the phase of the system at the time of the rotations. This is done by performing Ramsey interferometry experiments (see Sec. 2.3.7): Since all coherent manipulations in the experiments presented here (except for the choice of measurement basis) leave the state of the system on the equator of the many-particle Bloch sphere ($\langle \hat{S}_z\rangle \simeq 0$), one can interrupt the experimental sequence at any point and perform a $\pi/2$ pulse, scan its phase, and obtain a Ramsey fringe, which be fitted by Eq. (2.35).

C.6 Demixing-remixing dynamics

Fig. C.3 shows the experimental sequence we use to obtain spin squeezing: The BEC is prepared in a CSS on the equator of the many-particle Bloch sphere, $|\mathrm{CSS} : \pi/2, 0\rangle$, by a Rabi $\pi/2$ pulse. Then, the CPW mw generates a state-dependent dressing potential for a duration t_{sdp}, inducing the demixing-remixing dynamics described in Sec. 3.3.3, which activate the OAT term, $\hbar\chi\hat{S}_z^2$, in the collective spin Hamiltonian Eq. (2.17). This produces a SSS, whose variance reduction w.r.t. a CSS (*number squeezing*) and minimal variance direction (*squeezing angle*) depend on the time integral of χ [60].

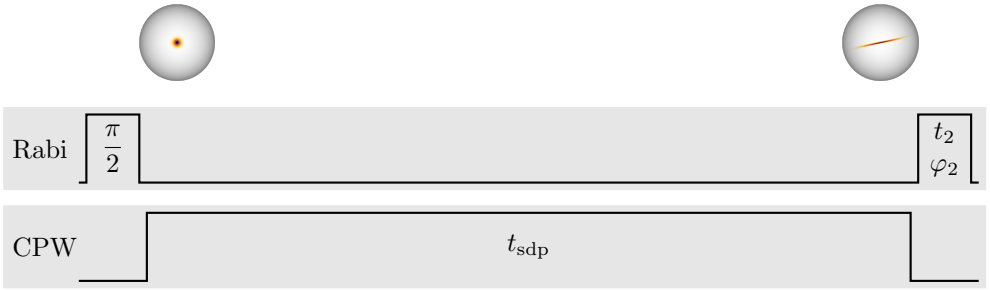

Figure C.3: Schematic of the spin squeezing sequence. Top: Qualitative representation on a Bloch sphere of the state of the BEC at different stages. Bottom: Time schematic of the Rabi coupling and of the CPW mw. The BEC is initially prepared in a CSS on the equator of the Bloch sphere (see the Bloch sphere on the top left) by a $\pi/2$ pulse. Then, the CPW mw is turned on for a time t_{sdp}, inducing the OAT dynamics and producing a SSS (see the Bloch sphere on the top right). Finally, a further Rabi pulse can be applied, e.g. to align the squeezed direction with the $\hat{S}_z$ axis.

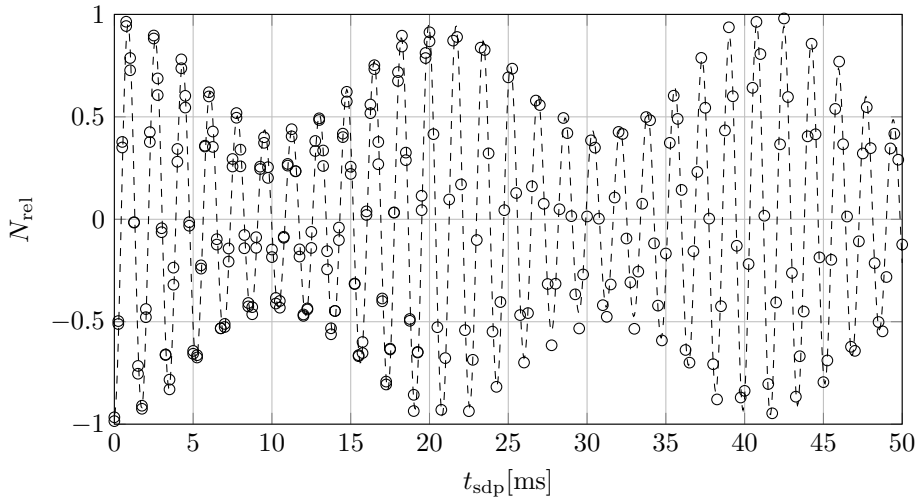

Figure C.4: Demixing-remixing dynamics measurement. The horizontal axis shows the time during which the state-dependent potential is turned on, t_{sdp}, and the vertical axis shows the normalised atom number imbalance, N_{rel}. The empty circles show the experimental data, whereas the dashed curve represents the fit given by Eq. (C.3).

The level shifts induced by the CPW mw also cause the system to accumulate a phase, which can be determined with a Ramsey experiment, see appendix C.5. Finally, a Rabi pulse with duration t_2 and phase φ_2 is applied, where t_2 and φ_2 depend on the use planned for the SSS.

As explained in Sec. 3.3.3, during the demixing-remixing dynamics the overlap between the two states can only be recovered for discrete values of t_{sdp}, called *revivals*, which can be determined by scanning t_{sdp} and measuring the interferometric contrast of the final state with a Ramsey experiment. In order to avoid a lengthy two-dimensional scan, it is possible to introduce some phase proportional to t_{sdp} in the final pulse (with much higher frequency than the splitting and recombination) and scan t_{sdp}, while keeping the phase of the last pulse fixed, i.e. $t_2 = t_{\pi/2}$ and $\varphi_2 = \text{constant}$. The result is a fast phase accumulation (the combined effect of the artificial phase and the one induced by the state dressing), whose contrast is modulated by the demixing-remixing dynamics. In the case of incomplete splitting of the two states and t_{sdp} much smaller than the BEC decoherence time, this can be fitted reasonably well by the function [51]

$$\langle N_{\mathrm{rel}}(t_{\mathrm{sdp}})\rangle = [A + B\cos(\omega_{\mathrm{dr}} t_{\mathrm{sdp}})]\cos(\omega_{\mathrm{fast}} t_{\mathrm{sdp}} + \varphi_{\mathrm{fast}}), \tag{C.3}$$

see Fig. C.4, where A and B are respectively the constant and modulated components of the amplitude, ω_{dr} is the angular frequency of the amplitude modulation caused by the demixing-remixing dynamics, and ω_{fast} and φ_{fast} are the frequency and phase of the fast oscillation. Based on the fit results, the value of t_{sdp} is chosen among the revival times – longer times yield stronger squeezing at the cost of larger phase noise. We typically choose the second revival, which for our experimental parameters occurs at about $t_{\mathrm{sdp}} \approx 40\,\mathrm{ms}$.

C.6.1 Demixing-remixing dynamics with spin echo

In the experiments presented in this thesis, a spin echo pulse [105] is used during the squeezing sequence, see Fig. C.5: At half t_{sdp}, the state-dependent potential is temporarily switched off and a Rabi π pulse (the *echo pulse*) is applied. This reduces shot-to-shot phase noise (e.g. due to CPW mw amplitude fluctuations) and mitigates asymmetric losses (see Sec. 2.3.6) [38, 51].

In order for the echo pulse to drive a collective spin rotation, it has to take place when the two BEC components are overlapped. Thus, we typically apply it at the first revival and then carry on with the demixing-remixing dynamics until the second. Since it is a π pulse applied to a state on the

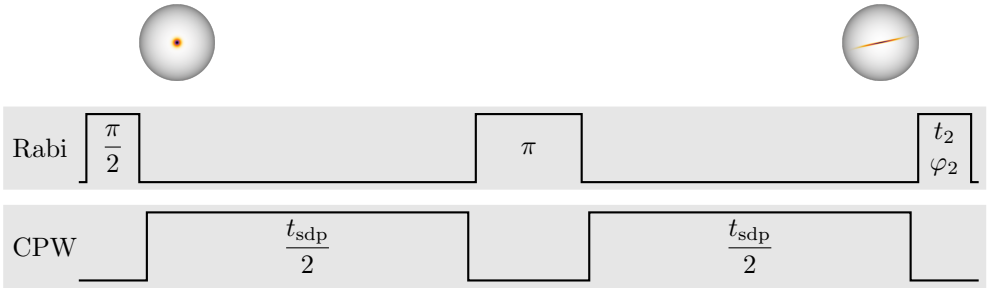

Figure C.5: Schematic of the spin squeezing sequence with spin echo. Top: Qualitative representation on a Bloch sphere of the state of the BEC at different stages. Bottom: Time schematic of the Rabi coupling and of the CPW mw. The BEC is initially prepared in a CSS on the equator of the Bloch sphere (see the Bloch sphere on the top left) by a $\pi/2$ pulse. Then, the CPW mw is turned on for a total time t_{sdp}, inducing the OAT dynamics and producing a SSS (see the Bloch sphere on the top right). At half of t_{sdp}, the CPW mw is switched off and the echo π pulse is performed. Finally, a further Rabi pulse can be applied, e.g. to align the squeezed direction with the $\hat{S}_z$ axis.

equator of the may-particle Bloch sphere, the phase of the echo pulse should only affect the phase calibration of the following pulses and not be important in itself. However, for the sake of reproducibility, we usually calibrate it so, that the state is rotated around its mean spin direction (i.e. at a zero crossing of the corresponding Ramsey fringe).

In addition to its improvements to stability, the use of a spin echo pulse simplifies the search of the second revival time: As long as the echo pulse is performed at half of the squeezing sequence, any phase accumulation with constant frequency (e.g. due to the level shifts induced by the CPW mw) cancels, making the phase calibration of the last pulse independent of t_{sdp}. Therefore, to determine the second revival time, one can calibrate the phase of the last pulse, φ_2, to correspond to the top of the related Ramsey fringe, scan t_{sdp}, and choose the value for which $\langle N_{\mathrm{rel}} \rangle$ is maximised.

C.7 Squeezing tomography

As mentioned in appendix C.6, the noise reduction and squeezing angle of a SSS produced by OAT dynamics depend on the time integral of χ [60], which is difficult to predict accurately. These quantities can be determined by a so-called *squeezing tomography* experiment: The SSS, prepared as described

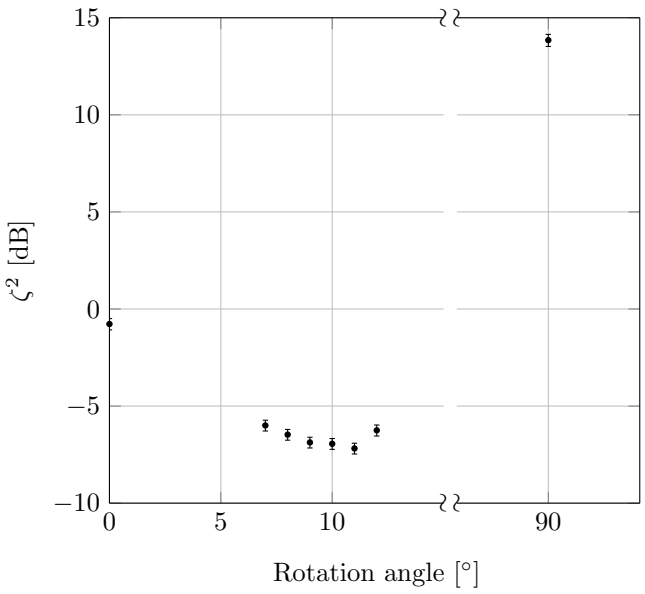

Figure C.6: Results of a typical squeezing tomography. The horizontal axis shows the rotation angle of the last Rabi pulse, $90° \, t_2/t_{\pi/2}$, and the vertical axis represents the number squeezing parameter, ζ^2.

in appendix C.6 (with or without spin echo pulse), is rotated around its mean spin direction by the final Rabi pulse, whose duration, t_2, is scanned. For every value of t_2, the experiment is repeated a sufficient number of times to obtain an accurate estimate for the variance of the measured collective spin direction, typically ~ 100 repetitions. The squeezing angle is thus determined by the setting for which this variance is minimised. In our experiments, this corresponds to a rotation by a small positive angle w.r.t. the $\hat{S}_z$ axis (typically $\sim 10°$) around the mean spin direction of the state. Thus, in order to find it with the shortest possible pulse, we choose φ_2 so, that the last pulse rotates the state in the opposite direction (i.e. at the zero crossing with negative slope of the corresponding Ramsey fringe).

Fig. C.6 shows the results of a typical squeezing tomography, where only the relevant rotation angles have been measured. From this measurement, we conclude that the squeezing angle is 10° and the number squeezing $\zeta(10°) = -6.9(3)\,\mathrm{dB}$. The measurement at 90° quantifies the anti-squeezing (although it is not exactly the anti-squeezed direction) and the phase noise accumulated during t_{sdp}, $\zeta(90°) = 13.8(3)\,\mathrm{dB}$. We attribute the excess noise w.r.t the Heisenberg limit to technical noise, see Refs. [51, 86] for a more detailed analysis.

The variance measured at 0° is expected to correspond to shot noise,

but it is actually smaller, $\zeta^2(0°) = -0.78(30)\,\mathrm{dB}$. We verified that this is not due to the imaging calibration by measuring the noise of a coherent spin state, which yielded $\zeta^2_{\mathrm{CSS}} = 0.2(2)\,\mathrm{dB}$. Hence, we attribute this effect to imperfections in the spin echo pulse.

C.8 Pulses during the time of flight

Due to the time constraints imposed by the time of flight and to the time-varying Rabi frequencies, calibrating the frequency and duration of the pulses introduced in Sec. 4.4 requires different strategies than for those performed when the atoms are still trapped. The calibration measurements discussed in this section are less precise, but allow us to calibrate the splitting and individual rotations of the split BECs pulses with a sufficient accuracy for the experiments presented in this thesis.

C.8.1 Resonance frequency

The resonance frequencies of the splitting pulses and individual manipulations are determined by scanning the frequencies of the driving fields and observing the contrast of Rabi oscillations, which can be fitted by the function

$$\langle N_{\mathrm{rel}}(t,\Delta)\rangle = 1 + \frac{\Omega^2}{\Omega^2+\Delta^2}\left[\cos\left(\sqrt{\Omega^2+\Delta^2}\,t\right) - 1\right], \tag{C.4}$$

where t is the pulse duration, Ω is the resonant Rabi frequency, and Δ is the detuning (in units of angular frequency). Note that this requires performing a two-dimensional scan of t and Δ for every signal of which we wish to find the resonance frequency. As a more time efficient alternative, one can perform Rabi oscillations at a fixed frequency and estimate Δ based on their contrast (although the sign of Δ cannot be determined by this method and must be found by trial and error).

C.8.2 Pulse duration

Since the Rabi frequencies during the time of flight are not constant, we cannot use longer pulses to calibrate the $\pi/2$ time (which is the strategy used in appendix C.3). Thus, we determine $t_{\pi/2}$ by looking for the shortest pulse duration for which $\langle N_{\mathrm{rel}}(t_{\pi/2})\rangle = 0$. This can be done either by scanning the pulse duration around this zero crossing and performing a linear fit, or by measuring $\langle N_{\mathrm{rel}}\rangle$ with a tentative pulse duration and using Eq. (C.1) (with $n = 1$).

Also, if we need to perform a π pulse, we need to calibrate t_π separately. Doing this in the same way used for $t_{\pi/2}$ is very imprecise, as $\langle N_{\mathrm{rel}}\rangle = \pm 1$ corresponds to the part of the Rabi oscillation that is least sensitive to pulse area variations, $\mathrm{d}\langle N_{\mathrm{rel}}\rangle/\mathrm{d}t|_{t_\pi} = 0$. In order to obtain a signal close to $\langle N_{\mathrm{rel}}\rangle = 0$ (i.e. in the most sensitive part of the Rabi oscillation), we perform a sequence similar to a Ramsey experiment: We prepare the state of the initial BEC along the $\hat{S}_x$ axis with a $\pi/2$ pulse in trap. Then, we apply the π pulse we wish to optimise around the $\pm\hat{S}_y$ axis. The value of t_π has to be corrected by a factor of

$$1 + \frac{\arcsin\big(\langle N_{\mathrm{rel}}^{-}\rangle\big) - \arcsin\big(\langle N_{\mathrm{rel}}^{+}\rangle\big)}{2\pi}, \tag{C.5}$$

where $N_{\mathrm{rel}}^{\pm}$ is the value of N_{rel} obtained after the rotation around the $\pm\hat{S}_y$ axis. Note that this method requires first calibrating the phase of the pulse we wish to optimise.

Appendix D

Phase of the split systems

As explained in Sec. 4.5.2, we study the phase noise due to trigger delay fluctuations with a simplified experimental sequence, where the initial BEC is prepared in a coherent spin state on the equator of the Bloch sphere by a $\pi/2$ pulse at the time t_0. After a duration t_1, the BEC is split into condensate A and B, and after t_2 the phases of the two systems are read out by another $\pi/2$ pulse. In this appendix I show the explicit calculations that lead to Eqs. (4.11) and (4.12).

The four involved atomic states are coupled with four different frequencies: The transition $|1A\rangle \leftrightarrow |2A\rangle$ is coupled by ω_A, $|1B\rangle \leftrightarrow |2B\rangle$ by ω_B, $|1A\rangle \leftrightarrow |1B\rangle$ by ω_1, and $|2A\rangle \leftrightarrow |2B\rangle$ by ω_2. We assume for simplicity that the coupling pulses are done instantaneously, or equivalently that their detuning with respect to the atomic transition does not matter,

$$\omega_A = \omega_{2A} - \omega_{1A}, \tag{D.1}$$
$$\omega_B = \omega_{1B} - \omega_{2B}, \tag{D.2}$$
$$\omega_1 = \omega_{1B} - \omega_{1A}, \tag{D.3}$$
$$\omega_2 = \omega_{2A} - \omega_{2B}, \tag{D.4}$$

where the frequency differences on the right-hand side represent the atomic transition frequencies. The coupling frequencies are produced by different combinations of signals (see Secs. 3.3.2 and 4.4.2), namely

$$\begin{aligned}
\omega_A &= \omega_{\mathrm{rf}} + \omega_{\mathrm{mw}} + \omega_{\mathrm{IQ}_A}, \\
\omega_B &= \omega_{\mathrm{mw}} + \omega_{\mathrm{IQ}_B}, \\
\omega_1 &= \omega_{\mathrm{mw}} + \omega_{\mathrm{IQ}_1}, \\
\omega_2 &= \omega_{\mathrm{mw}} + \omega_{\mathrm{IQ}_2},
\end{aligned}$$

where ω_{rf} is the rf frequency, ω_{mw} is the carrier frequency of the mw generator, and $\omega_{\mathrm{IQ},i}$ is the IQ modulation frequency used to produce ω_i, $i \in \{A, B, 1, 2\}$.

Similarly, the phases of the coupling signals are given by

$$\varphi_A = \varphi_{\mathrm{rf}} + \varphi_{\mathrm{mw}} + \varphi_{\mathrm{IQ}_A}, \tag{D.5}$$

$$\varphi_B = \varphi_{\mathrm{mw}} + \varphi_{\mathrm{IQ}_B}, \tag{D.6}$$

$$\varphi_1 = \varphi_{\mathrm{mw}} + \varphi_{\mathrm{IQ}_1}, \tag{D.7}$$

$$\varphi_2 = \varphi_{\mathrm{mw}} + \varphi_{\mathrm{IQ}_2}, \tag{D.8}$$

where φ_{rf} is the phase of the rf signal, φ_{mw} is the phase of the mw carrier, and $\varphi_{\mathrm{IQ},i}$ is the phase of the IQ modulation signal used to produce ω_i, $i \in \{A, B, 1, 2\}$. The above frequency definitions can be combined into the identities

$$\omega_1 + \omega_2 = \omega_A + \omega_B, \tag{D.9}$$

$$\omega_{\mathrm{IQ}_1} + \omega_{\mathrm{IQ}_2} = \omega_{\mathrm{IQ}_A} + \omega_{\mathrm{IQ}_B} + \omega_{\mathrm{rf}}, \tag{D.10}$$

which will be useful later.

We treat the phase evolution in the laboratory frame of reference, defining $t = 0$ as the time when the rf generator triggers the execution of the IQ sequence. The phase of the signal $\alpha \in \{\mathrm{rf}, \mathrm{mw}, \mathrm{IQ}_A, \mathrm{IQ}_B, \mathrm{IQ}_1, \mathrm{IQ}_2\}$ can be written as

$$\varphi_\alpha(t) = \varphi_\alpha(0) + \omega_\alpha t. \tag{D.11}$$

Since the time reference is defined by the rf generator, the initial rf phase is constant and can be chosen to be zero, $\varphi_{\mathrm{rf}}(0) = 0$. The initial phase of the IQ signals is given by $\varphi_{\mathrm{IQ}_i}(0) = -\omega_{\mathrm{IQ}_i}\delta t$, where δt is the trigger delay of the IQ generator. Given that the mw generator is run in continuous-wave mode, $\varphi_{\mathrm{mw}}(0)$ is random.

Let us now apply all of the above to our simplified experimental sequence. Note that every pulse but the final one couples a populated state to an unpopulated one. Due to this, the relative phases between the populations of the atomic states are given by the driving fields that first couple them,

$$\varphi_{2A}(t_0) - \varphi_{1A}(t_0) = \varphi_A(t_0), \tag{D.12}$$

$$\varphi_{1B}(t_0 + t_1) - \varphi_{1A}(t_0 + t_1) = \varphi_1(t_0 + t_1), \tag{D.13}$$

$$\varphi_{2A}(t_0 + t_1) - \varphi_{2B}(t_0 + t_1) = \varphi_2(t_0 + t_1), \tag{D.14}$$

where in the left-hand side of every equation the sign reflects which state has higher energy. The measured phase of each system corresponds to the difference between the phase of the final pulse and the relative phase between the two involved states. In the case of system A, this is simply

$$\begin{aligned}\phi_A &= \varphi_A(t_0 + t_1 + t_2) - [\varphi_{2A}(t_0 + t_1 + t_2) - \varphi_{1A}(t_0 + t_1 + t_2)] \\ &= [\omega_A - (\omega_{2A} - \omega_{1A})](t_1 + t_2) + \varphi_A(t_0) - [\varphi_{2A}(t_0) - \varphi_{1A}(t_0)] \\ &= 0.\end{aligned}$$

The measured phase of system B, on the other hand, is more complicated,

$$
\begin{aligned}
\phi_B &= \varphi_B(t_0+t_1+t_2) - [\varphi_{1B}(t_0+t_1+t_2) - \varphi_{2B}(t_0+t_1+t_2)] \\
&\quad \text{(apply Eq. (D.2))} \\
&= \varphi_B(t_0+t_1) - [\varphi_{1B}(t_0+t_1) - \varphi_{2B}(t_0+t_1)] \\
&\quad \text{(apply Eqs. (D.13) and (D.14))} \\
&= \varphi_B(t_0+t_1) + \varphi_{2A}(t_0+t_1) - \varphi_{1A}(t_0+t_1) + \\
&\quad - \varphi_1(t_0+t_1) - \varphi_2(t_0+t_1) \\
&\quad \text{(apply Eq. (D.12))} \\
&= \varphi_A(t_0+t_1) + \varphi_B(t_0+t_1) - \varphi_1(t_0+t_1) - \varphi_2(t_0+t_1) \\
&\quad \text{(apply } \varphi_i(t) = \varphi_i(0) + \omega_i t, \text{ where } i \in \{A, B, 1, 2\}) \\
&= \varphi_A(0) + \varphi_B(0) - \varphi_1(0) - \varphi_2(0) \\
&\quad + (\omega_A + \omega_B - \omega_1 - \omega_2)(t_0+t_1) \\
&\quad \text{(apply Eqs. (D.5), (D.6), (D.7), (D.8), and (D.9))} \\
&= \varphi_{\mathrm{rf}}(0) + \varphi_{\mathrm{mw}}(0) + \varphi_{\mathrm{IQ}_A}(0) + \varphi_{\mathrm{mw}}(0) + \varphi_{\mathrm{IQ}_B}(0) + \\
&\quad - \varphi_{\mathrm{mw}}(0) - \varphi_{\mathrm{IQ}_1}(0) - \varphi_{\mathrm{mw}}(0) - \varphi_{\mathrm{IQ}_2}(0) \\
&\quad \text{(apply } \varphi_{\mathrm{rf}}(0) = 0) \\
&= \varphi_{\mathrm{IQ}_A}(0) + \varphi_{\mathrm{IQ}_B}(0) - \varphi_{\mathrm{IQ}_1}(0) - \varphi_{\mathrm{IQ}_2}(0) \\
&\quad \text{(apply Eq. (D.11))} \\
&= (\omega_{\mathrm{IQ}_1} + \omega_{\mathrm{IQ}_2} - \omega_{\mathrm{IQ}_A} - \omega_{\mathrm{IQ}_B})\delta t \\
&\quad \text{(apply Eq. D.10)} \\
&= \omega_{\mathrm{rf}}\delta t,
\end{aligned}
$$

which shows that, in contrast to ϕ_A, the measured phase of system B is affected by fluctuations in the triggering delay of the IQ generator.

Acknowledgements

All the results presented in this thesis were obtained by a team, to whom I am immensely grateful. This was a challenging project, whose success relied on all team members cooperating towards a common goal.

Firstly, I wish to thank Prof. Philipp Treutlein for being a present and understanding supervisor, always ready to provide precious input with discussions and supportive when I was going through difficult times (and when I suggested that we should buy a coffee machine).

My work was supervised directly by Dr. Tilman Zibold, who has been the main source of progress of our project during my doctorate and who has taught me incredible amounts about physics, experimental techniques, and coffee.

Most of my time in the laboratory was spent together with Dr. Yifan Li, who first contributed to teaching me how to operate the experimental apparatus and has then been an excellent work companion, both scientifically and personally. Also, thank you for introducing me to badminton and admitting that you do not use the proper chopstick technique.

Towards the end of my doctorate, the team was joined by Lex Joosten, whom I wish to thank for numerous discussions and for getting a glass teapot for the office.

Philipp and Tilman were also part of my PhD committee, together with my second supervisor, Prof. Christoph Bruder, and my external examiner, Prof. Marco Fattori. I wish to thank the committee for undergoing the hassle of reading my thesis and for the interesting questions they asked during my defence. In addition to this, I would like to thank Marco for coming all the way from Florence to Basel and back again, spending about 14 hours in a train within two days.

All the people mentioned above greatly helped me improve this thesis with their careful reading. From my experience, reading what I write is not pleasant, so thank you all once more for this.

I would also like to thank Dr. Matteo Fadel and Dr. Boris Décamps for contributing to my supervision during the first months of my doctorate.

Besides the contributions to this project made by permanent team members, over the course of my doctorate two master's students have made decisive improvements to the experimental apparatus: Simon Josephy, who built the offset lock of the slave laser and implemented the new experiment control system, and Clara Piekarsky, who renewed the imaging system. I would also like to acknowledge the work of Jiajie Guo, who spent one year in our team as a visiting student; during this time she performed interesting theoretical studies about non-linear squeezing in our system and introduced me to proper Chinese tea.

I realise that beginning a doctorate with a working apparatus is a great advantage over building one myself. Hence, I wish to thank all those who have worked on it in the past.

In addition to the scientific contributions mentioned above, I would like to thank the rest of the group for providing a friendly work environment, as well as the technical and administrative staff of the physics department of the university of Basel, without whom scientific activities would not be possible.

Finally, I would like to thank my family for giving me the chance to study and for supporting me (both emotionally and financially) throughout my studies. I should also acknowledge the emotional support provided by my girlfriend and friends. The people mentioned in this paragraph allowed me to keep my brain functional during what have been, after all, difficult years.

Bibliography

[1] A. Einstein, B. Podolsky, and N. Rosen. Can quantum-mechanical description of physical reality be considered complete? *Phys. Rev.*, 47:777, 1935.

[2] E. Schrödinger. Die gegenwärtige Situation in der Quantenmechanik. *Naturwissenschaften*, 23:844, 1935.

[3] E. Schrödinger. Discussion of probability relations between separated systems. *Math. Proc. Cambridge Philos. Soc.*, 31:555, 1935.

[4] J. S. Bell. On the Einstein Podolsky Rosen paradox. *Physics Physique Fizika*, 1:195, 1964.

[5] C. S. Wu and I. Shaknov. The angular correlation of scattered annihilation radiation. *Phys. Rev.*, 77:136, 1950.

[6] Z. Y. Ou, S. F. Pereira, H. J. Kimble, and K. C. Peng. Realization of the Einstein-Podolsky-Rosen paradox for continuous variables. *Phys. Rev. Lett.*, 68:3663, 1992.

[7] E. Hagley, X. Maître, G. Nogues, C. Wunderlich, M. Brune, J. M. Raimond, and S. Haroche. Generation of Einstein-Podolsky-Rosen pairs of atoms. *Phys. Rev. Lett.*, 79:1, 1997.

[8] W. P. Bowen, R. Schnabel, P. K. Lam, and T. C. Ralph. Experimental investigation of criteria for continuous variable entanglement. *Phys. Rev. Lett.*, 90:043601, 2003.

[9] M. D. Reid, P. D. Drummond, W. P. Bowen, E. G. Cavalcanti, P. K. Lam, H. A. Bachor, U. L. Andersen, and G. Leuchs. Colloquium: The Einstein-Podolsky-Rosen paradox: From concepts to applications. *Rev. Mod. Phys.*, 81:1727, 2009.

[10] K. V. Kheruntsyan, J.-C. Jaskula, P. Deuar, M. Bonneau, G. B. Partridge, J. Ruaudel, R. Lopes, D. Boiron, and C. I. Westbrook. Violation of the Cauchy-Schwarz inequality with matter waves. *Phys. Rev. Lett.*, 108:260401, 2012.

[11] S. J. Freedman and J. F. Clauser. Experimental test of local hidden-variable theories. *Phys. Rev. Lett.*, 28:938, 1972.

[12] M. Lamehi-Rachti and W. Mittig. Quantum mechanics and hidden variables: A test of Bell's inequality by the measurement of the spin correlation in low-energy proton-proton scattering. *Phys. Rev. D*, 14:2543, 1976.

[13] A. Aspect, P. Grangier, and G. Roger. Experimental realization of Einstein-Podolsky-Rosen-Bohm Gedankenexperiment: A new violation of Bell's inequalities. *Phys. Rev. Lett.*, 49:91, 1982.

[14] A. Aspect, J. Dalibard, and G. Roger. Experimental test of Bell's inequalities using time-varying analyzers. *Phys. Rev. Lett.*, 49:1804, 1982.

[15] B. Hensen, H. Bernien, A. E. Dréau, A. Reiserer, N. Kalb, M. S. Blok, J. Ruitenberg, R. F. L. Vermeulen, R. N. Schouten, C. Abellán, W. Amaya, V. Pruneri, M. W. Mitchell, M. Markham, D. J. Twitchen, D. Elkouss, S. Wehner, T. H. Taminiau, and R. Hanson. Loophole-free Bell inequality violation using electron spins separated by 1.3 kilometres. *Nature*, 526:682, 2015.

[16] M. Giustina, M. A. M. Versteegh, S. Wengerowsky, J. Handsteiner, A. Hochrainer, K. Phelan, F. Steinlechner, J. Kofler, J.-Å. Larsson, C. Abellán, W. Amaya, V. Pruneri, M. W. Mitchell, J Beyer, T Gerrits, A. E. Lita, L. K. Shalm, S. W. Nam, T. Scheidl, R. Ursin, B. Wittmann, and A. Zeilinger. Significant-loophole-free test of Bell's theorem with entangled photons. *Phys. Rev. Lett.*, 115:250401, 2015.

[17] L. K. Shalm, E. Meyer-Scott, B. G. Christensen, P. Bierhorst, M. A. Wayne, M. J. Stevens, T. Gerrits, S. Glancy, D. R. Hamel, M. S. Allman, K. J. Coakley, S. D. Dyer, C. Hodge, A. E. Lita, V. B. Verma, C. Lambrocco, E. Tortorici, A. L. Migdall, Y. Zhang, D. R. Kumor, W. H. Farr, F. Marsili, M. D. Shaw, J. A. Stern, C. Abellán, W. Amaya, V. Pruneri, T. Jennewein, M. W. Mitchell, P. G. Kwiat, J. C. Bienfang, R. P. Mirin, E. Knill, and S. W. Nam. Strong loophole-free test of local realism. *Phys. Rev. Lett.*, 115:250402, 2015.

[18] W. Rosenfeld, D. Burchardt, R. Garthoff, K. Redeker, N. Ortegel, M. Rau, and H. Weinfurter. Event-ready Bell test using entangled atoms simultaneously closing detection and locality loopholes. *Phys. Rev. Lett.*, 119:010402, 2017.

[19] A. J. Leggett. Testing the limits of quantum mechanics: motivation, state of play, prospects. *J. Phys.: Condens. Matt.*, 14:R415, 2002.

[20] A. J. Leggett. How far do EPR-Bell experiments constrain physical collapse theories? *J. Phys. A: Math. Theor.*, 40:3141, 2007.

[21] E. G. Cavalcanti and M. D. Reid. Uncertainty relations for the realization of macroscopic quantum superpositions and EPR paradoxes. *J. Mod. Opt.*, 54:2373, 2007.

[22] B. Julsgaard, A. Kozhekin, and E. S. Polzik. Experimental long-lived entanglement of two macroscopic objects. *Nature*, 413:400, 2001.

[23] C. W. Chou, H. de Riedmatten, D. Felinto, S. V. Polyakov, S. J. van Enk, and H. J. Kimble. Measurement-induced entanglement for excitation stored in remote atomic ensembles. *Nature*, 438:828, 2005.

[24] M. Lettner, M. Mücke, S. Riedl, C. Vo, C. Hahn, S. Baur, J. Bochmann, S. Ritter, S. Dürr, and G. Rempe. Remote entanglement between a single atom and a Bose-Einstein condensate. *Phys. Rev. Lett.*, 106:210503, 2011.

[25] R. A. Thomas, M. Parniak, C. Østfeldt, C. B. Møller, C. Bærentsen, Y. Tsaturyan, A. Schliesser, J. Appel, E. Zeuthen, and E. S. Polzik. Entanglement between distant macroscopic mechanical and spin systems. *Nat. Phys.*, 17:228, 2021.

[26] S. Kotler, G. A. Peterson, E. Shojaee, F. Lecocq, K. Cicak, A. Kwiatkowski, S. Geller, S. Glancy, E. Knill, R. W. Simmonds, J. Aumentado, and J. D. Teufel. Direct observation of deterministic macroscopic entanglement. *Science*, 372:622, 2021.

[27] L. M. de Lépinay, C. F. Ockeloen-Korppi, M. J. Woolley, and M. A. Sillanpää. Quantum mechanics-free subsystem with mechanical oscillators. *Science*, 372:625, 2021.

[28] J. Peise, I. Kruse, K. Lange, B. Lücke, L. Pezzé, J. Arlt, W. Ertmer, K. Hammerer, L. Santos, A. Smerzi, and C. Klempt. Satisfying the Einstein-Podolsky-Rosen criterion with massive particles. *Nat. Commun.*, 6:8984, 2015.

[29] R. Schmied, J.-D. Bancal, B. Allard, M. Fadel, V. Scarani, P. Treutlein, and N. Sangouard. Bell correlations in a Bose-Einstein condensate. *Science*, 352:441, 2016.

[30] M. Fadel, T. Zibold, B. Décamps, and P. Treutlein. Spatial entanglement patterns and Einstein-Podolsky-Rosen steering in Bose-Einstein condensates. *Science*, 360:409, 2018.

[31] P. Kunkel, M. Prüfer, H. Strobel, D. Linnemann, A. Frölian, T. Gasenzer, M. Gärttner, and M. K. Oberthaler. Spatially distributed multipartite entanglement enables EPR steering of atomic clouds. *Science*, 360:413, 2018.

[32] D. Bohm. *Quantum Theory*. Constable, London, 1951.

[33] D. Bohm and Y. Aharonov. Discussion of experimental proof for the paradox of Einstein, Rosen, and Podolsky. *Phys. Rev.*, 108:1070, 1957.

[34] A. Sørensen, L.-M. Duan, J. I. Cirac, and P. Zoller. Many-particle entanglement with Bose-Einstein condensates. *Nature*, 409:63, 2001.

[35] M. F. Riedel, P. Böhi, Y. Li, T. W. Hänsch, A. Sinatra, and P. Treutlein. Atom-chip-based generation of entanglement for quantum metrology. *Nature*, 464:1170, 2010.

[36] P. Colciaghi, Y. Li, P. Treutlein, and T. Zibold. Einstein-Podolsky-Rosen experiment with two Bose-Einstein condensates. *Phys. Rev. X*, 13:021031, 2023.

[37] Y. Li, K. Pawłowski, B. Décamps, P. Colciaghi, M. Fadel, P. Treutlein, and T. Zibold. Fundamental limit of phase coherence in two-component Bose-Einstein condensates. *Phys. Rev. Lett.*, 125:123402, 2020.

[38] M. Fadel. *Many-particle entanglement, Einstein-Podolsky-Rosen steering and Bell correlations in Bose-Einstein condensates*. PhD thesis, Universität Basel, Basel, 2019.

[39] W. Ketterle, D. S. Durfee, and D. M. Stamper-Kurn. Making, probing and understanding Bose-Einstein condensates. In M. Inguscio, S. Stringari, and C. Wieman, editors, *Proceedings of the International School of Physics "Enrico Fermi", Course CXL*, pages 67–176. IOS, Amsterdam, 1999.

[40] F. Dalfovo, S. Giorgini, L. P. Pitaevskii, and S. Stringari. Theory of Bose-Einstein condensation in trapped gases. *Rev. Mod. Phys.*, 71:463, 1999.

[41] A. J. Leggett. Bose-Einstein condensation in the alkali gases: Some fundamental concepts. *Rev. Mod. Phys.*, 73:307, 2001.

[42] P. Treutlein. *Coherent manipulation of ultracold atoms on atom chips.* PhD thesis, Ludwigs-Maximilians-Universität, München, 2008.

[43] S. N. Bose. Plancks Gesetz und Lichtquantenhypothese. *Z. Phys.*, 26:178, 1924.

[44] A. Einstein. Quantentheorie des einatomigen idealen Gases. *Sitzber. Kgl. Preuss. Akad. Wiss.*, 22:261, 1924.

[45] A. Einstein. Quantentheorie des einatomigen idealen Gases. *Sitzber. Kgl. Preuss. Akad. Wiss.*, 23:3, 1925.

[46] M. H. Anderson, J. R. Ensher, M. R. Matthews, C. E. Wieman, and E. A. Cornell. Observation of Bose-Einstein Condensation in a dilute atomic vapor. *Science*, 269:198, 1995.

[47] C. C. Bradley, C. A. Sackett, J. J. Tollett, and R. G. Hulet. Evidence of Bose-Einstein condensation in an atomic gas with attractive interactions. *Phys. Rev. Lett.*, 75:1687, 1995.

[48] K. B. Davis, M.-O. Mewes, M. R. Andrews, N. J. van Druten, D. S. Durfee, D. M. Kurn, and W. Ketterle. Bose-Einstein condensation in a gas of sodium atoms. *Phys. Rev. Lett.*, 75:3969, 1995.

[49] S. Giorgini, L. P. Pitaevskii, and S. Stringari. Condensate fraction and critical temperature of a trapped interacting Bose gas. *Phys. Rev. A*, 54:R4633, 1996.

[50] B. Allard, M. Fadel, R. Schmied, and P. Treutlein. Sideband Rabi spectroscopy of finite-temperature trapped Bose gases. *Phys. Rev. A*, 93:043624, 2016.

[51] Y. Li. *Phase coherence and spin squeezing in a two component Bose-Einstein condensate.* PhD thesis, Tsinghua University, Beijing, 2021.

[52] D. A. Steck. Rubidium 87 D line data. `http://steck.us/alkalidata`. (revision 2.2.2, 9 July 2021).

[53] M. Egorov, B. Opanchuk, P. Drummond, B. V. Hall, P. Hannaford, and A. I. Sidorov. Measurement of s-wave scattering lengths in a two-component Bose-Einstein condensate. *Phys. Rev. A*, 87:053614, 2013.

[54] D. M. Harber, H. J. Lewandowski, J. M. McGuirk, and E. A. Cornell. Effect of cold collisions on spin coherence and resonance shifts in a magnetically trapped ultracold gas. *Phys. Rev. A*, 66:053616, 2002.

[55] C. Deutsch, F. Ramirez-Martinez, C. Lacroûte, F. Reinhard, T. Schneider, J. N. Fuchs, F. Piéchon, F. Laloë, J. Reichel, and P. Rosenbusch. Spin self-rephasing and very long coherence times in a trapped atomic ensemble. *Phys. Rev. Lett.*, 105:020401, 2010.

[56] R. Szmuk, V. Dugrain, W. Maineult, J. Reichel, and P. Rosenbusch. Stability of a trapped-atom clock on a chip. *Phys. Rev. A*, 92:012106, 2015.

[57] L. Pezzé, A. Smerzi, M. K. Oberthaler, R. Schmied, and P. Treutlein. Quantum metrology with nonclassical states of atomic ensembles. *Rev. Mod. Phys.*, 90:035005, 2018.

[58] J. J. Sakurai. *Modern Quantum Mechanics*. Addison-Wesley Publishing Company, 1994.

[59] Y. Li, P. Treutlein, J. Reichel, and A. Sinatra. Spin squeezing in a bimodal condensate: spatial dynamics and particle losses. *Eur. Phys. J. B*, 68:365, 2009.

[60] M. Kitagawa and M. Ueda. Squeezed spin states. *Phys. Rev. A*, 47:5138, 1993.

[61] J. P. Dowling, G. S. Agarwal, and W. P. Schleich. Wigner distribution of a general angular-momentum state: Applications to a collection of two-level atoms. *Phys. Rev. A*, 49:4101, 1994.

[62] R. Schmied and P. Treutlein. Tomographic reconstruction of the Wigner function on the Bloch sphere. *New J. Phys.*, 13:065019, 2011.

[63] D. J. Wineland, J. J. Bollinger, W. M. Itano, F. L. Moore, and D. J. Heinzen. Spin squeezing and reduced quantum noise in spectroscopy. *Phys. Rev. A*, 46:6797, 1992.

[64] D. J. Wineland, J. J. Bollinger, W. M. Itano, and D. J. Heinzen. Squeezed atomic states and projection noise in spectroscopy. *Phys. Rev. A*, 50:67, 1994.

[65] L. Pezzé and A. Smerzi. Entanglement, nonlinear dynamics, and the Heisenberg limit. *Phys. Rev. Lett.*, 102:100401, 2009.

[66] M. Gessner, A. Smerzi, and L. Pezzé. Metrological nonlinear squeezing parameter. *Phys. Rev. Lett.*, 122:090503, 2019.

[67] Y. Baamara, A. Sinatra, and M. Gessner. Squeezing of nonlinear spin observables by one axis twisting in the presence of decoherence: An analytical study. *Comptes Rendus. Physique*, 23:1, 2022.

[68] S. Colombo, E. Pedrozo-Peñafiel, A. F. Adiyatullin, Z. Li, E. Mendez, C. Shu, and V. Vuletić. Time-reversal-based quantum metrology with many-body entangled states. *Nat. Phys.*, 18:925, 2022.

[69] C. Ockeloen. *Quantum Metrology with a Scanning Probe Atom Interferometer*. PhD thesis, Universität Basel, Basel, 2014.

[70] A. Sinatra and Y. Castin. Phase dynamics of Bose-Einstein condensates: Losses versus revivals. *Eur. Phys. J. D*, 4:247, 1998.

[71] N. F. Ramsey. A molecular beam resonance method with separated oscillating fields. *Phys. Rev.*, 78:695, 1950.

[72] Y. Castin and A. Sinatra. Spatial and temporal coherence of a Bose-condensed gas. In *New Trends and Hot Topics in Atomic and Polariton Condensates*, pages 315–339. Springer-Verlag Berlin Heidelberg, 2013.

[73] P. Böhi, M. F. Riedel, J. Hoffrogge, J. Reichel, T. W. Hänsch, and P. Treutlein. Coherent manipulation of Bose-Einstein condensates with state-dependent microwave potentials on an atom chip. *Nat. Phys.*, 5:592, 2009.

[74] P. A. Böhi. *Coherent manipulation of ultracold atoms with microwave near-fields*. PhD thesis, Ludwigs-Maximilians-Universität, München, 2010.

[75] M. F. Riedel. *Multi-particle entanglement on an atom chip*. PhD thesis, Universität Basel, Basel, 2010.

[76] J. Reichel and V. Vuletić, editors. *Atom Chips*. Wiley-VCH, Weinheim, Germany, 2011.

[77] P. A. Böhi, M. F. Riedel, T. W. Hänsch, and P. Treutlein. Imaging of microwave fields using ultracold atoms. *Appl. Phys. Lett.*, 97:051101, 2010.

[78] C. F. Ockeloen, R. Schmied, M. F. Riedel, and P. Treutlein. Quantum metrology with a scanning probe atom interferometer. *Phys. Rev. Lett.*, 111:143001, 2013.

[79] Y. V. Gott, M. S. Ioffe, and V. G. Tel'Kovskii. *Nuclear Fusion Supplement*, 3:1045, 1962.

[80] D. E. Pritchard. Cooling neutral atoms in a magnetic trap for precision spectroscopy. *Phys. Rev. Lett.*, 51:1336, 1983.

[81] V. S. Bagnato, G. P. Lafyatis, A. G. Martin, E. L. Raab, R. N. Ahmad-Bitar, and D. E. Pritchard. Continuous stopping and trapping of neutral atoms. *Phys. Rev. Lett.*, 58:2194, 1987.

[82] J. Hoffrogge. Mikrowellen-Nahfelder auf Atomchips. Master's thesis, Ludwig-Maximilians-Universität, München, 2007.

[83] S. Josephy. Laser phase lock loop in GHz range. Semester project, Universität Basel, Basel, 2019.

[84] W. Ketterle and N. J. van Druten. Evaporative cooling of atoms. *Adv. At. Mol. Opt. Phys*, 37:181, 1996.

[85] D. A. Steck. Quantum and atom optics. `http://steck.us/teaching`. (revision 0.13.9, 22 July 2021).

[86] C. Piekarski. Precision imaging for a BEC-on-chip experiment. Master's thesis, ETH Zürich, Basel, 2022.

[87] G. Reinaudi, T. Lahaye, Z. Wang, and D. Guéry-Odelin. Strong saturation absorption imaging of dense clouds of ultracold atoms. *Opt. Lett.*, 32:3143, 2007.

[88] W. Muessel, H. Strobel, M. Joos, E. Nicklas, I. Stroescu, J. Tomkovič, D. B. Hume, and M. K. Oberthaler. Optimized absorption imaging of mesoscopic atomic clouds. *Appl. Phys. B*, 113:69, 2013.

[89] C. F. Ockeloen, A. F. Tauschinsky, R. J. C. Spreeuw, and S. Whitlock. Detection of small atom numbers through image processing. *Phys. Rev. A*, 82:061606, 2010.

[90] S. Josephy. State of the art computer control for studying many-body physics with ultra cold quantum gases. Master's thesis, Universität Basel, Basel, 2020.

[91] P. T. Starkey, C. J. Billington, S. P. Johnstone, M. Jasperse, K. Helmerson, L. D. Turner, and R. P. Anderson. A scripted control system for autonomous hardware-timed experiments. *Rev. Sci. Instrum.*, 84:085111, 2013.

[92] N. Killoran, M. Cramer, and M. B. Plenio. Extracting entanglement from identical particles. *Phys. Rev. Lett.*, 112:150501, 2014.

[93] K. Lange, J. Peise, B. Lücke, I. Kruse, G. Vitagliano, I. Apellaniz, M. Kleinmann, G. Tóth, and C. Klempt. Entanglement between two spatially separated atomic modes. *Science*, 360:416, 2018.

[94] J. F. Clauser, M. A. Horne, A. Shimony, and R. A. Holt. Proposed experiment to test local hidden-variable theories. *Phys. Rev. Lett.*, 23:880, 1969.

[95] H. M. Wiseman, S. J. Jones, and A. C. Doherty. Steering, entanglement, nonlocality, and the Einstein-Podolsky-Rosen paradox. *Phys. Rev. Lett.*, 98:140402, 2007.

[96] R. F. Werner. Quantum states with Einstein-Podolsky-Rosen correlations admitting a hidden-variable model. *Phys. Rev. A*, 40:4277, 1989.

[97] D. Cavalcanti and P. Skrzypczyk. Quantum steering: a review with focus on semidefinite programming. *Rep. Prog. Phys.*, 80:024001, 2017.

[98] R. Uola, A. C. S. Costa, H. Chau Nguyen, and O. Gühne. Quantum steering. *Rev. Mod. Phys.*, 92:015001, 2020.

[99] G. C. Ghirardi, A. Rimini, and T. Weber. A general argument against superluminal transmission through the quantum mechanical measurement process. *Lett. Nuovo Cimento*, 27:293, 1980.

[100] J. S. Bell and A. Aspect. *Speakable and Unspeakable in Quantum Mechanics: Collected Papers on Quantum Philosophy.* Cambridge University Press, 2nd edition, 2004.

[101] W. K. Wootters and W. H. Zurek. A single quantum cannot be cloned. *Nature*, 299:802, 1982.

[102] M. D. Reid. Demonstration of the Einstein-Podolsky-Rosen paradox using nondegenerate parametric amplification. *Phys. Rev. A*, 40:913, 1989.

[103] V. Giovannetti, S. Mancini, D. Vitali, and P. Tombesi. Characterizing the entanglement of bipartite quantum systems. *Phys. Rev. A*, 67:022320, 2003.

[104] E. Oudot, J.-D. Bancal, P. Sekatski, and N. Sangouard. Bipartite nonlocality with a many-body system. *New J. Phys.*, 21:103043, 2019.

[105] E. L. Hahn. Spin echoes. *Phys. Rev.*, 80:580, 1950.

[106] E. Timmermans, R. Côté, and I. Simbotin. Self-similar BEC dynamics: accuracy and applications. *J. Phys. B*, 33:4157, 2000.

[107] Y. Castin and R. Dum. Bose-Einstein condensates in time dependent traps. *Phys. Rev. Lett.*, 77:5315, 1996.

[108] A. Peres. Unperformed experiments have no results. *Am. J. Phys.*, 46:745, 1978.

[109] M. Gessner, L. Pezzé, and A. Smerzi. Sensitivity bounds for multiparameter quantum metrology. *Phys. Rev. Lett.*, 121:130503, 2018.

[110] B. Yadin, M. Fadel, and M. Gessner. Metrological complementarity reveals the Einstein-Podolsky-Rosen paradox. *Nat. Commun.*, 12:2410, 2021.

[111] M. Fadel, B. Yadin, Y. Mao, T. Byrnes, and M. Gessner. Multiparameter quantum metrology and mode entanglement with spatially split nonclassical spin states. *arXiv*, page 2201.11081, 2022.

[112] Y. Baamara, M. Gessner, and A. Sinatra. Quantum-enhanced multiparameter estimation and compressed sensing of a field. *SciPost Phys.*, 14:050, 2023.

[113] K. Pawłowski, M. Fadel, P. Treutlein, Y. Castin, and A. Sinatra. Mesoscopic quantum superpositions in bimodal Bose-Einstein condensates: Decoherence and strategies to counteract it. *Phys. Rev. A*, 95:063609, 2017.